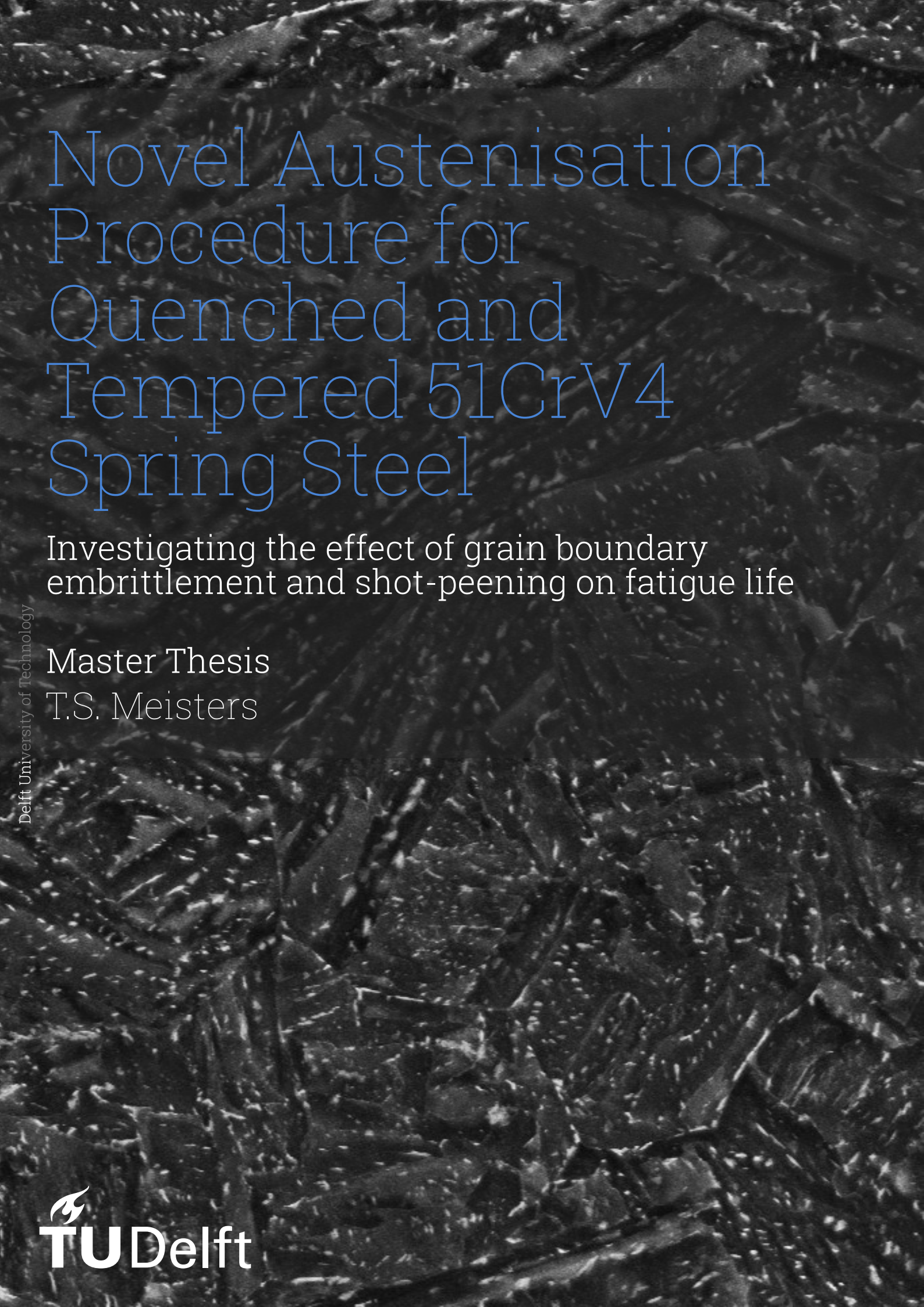

Novel Austenisation Procedure for Quenched and Tempered 51CrV4 Spring Steel

Investigating the effect of grain boundary embrittlement and shot-peening on fatigue life

Master Thesis

T.S. Meisters

Delft University of Technology

TU Delft

Novel Austenisation Procedure for Quenched and Tempered 51CrV4 Spring Steel

Investigating the effect of grain boundary embrittlement and shot-peening on fatigue life

by

T.S. Meisters

to obtain the degree of Master of Science
at the Delft University of Technology,
to be defended publicly on Tuesday December 19, 2023 at 15:00.

Student number: 4462688
Project duration: May, 2023 – December, 2023

Cover: SEM micrograph of the microstructure of a trailing arm
Style: TU Delft Report Style, with modifications by Daan Zwaneveld

TU Delft VDL

Preface

This thesis is the culmination of almost 8 months of work, although I could not have done this all on my own. I would like to thank:

- Erik Offerman and Lie Zhao for their supervision, guidance and advice during this project.
- Ruud Hendrikx for performing the X-Ray Diffraction (XRD) measurements for the residual stress profile and processing the corresponding data for this study.
- Ton Riemslag for his help and advice on preparing the samples for XRD measurement of the residual stress depth profile, with the new method using Electronic Discharge Machining (EDM).
- Kees Kwakernaak, Prasaanth Ravi Anusuyadevi, and Prasad Gonugunta for their help in performing the SEM and EDS analyses of the fracture surfaces and the microstructure.
- Saskia van der Meer for all her invaluable help, advice, and support, not only during my thesis project, but during the entire Master programme.

T.S. Meisters
Delft, December 2023

Abstract

VDL Weweler has developed a novel heat treatment approach for their trailing arms, which eliminates the traditional austenisation step and instead capitalises on the inherent heat used for hot-forming to austenise the steel before quenching. This not only saves energy, but surprisingly also improves the lifetime of the products. The underlying reasons for this improvement in fatigue life are the central focus of the present study. Two trailing arms were used for this study, one from the traditional 'Reference' process, and one from the new 'Gasloos' process. Both were produced from the same heat of raw 51CrV4 steel bars that are inductively heated to 1200°C before hot-forming, after which Gasloos is immediately quenched to 180°C. Reference is left to cool to 600°C before being reheated in a gas oven at 900°C for one hour and is finally also quenched to 180°C. After quenching, both are tempered at 450°C for one hour, quenched to room temperature, and shot peened. Reference also underwent the usual painting procedure, Gasloos was collected before this. Both underwent fatigue bending tests, where the Gasloos trailing arm lasted about seven times longer. Fracture surfaces and unfatigued parts were collected from both trailing arms for analysis. Since it was obvious early on that the Reference trailing arm has a partially intergranular fracture, a literature survey was performed to assess the possibility that grain boundary segregation and embrittlement would occur. Scanning Electron Microscopy (SEM) combined with Energy Dispersive X-Ray Spectroscopy (EDS) was used to perform fracture and microstructural analysis, as well as to measure grain boundary segregation. X-Ray Diffraction (XRD) analysis was used to measure the depth profiles of the residual stress to assess the effectiveness of the shot-peening. Samples for XRD were cut using Electronic Discharge Machining (EDM). In both trailing arms, cracks initiated on slag inclusions present from the steelmaking process. Reference initiated on an inclusion 10μm in size, while Gasloos initiated on an inclusion 45μm size, 4.5 times bigger. Slag inclusions are on average 16.09μm in size. The Reference fracture surface is 16% intergranular, while Gasloos is fully transgranular. Carbide density on the PAGB is more than twice as high in Reference, while overall carbide density is 10% higher in Gasloos. Solute segregation to the PAGB could not be measured with EDS. XRD analysis shows that the compressive residual stress from shot-peening is 1.5 times higher and twice as deep in Gasloos compared to Reference. This is due to the oxide scales, containing 17.49 weight% oxygen, that comprise the surface of Reference, making it very brittle and filled with voids. Gasloos does not have these oxide scales at the surface.

Contents

List of Figures

List of Tables

1 Introduction

Steel trailing arms serve as essential components within vehicle suspension systems, influencing both ride comfort and safety. To meet the ever-evolving demands placed on the automotive industry to reduce the impact on the environment placed by both their production and the product itself, VDL Weweler has devised a novel heat treatment approach for their trailing arms. This innovative approach, unlike conventional quench and tempering techniques, eliminates the traditional austenisation step by capitalising on the heat already used for hot working. Not only does this boast significant environmental benefits by reducing energy consumption and greenhouse gas emissions, it surprisingly also yields profound improvements in fatigue life.

Traditionally, austenisation of the steel has been an integral part of the quench and tempering process. However, this new method reimagines the process, utilising the inherent heat used for the initial hot working phase to fully austenise the steel prior to subsequent quenching. This eliminates the need for a gas oven, which consumes substantial amounts of natural gas, thus earning this novel heat treatment approach the nickname ”Gasloos” , which translated from Dutch means ”Gasless” or ”without gas”. In fact, this innovation saves VDL Weweler between 30 and 40 thousand cubic metres of natural gas per month, a remarkable reduction with notable implications for the environment. Furthermore, the remaining heating steps involved in this process are powered by electricity, which can potentially be sourced from renewable and sustainable energy sources, aligning the method with a carbon-neutral trajectory. Beyond its ecological advantages, this novel approach also demonstrates exceptional improvements in the fatigue life of the steel trailing arms. Compared to the traditional heat treatment process, the trailing arms produced through this innovative technique exhibit fatigue life extensions that range from two to six times longer in controlled fatigue tests. The underlying reasons for this remarkable enhancement in fatigue life remain a subject of intrigue and scientific inquiry and form the central focus of the present study.

For the purpose of this inquiry, a trailing arm was randomly chosen from each heat treatment approach for fatigue testing. Both trailing arms were produced from the same batch of 51CrV4 steel, the chemical composition of which can be found in table 1.1. The exact number of cycles to failure for both trailing arms is not disclosed by VDL Weweler; what is shared, however, is that the Gasloos-produced trailing arm lasted about seven times longer than the Reference-produced trailing arm in this case. From these trailing arms, the fracture surfaces are provided, as well as additional material cut from the far end of the trailing arms for further analysis.

C	Si	Mn	P	S	Cr	Ni	Mo	V	Cu	Al	Sn
0.54	0.22	0.98	0.010	0.011	1.15	1.13	0.03	0.14	0.19	0.010	0.012

Table 1.1: Chemical composition of 51CrV4

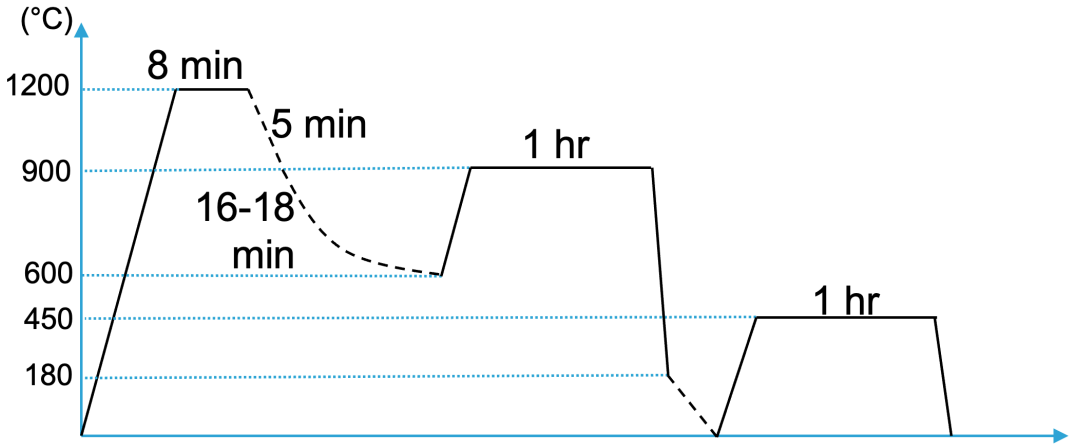

Figure 1.1: Reference Heat Treatment

1.1. Heat treatment variations

Reference Heat Treatment

The original heat treatment for the trailing arms in question, referred to as the 'reference' heat treatment from now on, mostly follows the general outline of a standard quench and temper treatment:

1. The raw 51CrV4 steel bars are induction heated to 1200° C, and held at that temperature for 8 minutes.
2. The hot steel bars are made into trailing arms by hot rolling, eyemaking, and punching in about 5 minutes, during which time they will cool to around 900° C.
3. The trailing arms are left to cool in the open air to around 600° C in around 16 to 18 minutes.
4. The trailing arms are placed in an oven for about an hour at 900° C for austenisation. The oven is filled with endothermic gas, with the purpose of shielding the trailing arms from corrosion and carburising the surface of the trailing arms.
5. The now austenitic steel is quenched in salt water to 180° C to create martensite, and then air cooled to room temperature.
6. To relieve some internal stress, the trailing arms are tempered at 450° C in salt baths.
7. After tempering, the trailing arms are once again quenched close to room temperature (60° C) and progressively rinsed in several water baths to remove the salt.
8. The trailing arms are shot-peened, a method by which a residual compressive stress is introduced at the surface to prevent fatigue crack nucleation and, in turn, extend the fatigue life.
9. Finally, the trailing arms are coated with an expoy-ester coating to protect against corrosion.

Gasloos Heat Treatment

The novel 'gasloos' heat treatment approach differs only from this by skipping the austenisation oven. Instead, it capitalises on the heat already used for hot forming to austenise the steel, before immediately quenching to the martensitic state.

1. The raw 51CrV4 steel bars are induction heated to 1200° C, and held at that temperature for 8 minutes.
2. The hot steel bars are made into trailing arms by hot rolling, eyemaking, and punching in about 5 minutes, during which time they will cool to around 900° C.
3. The still austenitic steel is quenched in salt water to 180° C to create martensite, and then air cooled to room temperature.
4. To relieve some internal stress, the trailing arms are tempered at 450° C in salt baths.
5. After tempering, the trailing arms are once again quenched close to room temperature (60° C) and progressively rinsed in several water baths to remove the salt.
6. The trailing arms are shot-peened, a method by which a residual compressive stress is introduced at the surface to prevent fatigue crack nucleation and, in turn, extend the fatigue life.
7. Finally, the trailing arms are coated with an expoy-ester coating to protect against corrosion.

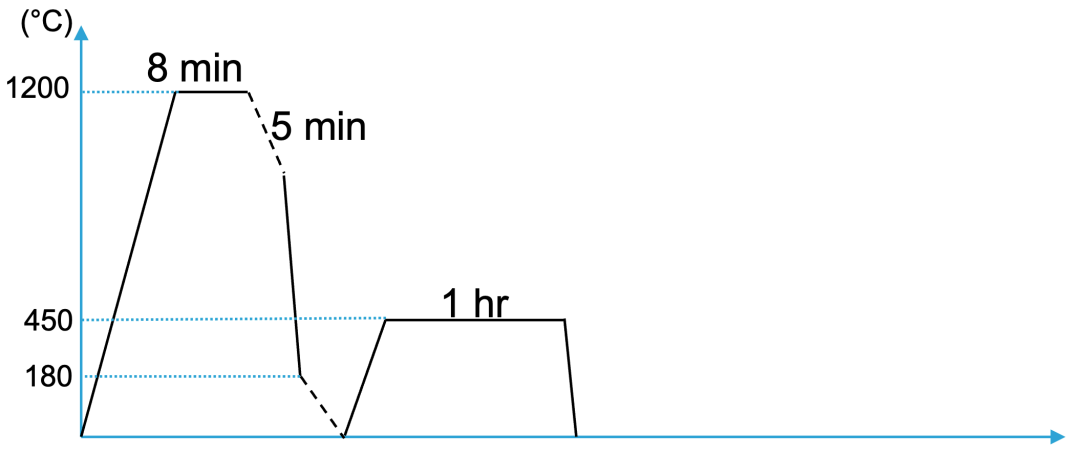

Figure 1.2: Gasloos Heat Treatment

1.2. Notable differences between trailing arms

The first aspect to investigate is the difference in the fracture mode observed in the trailing arms produced with the novel heat treatment approach. Parts of the fracture in the trailing arm produced by the traditional heat treatment process follow the grain boundary, which is also called intergranular fracture, suggesting that the grain boundary is significantly weakened or embrittled. This is in contrast to the trailing arms produced with the novel heat treatment approach, which have a fully transgranular fracture surface. Here lies the biggest difference: In the trailing arms produced with the novel heat treatment approach, the grain boundaries are strong enough to provide a potential barrier that propagating fatigue cracks need to overcome, whereas in the traditional heat treatment process, the weakened grain boundary provides a path of lesser resistance to crack propagation, thus easing the subsequent propagation of said fatigue cracks, leading to a lower fatigue life. Therefore, the present study will investigate how this embrittled grain boundary is mitigated by the different austenisation processes and how this improves the fatigue life of the trailing arms. It must, of course, be acknowledged that embrittlement of the grain boundary can almost never be attributed to one single embrittlement mechanism, let alone to a couple of embrittlement mechanisms. Therefore, the present study will attempt to highlight the most probable and influential mechanisms that contribute to the overall embrittlement of the grain boundary in question, while acknowledging that other mechanisms outside of the scope of the present research could potentially also play a role, although smaller.

The second aspect to investigate is the surface of the trailing arms. After the hot-forming of the trailing arms, which for Gasloos is also the austenisation phase of the heat treatment, the trailing arms are covered in a layer of oxide scales. This layer forms during hot-forming due to the exposure of the trailing arms to the regular atmosphere at the high temperatures experienced during this phase of the heat treatment. From this point forward, nothing is intentionally done to remove this layer, meaning that for the Reference treatment these oxide scales are left there during the recrystalisation and austenisation phase of the heat treatment, effectively fusing to the trailing arm and forming an oxide layer on the trailing arms. For the Gasloos heat treatment, the almost immediate quenching of the trailing arms after hot-forming incidentally results in the oxide scales being washed off, leaving a fresh steel surface on the trailing arms. This difference in surface ”quality,” so to speak, may translate to a profound difference in effectiveness of the shot-peening treatment following at the relative end of the manufacturing process, which in turn can have a drastic impact of the overall fatigue life of the trailing arms. The present study will thus aim to quantify this difference in shot-peening effectiveness, to further explain the difference in fatigue life.

1.3. Aim of research

As was already alluded to in the previous section, the present study aims to answer two central research questions pertaining to the problem at hand, those being:

1. How does the austenisation procedure influence the grain boundary embrittlement due to solute segregation, and the subsequent nucleation and growth of fatigue cracks in 51CrV4 spring steel?
2. How does the austenisation procedure influence the effectiveness of the shot-peening treatment, and the subsequent nucleation and growth of fatigue cracks in 51CrV4 spring steel?

Since this still leaves open the actual approach that will be taken to answer these questions, and this study seeks to identify practical measures that can be used to explain the difference in fatigue life, a number of concise research goals are formulated to help answer the research questions:

- Quantify the difference in the fracture mode.
- Quantify the difference in the amount of carbide precipitates on the prior austenite grain boundary.
- Quantify the difference in the segregation of solute elements to the prior austenite grain boundary.
- Quantify the difference in the residual compressive stress at the surface due to the shot-peening treatment.
- Quantify the difference in composition at the surface.

Of these subquestions, it must be noted that the first three are mainly related to the first main research question, while the last two are more related to the second. To better understand the complex topic of grain boundary segregation and embrittlement, the following two chapters will take a closer look at the literary background of these phenomena. After this, the experimental methodology used in the practical aspect of the present study will be covered, followed by the results, discussion, conclusions, and recommendations for further research. The list of references and supplementary material will be provided at the end of this document.

2

Solute Segregation of Elements to the Grain Boundary

The segregation of solutes at interfaces is a complex phenomenon intimately connected to the thermodynamic properties of these boundary regions. A recent review [1] by Pavel Lejček provides an excellent starting point for the investigation into this subject. Interfaces, because of their unsaturated bonds, exhibit a higher Gibbs energy compared to single crystals. This elevated energy level at interfaces is not constant but depends on a multitude of factors, including the type, orientation, and atomic structure of the interface, as well as the composition, temperature, and pressure of the system. Consequently, these interfaces interact with lattice defects such as dislocations, vacancies, and foreign atoms in an effort to minimise the overall Gibbs energy of the system.

Grain boundaries represent a crucial class of interfaces, and the segregation of solutes at these boundaries can occur through either equilibrium or non-equilibrium processes. In the case of equilibrium segregation, solute atoms tend to occupy sites along the grain boundary that offer a lower Gibbs energy, thereby stabilising the interface. This process is strongly influenced by the thermodynamics of the system and the specific interactions between the solute and the grain boundary, and will be discussed in section 2.2. Non-equilibrium segregation, on the other hand, is contingent upon rate processes and kinetic events within the material. It is important to note that this type of segregation diminishes with time and ultimately approaches an equilibrium state. Non-equilibrium segregation will be covered at the end of this chapter in section 2.3.

2.1. Prelude - Mathematical Predicition of Segregation Behaviour

Although mathematical definitions of segregation models will be given, these equations are provided only to illustrate the general working of the important mechanisms of segregation and will not be used to predict segregation behaviour, as this is beyond the scope of the present study. Initially, it was decided that it would be preferred that the explanation for the increase in fatigue life of the trailing arms be provided through physical experimentation. The fact is that the actual mathematical prediction of segregation in metals can be an entire study on its own, if not several. This may already become obvious when looking at the parameters required in the Guttmann model (see equation (2.6)). The interaction parameter is different for every solute, in every matrix element, and for every crystallographic structure that this matrix element can take. Up until now, the values for these parameters for different ternary systems in particular matrices have only been found empirically, meaning that, for accurate prediction of segregation behaviour in a complex alloy, a multitude of experiments should be performed to acquire the necessary interaction parameters.

2.2. Equilibrium Segregation Mechanisms

2.2.1. Segregation Isotherms (Gibbs)

In its essence, grain boundary segregation differs only from other types of interfacial segregation in terms of the values taken by certain thermodynamic parameters, which comes primarily from the difference in chemical bonding and crystal structures [2]. The first and simplest type of isotherm that describes equilibrium segregation in a binary system with matrix element M and solute I is the Gibbs adsorption isotherm [3]:

$$\Gamma_{I,M}^{\Phi} = -\frac{1}{RT}\left(\frac{\partial\sigma}{\partial \ln X_I}\right), X_I \ll 1 \tag{2.1}$$

This defines a simple approximation of the grain boundary adsorption $\Gamma_{I,M}^{\Phi}$ on the change of grain boundary energy σ and molar fraction of the solute X_I for dilute solutes. The quantity $\Gamma_{I,M}^{\Phi}$ was first introduced using the more descriptive term of "surface density of the solute I at the interface" by Gibbs; it was McLean [4] who later revised it to the now accepted term of "grain boundary adsorption" or "adsorption" in short. This quantity represents the surface density of the solute I at the interface and is defined as:

$$\Gamma_I^{\Phi} = n_I^{\Phi}/A^{\Phi} \tag{2.2}$$

which is the amount of solutes at the grain boundary n_I^{Φ} normalised by the grain boundary area A^{Φ} for binary systems. To describe both binary and multi-component systems, it may be useful to normalise this with the bulk concentration as well as the maximum grain boundary concentration. This is called the grain boundary enrichment ratio, which is the ratio between the concentration of solutes at the grain boundary and the concentration of solutes in the bulk, and is defined as:

$$\beta_I^{\Phi} = \frac{X_I^{\Phi}}{X^0 X_I} = \frac{\Gamma_I^{\Phi}}{\Gamma^0 X_I} \tag{2.3}$$

in which the superscript 0 describes the maximum, meaning Γ^0 is the maximum amount of solutes in one mono-atomic layer in a close packed structure, and X^0 is the maximum grain boundary atomic concentration [1]. This then equates to the so-called grain boundary enrichment ratio, which is often used when describing non-equilibrium segregation, which will be covered in section 2.3.

The Gibbs adsorption isotherm was successfully applied to early experiments on grain boundary segregation, although it proved difficult to measure the grain boundary energy as a function of temperature and bulk concentration simultaneously [1]. It is able to accurately describe segregation in binary and "pseudobinary" systems, which are systems in which there are two solutes that do not interact with each other, as is the case for two solutes that occupy different lattice sites (substitutional and interstitial), for example.

2.2.2. Site Competition (Langmuir-McLean)

The second type of isotherm that describes grain boundary segregation is the so-called Langmuir-McLean type isotherm, named after the Langmuir-McLean model from which most of these models are derived. This model itself find its origin in the publication by McLean [4] mentioned earlier, and is an analogue of Langmuir's model for adsorption to free surfaces, adapted by McLean to work for grain boundaries instead and thus named the Langmuir-McLean model:

$$\frac{X^{\Phi}}{1-X^{\Phi}} = \frac{X}{1-X}\exp\left(-\frac{\Delta u}{kT}\right) \tag{2.4}$$

where Δu is the molar internal energy of segregation, defined as the difference in internal energy between solutes in the lattice and the grain boundary. In this derivation, it is assumed that all of the solutes take substitutional sites in the lattice and at the grain boundary. However, incorporating the effect of interstitial solutes is less straightforward than may be expected because the larger free volume at grain boundaries allows larger atoms than usual to occupy interstitial sites at the grain boundary than is to be expected in the crystal lattice of a matrix material. This is of particular relevance in steel when considering elements such as phosphorus, tin, and antimony in a bcc iron matrix, which take substitutional sites in the bulk lattice but can occupy interstitial sites at the grain boundary. Lejček

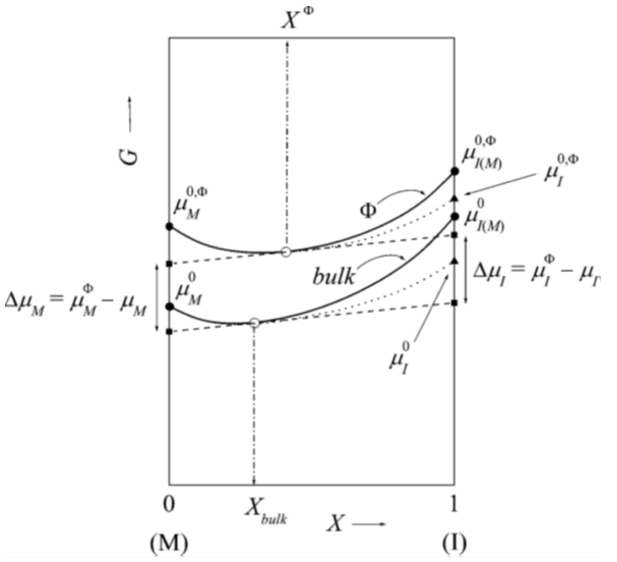

Figure 2.1: Concentration dependence of bulk Gibbs energy and grain boundary Gibbs energy that leads to Gibbs energy of segregation. Depicted also are the chemical potential of the solute element I in the bulk $\mu^0_{I(M)}$ and at the grain boundary $\mu^{0,\Phi}_{I(M)}$, as well as the chemical potential of the matrix element M in the bulk μ^0_M and at the grain boundary $\mu^{0,\Phi}_M$. Equilibrium concentration X^Φ_I follows from the tangent to G^Φ parallel to the tangent of G^{bulk} in X_I, which satisfies the condition $\Delta G = \Delta\mu_I - \Delta\mu_M = 0$. Reproduced from Lejček [1].

solves this by defining an extra sublattice at the boundary for grain boundary interstitials. Integrating this approach into the Hondros and Seah [5] variant of the Langmuir-McLean isotherm, it gives the following expression:

$$\frac{X^\Phi_I}{1-\sum_{i=1}^{M-1} X^\Phi_i} = \frac{X_I}{1-\sum_{i=1}^{M-1} X_i} \exp\left(-\frac{\Delta G^0_I + \Delta G^E_I}{RT}\right) \tag{2.5}$$

Here $\Delta G^0_I = \left(\mu^{0,\Phi}_{I(M)} - \mu^0_{I(M)}\right) - \left(\mu^{0,\Phi}_M - \mu^0_M\right) \neq 0$ is defined as the standard molar Gibbs energy of segregation, which depends on the chemical potential of the solute element I in the bulk $\mu^0_{I(M)}$ and at the grain boundary $\mu^{0,\Phi}_{I(M)}$, as well as the chemical potential of the matrix element M in the bulk μ^0_M and at the grain boundary $\mu^{0,\Phi}_M$. This is best visualised in figure 2.1. If applied to an ideal, infinitesimally diluted, (pseudo)binary system, it can be assumed that the excess molar Gibbs energy of segregation $\Delta G^E_I = 0$ [1], and then equation (2.5) forms the basis for describing site competition between segregating solutes in an ideal dilute multi-component system.

2.2.3. Attractive or Repulsive solute Interaction (Guttmann)

Site competition is not the only type of interaction that two solutes can have, as some solutes attract and others repel one another. Distinguishing between repulsive interaction and site competition is difficult when considering solutes that occupy the same lattice site; however, because site competition does not occur between solutes that occupy different lattice sites, a clear repulsive interaction can be measured for these pairs. The model proposed by Guttmann [6] in 1979 accounts for both site competition and interaction between solutes in non-ideal multi-component systems and still stands to this day. To account for non-ideal systems, it cannot be assumed that $\Delta G^E_I = 0$ in equation (2.5), and instead they proposed the following equation:

$$\Delta G^{\mathsf{E}}_I = -2\alpha^\Phi_{IM}\left(X^\Phi_I - X_I\right) + \sum_{J\neq I,M} \alpha'^\Phi_{IJ}\left(X^\Phi_J - X_J\right) \tag{2.6}$$

Here, α^Φ_{IM} is the interaction between solute element I and matrix element M, and α'^Φ_{IJ} is the interaction between solute element I and another solute element J, where $\alpha'^\Phi_{IJ} > 0$ equates to repulsive interaction, and $\alpha'^\Phi_{IJ} < 0$. It should also be noted that α'^Φ_{IJ} is the net interaction between the solutes with respect to their interaction with the matrix element and structure.

2.3. Non-Equilibrium Segregation Mechanisms

Two primary mechanisms of non-equilibrium grain boundary segregation may be relevant to the present study: thermally induced segregation and segregation due to the migration of grain boundaries. The former is influenced by temperature gradients and thermal fluctuations that drive the redistribution of solute atoms along grain boundaries. The latter involves coupled processes of segregation and grain boundary migration, where the movement of grain boundaries contributes to the redistribution of solutes. The descriptions of both are largely sourced from Lejček [1].

2.3.1. Thermally Induced Grain Boundary Segregation

The main process by which non-equilibrium segregation occurs is through the generation of point defects. One way to generate additional point defects occurs during the quenching process after a heat treatment, leading to vacancy supersaturation. Upon subsequent moderate-temperature heating, non-equilibrium redistribution of vacancies occurs within the microstructure, with vacancies moving towards grain boundaries due to their efficiency as vacancy sinks. Because of the tendency for vacancies in the matrix, especially in the case of significant misfit of the solute-solvent complex, to form impurity-vacancy complexes, an enrichment of regions near the grain boundaries occurs on a nanometric scale. This non-equilibrium state can be negated with sufficient time at these moderate temperatures, erasing the effects of segregation.

Faulkner [7] developed an effective model describing this mode of non-equilibrium segregation. Apart from a general formula for grain boundary enrichment (a general description for grain boundary segregation that was introduced in section 2.2.1), they came up with an expression for the so-called critical time

$$t_{\mathsf{c}} = \frac{d^2 \ln\left(D_{\mathsf{c}}/D_{\mathsf{l}}\right)}{4\delta\left(D_{\mathsf{c}} - D_{\mathsf{l}}\right)} \tag{2.7}$$

which is either the minimum time for slow quenching or minimum tempering time that is needed to negate these non-equilibrium segregation effects in the material. In this equation, d is the grain size, D_c and D_I are the vacancy-impurity complex and bulk impurity diffusivities and $\delta \approx 5 \times 10^{-2}$ is a constant [7]. Although Lejček [1] highlights several studies that support the accuracy of this metric, an important observation that must be made is that the diffusivity parameters are empirical quantities that are not only different for both solutes and the respective matrix material, but also vary with temperature. The temperature dependence may be trivial in the sense that diffusivity increases with temperature and thus the rate at which this non-equilibrium segregation takes place increases, shortening the critical time. The main limitation lies in the empirical nature of the diffusivity coefficients, which may hinder the practical application of this model.

2.3.2. Grain Boundary Migratory Segregation

Although the dragging effect of solute atoms is most often investigated in the context of slowing grain boundary migration, it might be thought that, analogues to something as simple as Newton's third law of motion [8], the migration of a grain boundary has an equal and opposite effect on the solutes. This could then result in the drag of solutes along with the migration of grain boundaries at speeds significantly higher than those suspected by regular diffusion. Gottstein and Shvinderlerman [9] derived the following distribution profile for 1D steady-state grain boundary migration:

$$\begin{aligned} X_I^{\Phi} &= X_I \frac{D_I + bv}{D_I \exp\left(-H_0/kT\right) + bv} \geq X_I \\ X_I &= 1 - \frac{D_I bv\left(1 - \exp\left(-H_0/kT\right)\right)}{\left(D_I + bv\right)\left(D_I \exp\left(H_0/kT\right) + bv\right)} \end{aligned} \tag{2.8}$$

Here, a is the matrix atom diameter, b the solute atom diameter, v the grain boundary velocity, D_I the diffusivity of solute I, and H_0 is the activation enthalpy of diffusion through the grain boundary interface. When plotted, it shows the asymmetric concentration profile as seen in figure 2.2

Cha et al. [10] obtained similar results through the construction of a phase field model. They showed the influence that velocity has on the concentration profile around the grain boundary, which can be observed in figure 2.3.

These studies are only two examples of many studies that investigated the solute drag of migrating boundaries. Although it would be interesting to further analyse studies that investigate this phe-

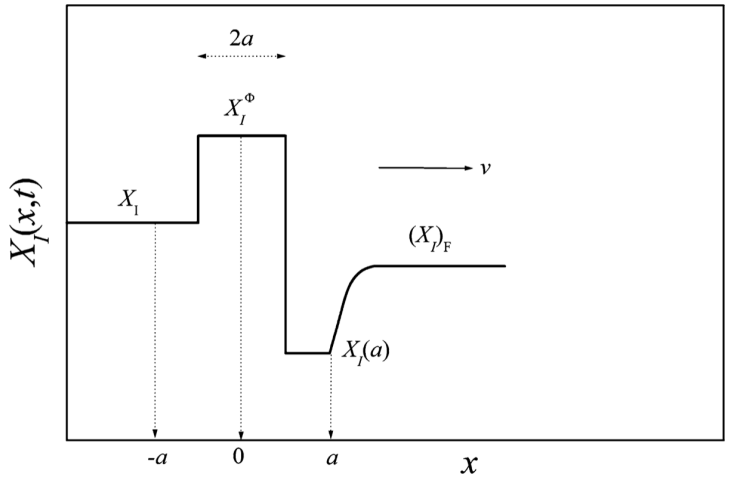

Figure 2.2: Concentration distribution produced by steady-state grain boundary migration according to the model by Gottstein and Shvinderlerman [9], reproduced from Lejček [1].

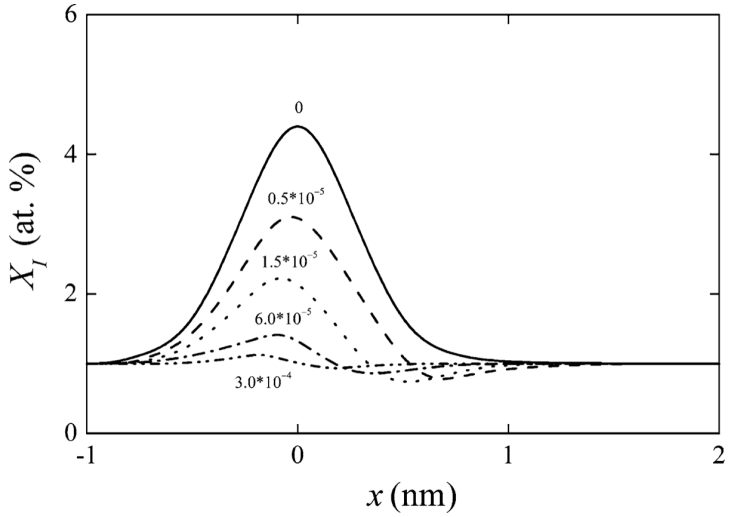

Figure 2.3: Concentration distribution produced by steady-state grain boundary migration according to the phase field model by Cha et al. [10], reproduced from Lejček [1].

nomenon, the effort would be futile in the context of the present study. The reverse effect of non-equilibrium segregation to moving grain boundaries is much higher than is expected from these models, particularly for cases such as recrystalisation or grain growth. This is explained by observing that these models are one-dimensional and are thus unable to account for expanding width of these boundaries that occur during these processes. To accurately describe the reverse phenomenon, Zhang et al. [11] came up with the following expression:

$$\beta_I^{\Phi} = 1 + \frac{\delta}{v} \exp\left(\frac{U_0}{RT} - 1\right) \tag{2.9}$$

This expression for the grain boundary enrichment ratio includes U_0, which is the potential of the solute atoms near the grain boundary, as well as an expression for the width of the grain boundary $\delta = \delta_0 + v\tau\delta_\tau\Delta\rho$. In another study by the same author [12], the enrichment ratio for Boron in a Fe-3%Si alloy was measured as 1.6, while this model predicts an enrichment ratio of 1.7, showing that for this particular alloy, the results of the model agree with the experimental results. In this study, it was also shown that with decreasing boundary migration velocity, the levels of segregated boron decreased. Thus, it seems that the expansion of the growing grain boundary provides the extra driving force needed to explain these elevated levels of segregation, which the model also adequately describes.

3

Grain Boundary Embrittlement

The grain boundary energy is altered by a number of different phenomena related to the intentional or unintentional addition of other elements to steel. These can enhance the grain boundary cohesion or deteriorate it, possibly leading to the grain boundary becoming brittle. This chapter will discuss the relevant grain boundary phenomena for the present study. First, the influence of elements in solid solution will be discussed in section 3.2. For elements in larger concentrations, the possibility of forming separate phases on the grain boundary is also a possibility that must be considered, which will be discussed in section 3.3.

3.1. Terminology clarification and unification

When discussing these phenomena, the literature often uses terms such as temper embrittlement[13, 14, 1, 15, 16, 17], tempered martensite embrittlement[13, 18, 19], 350C/500F embrittlement[13, 14, 18, 20, 21], 500C embrittlement[13], one-step (temper) embrittlement[20, 21] or two-step (temper) embrittlement[20, 21] to refer to one, the other, or even both of these phenomena. Although there seems to be somewhat of a consensus formed, these terms are still misused frequently, since the names chosen are somewhat confusing or even misleading. Where the last two terms are clearly named after the heat treatment steps that were used that lead to the subsequent embrittlement, and the middle two refer to the tempering temperature that preceded the embrittlement, the first two seem very similar in their naming and are thus sometimes mistakenly used interchangeably, even though they are mostly used to refer to two seemingly different phenomena. The use of the word ”seemingly” here is appropriate, since the current state of research into these phenomena has made it clear that these phenomena are, in fact, not that different at all. Both are a result of the segregation of (different) solute atoms to the grain boundary, while showing somewhat different characteristic symptoms, but both leading to the embrittlement of the grain boundary. To provide some clarity throughout this study, it is stated (in accordance with [13, 17, 20]) that:

- Tempered martensite embrittlement, 350C/500F embrittlement or one-step (temper) embrittlement refers to the intergranular fracture caused by the precipitation of cementite along the prior austenite grain boundary due to segregation of *alloying elements* to the grain boundary.
- Temper embrittlement, 500C embrittlement or two-step (temper) embrittlement refers to the weakening of the grain boundary by segregation of *impurities* to the grain boundary, weakening the grain boundary and leading to intergranular failure to become the predominant mode of fracture.

This group these terms into two distinct phenomena; grain boundary embrittlement due to the weakening of the grain boundary by solute segregation, and grain boundary embrittlement due to the preferential precipitation of carbides due to solute segregation. However, the further distinction that the weakening of the grain boundary is due only to impurity segregation and that only alloying elements play a role in embrittlement due to the preferential precipitation of carbides is shown to be shortsighted in this chapter. Because of this, combined with the fact that both phenomena are not that different, and basically two symptoms of solute segregation to the grain boundary, more recent publications have

started to refer to both together as 'temper embrittlement' after all. However, since this remains a possibility for further confusion, it is decided that the use of these terms will be avoided wherever possible from here on.

3.2. Effect of solute elements on the grain boundary interface

Although the effect of elements on embrittlement in steel is well known, the exact cause of this phenomenon is still being debated. In fact, grain boundary embrittlement due to solute segregation can actually occur quite often, although it becomes pronounced only in metals with a very strong grain interior [17]. The same review as mentioned in chapter 2 by Lejček [1] also providing an outstanding starting point for this part of the literature survey. In this review, the author answers two important questions related to the problem at hand:

1. Why do certain elements weaken or strengthen the cohesion between grains, i.e. weaken or strengthen the grain boundary interface?
2. What is the relative potency of these elements?

3.2.1. Embrittling effect of certain elements on the grain boundary

To determine the effect of the solute elements on grain boundary cohesion, their effect on the ideal work of grain boundary fracture γ must be understood, which is essentially the energy needed to break the bonds across the grain boundary. The ideal work of fracture of a pure grain boundary is described by McLean [4]:

$$\gamma^0 = 2\sigma^{\mathrm{s},0} - \sigma^{\Phi,0} \tag{3.1}$$

where $\sigma^{\mathrm{s},0}$ is the free surface energy of the pure material and $\sigma^{\Phi,0}$ is the surface energy of the non-segregated grain boundary. For most metals, it turns out that $\sigma^{\Phi,0} \approx \sigma^{\mathrm{s},0}/3$, with the ideal work of fracture of a pure grain boundary being only about 5/6 that of a crystallographic plane. Here Lejček [1] claims that this does not necessarily mean that intergranular fracture is automatically the preferred mode of fracture in most bcc metals. The preferred fracture mode depends also on the orientation of the slip planes and the surface energy of the low-index cleavage planes. This makes cleavage fracture more likely in pure bcc metals.

The main dependence between the ductile and brittle failure of a pure metal is temperature. At higher temperatures, dislocation movement is easy, enabling plastic deformation and eventually leading to ductile failure of the material. On the other hand, at lower temperatures, dislocation movement is difficult, hindering plastic deformation and leading to brittle failure of the material. The temperature where this changeover happens is called the Ductile-to-Brittle-Transition-Temperature (DBTT). When grain boundary cohesion is reduced, the fracture energy for the brittle fracture beneath the DBTT is reduced. This leads to an increase in the DBTT, which is schematically shown in figure 3.1. From this, it can be concluded that the segregation of solute elements to the grain boundary can potentialy cause the failure mode to change from ductile to brittle fracture, under the condition that the operating temperature is above the old and beneath the new DBTT.

The effect of segregated solute elements on the ideal work of grain boundary fracture γ can be described by two different equations, both of which end in the same result. The first by Hirth and Rice[22] describes the effect on the ideal work of fracture using the grain boundary and the surface chemical potential of the solute element, and is given by

$$\gamma = \gamma^0 - \int_0^{\Gamma_I^\Phi} \left[\mu_I^\Phi(\Gamma) - \mu_I^{\mathrm{s}}(\Gamma/2)\right] \mathrm{d}\Gamma \tag{3.2}$$

where μ_I^Φ and μ_I^{s} are the grain boundary and surface chemical potential of solute I in equilibrium with a level of grain boundary adsorption Γ_I^Φ, that is, the quantity of species I with chemical potential μ_I per unit area of the interface. This equation is then rewritten by Lejček [1] (with no intermediate steps given) to

$$\gamma = \gamma^0 + \Gamma_I^\Phi \left(\Delta G_I^{\mathrm{s}} - \Delta G_I^\Phi\right) + RT \int_0^{\Gamma_I^\Phi} \ln \frac{\Gamma_{I,\mathrm{max}}^\Phi - \Gamma}{\Gamma_{I,\mathrm{max}}^{\mathrm{s}} - \Gamma} \mathrm{d}\Gamma \tag{3.3}$$

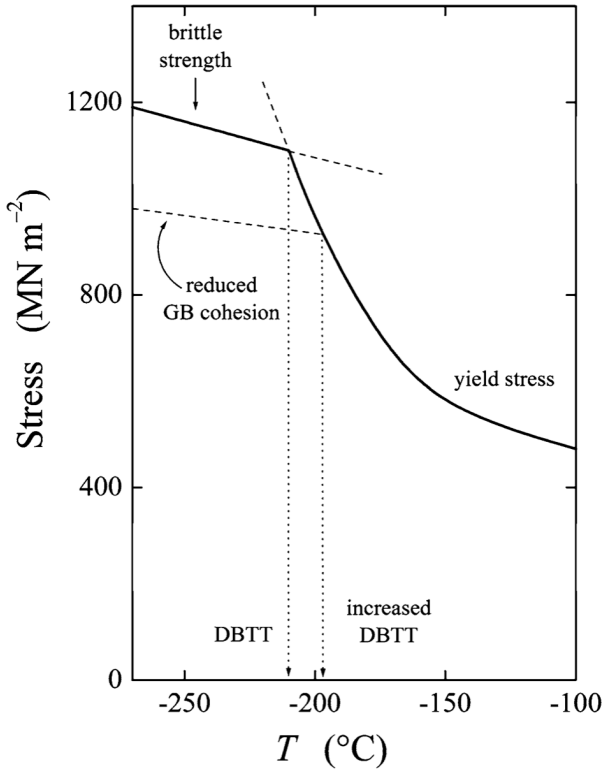

Figure 3.1: Schematic representation of the increased DBTT caused by a reduction in grain boundary cohesion for 0.2% carbon steel, reproduced from Lejček [1]

where $\Gamma^{\Phi}_{I,\mathsf{max}}$ and $\Gamma^{\mathsf{s}}_{I,\mathsf{max}}$ are the maximum levels of adsorption and where ΔG^{Φ}_{I} and $\Delta G^{\mathsf{s}}_{I}$ are the Gibbs energies of segregation of solute I, both at the grain boundaries and surface respectively.

The other approach to describe the effect of segregated solute elements on the ideal work of grain boundary fracture γ by Seah[23] does this by actually evaluating the difference in bond energy across the grain boundary after fracture. It is written as follows:

$$\gamma = \gamma^{0} + \Gamma^{\Phi}_{I}\left(\frac{Z_{\mathsf{g}}}{Z\Gamma^{\Phi,0}_{I}}\right)\left(H^{\mathsf{sub},*}_{I} - H^{\mathsf{sub},*}_{M} - \frac{Z\Omega}{a^{2}_{I}}\right) \tag{3.4}$$

where $\Omega = H_{\mathsf{mix}}/\left[ZX_{I}\left(1-X_{\mathsf{c}}\right)\right]$ with H_{mix} as the enthalpy of mixing, Z and Z_{g} are the bulk and grain boundary coordination number, $H^{\mathsf{sub},*}_{I}$ and $H^{\mathsf{sub},*}_{M}$ are the enthalpies of sublimation of solute I and matrix M, $\Gamma^{\Phi,0}_{I}$ is Γ^{Φ}_{I} at one layer deep and a_{I} is the lattice parameter of the solute I.

When equation (3.4) is written in this form, it is easy to see the similarity to equation (3.3), giving immediate insight into the fact that these different formulae give the same result in the end. Both methods are thus valid to describe the effect of segregated solute elements on the ideal work of grain boundary fracture and thus their effect on grain boundary cohesion and the DBTT.

3.2.2. Relative potency of embrittling elements

It is interesting to conclude from equation (3.3) that the ideal work of grain boundary fracture changes linearly with segregation, and that whether this increases or decreases the ideal work of grain boundary fracture depends on whether these elements segregate more strongly to grain boundaries or free surfaces, respectively. Most importantly, within the context of the DBTT, this suggests that there is a relation that states that [24]

$$\frac{\delta\mathsf{DBTT}}{\delta\Gamma^{\Phi}_{I}} \propto \left(\Delta G^{\mathsf{s}}_{I} - \Delta G^{\Phi}_{I}\right) \tag{3.5}$$

This relationship is an excellent starting point, showing that the presence of different solute elements has a positive or negative effect on grain boundary cohesion and that some elements are more potent in this effect than others. It, however, fails to consider the matrix element and more so describes the grain boundary cohesion of the solute in absolute terms.

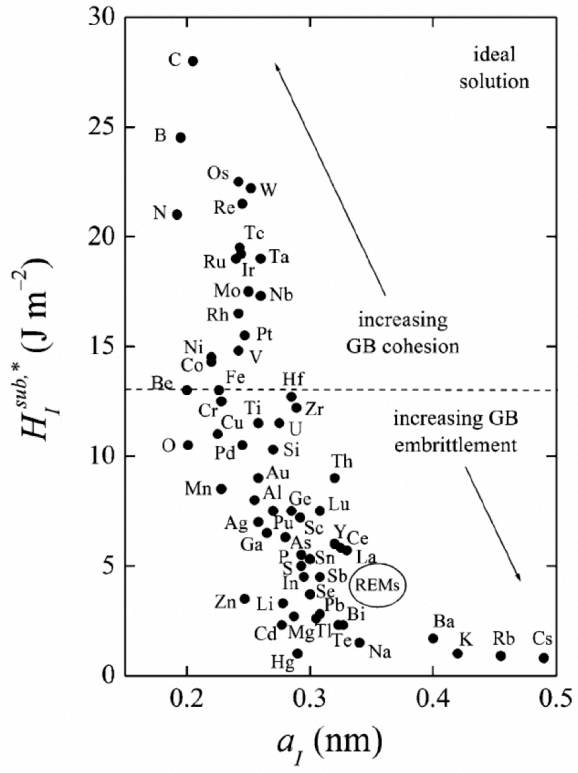

Figure 3.2: Enthalpy of sublimation $H_I^{\text{sub},*}$ of different elements plotted against their lattice parameter a_I. The dashed line represents the enthalpy of sublimation for iron, with elements higher than this enhancing grain boundary cohesion in iron and elements below decreasing it. Reproduced from Lejček [1]

When looking at the effect that a solute I has on the grain boundary cohesion in a material made up mostly of matrix element M, it must be considered how the bond energy of the solute element across a grain boundary relates to the bond energy of the matrix element across a grain boundary. For this reason equation (3.4) provides a more intuitive approach to determine the relative potency of the elements of the solute with respect to the elements of the matrix, since it considers the sublimation enthalpies of both the solute and the matrix, while also considering the bulk and grain boundary coordination number along with the lattice parameter of the solute. When using this equation as an approximation for an ideal solution (thus neglecting the correction factor Ω [23]) for the ideal work of grain boundary fracture, it can be observed that, in general, a solute element is embrittling whenever $H_I^{\text{sub},*} < H_M^{\text{sub},*}$, and that this effect is proportional to $\mid H_I^{\text{sub},*} - H_M^{\text{sub},*} \mid$. The coordination numbers in both the bulk and at the grain boundary, as well as the lattice parameter of the solute, still play a role, but this effect is in most cases a lot smaller. This last fact is most obvious when looking at the relation between enthalpy of sublimation of elements and their respective lattice parameter for example, shown in figure 3.2, where it can be observed that the difference in sublimation enthalpy between solute and matrix is generally multiple orders of magnitude bigger than the lattice parameter of the solute.

3.3. Precipitates on the Grain Boundary

The previous section only considered the interaction of foreign elements in solid solution with the grain boundary. Considering this as the only interaction is generally valid whenever the concentration of these elements is relatively low. Whenever local concentration on the grain boundary becomes higher, either through excessive segregation to the grain boundary and/or high bulk concentration, the possibility that separate phases will precipitate must also be considered. Often, these phases are highly brittle, providing an even easier path for cracks to propagate along, giving the appearance of intergranular fracture since these phases lie on the (prior austenite) grain boundary, while technically being more transgranular in nature. In the case of the present study, this particular question concerns the formation of a thin carbide film along the prior austenite grain boundary, which is discussed in this section.

3.3.1. Formation of Carbides at the grain boundary

The embrittlement due to the formation of carbides on the grain boundary, often referred to as tempered martensite embrittlement (see section 3.1), is a complex phenomenon and the literature offers intriguing insights into this intricate process. Horn et al. [18] summarises that although early explanations of the phenomenon were already focused on the involvement of austenite retained after quenching, these were wrongfully abandoned for two reasons:

- Cooling the samples to sub-ambient temperatures after quenching did not eliminate the embrittlement, since it was falsely assumed that this would remove most of the retained austenite.
- Inability to accredit the sole observation of the intergranular fracture to the transformation of retained austenite, although it was later discovered that fractures due to this embrittlement were not necessarily solely intergranular.

Although acknowledging the efforts leading to this, it seems that Horn et al. [18] was the one who revived the hypothesis that retained austenite plays a significant role in embrittlement due to intergranular carbides, which is still supported today. They attribute this embrittlement to partial thermal decomposition of retained austenite into cementite and subsequent deformation-induced transformation of the remaining austenite into untempered martensite after initial mechanical loading of the material. In this study, it was shown that cementite precipitates directly from the retained austenite, depleting the remaining austenite of carbon and making it mechanically unstable, causing it to transform into untempered martensite the moment it experiences any significant load.

The stabilisation of this austenite also seems to be a symptom of solute segregation during the austenisation process [18]. Elements that are known to stabilise austenite at room temperature, particularly carbon and manganese [25] in 51CrV4, can also segregate to grain boundaries during prolonged austenisation (mechanisms of which will be covered in chapter 2). During the subsequent quenching, the high local concentration of these austenite stabilising elements on the grain boundary retards the formation of martensite that takes place within the rest of the steel, producing a fine film of stabilised austenite within a matrix of martensite, right where the prior austenite grain boundary was previously. As the steel progresses to the tempering phase, the stabilised austenite subsequently decomposes as described in the preceding paragraph.

The precise composition of this carbide film seems to be contingent on the overall composition of the steel and the extent to which these elements have segregated to the grain boundary during the austenisation phase. Horn et al. [18] found that these carbides are cementite in their study, although other publications [19, 17, 26] mention the possibility that they can also be alloy carbides. With the composition of 51CrV4, it is definitely plausible that these carbides manifest themselves as alloy carbides, but not guaranteed.

3.3.2. Rejection of Solutes from Carbides

Though the main focus in the previous section was on segregation of austenite stabilising elements, it should not be forgotten that most of the other elements present in the steel simultaneously still present the possibility of segregation as well. Considering that there already is sufficient segregation of the austenite stabilising elements for stabilisation of the austenite film to occur, it is likely that there are other elements that segregated in large quantities to the retained austenite. During [27] and after [28] the austenite film decomposes, any non-carbide-forming element [14] is ”rejected” from the carbide. This then results in a high concentration of elements at the grain boundary between the carbide and the surrounding matrix. In the event that the solutes rejected from the carbide are relatively embrittling in the matrix element, this results in significant grain boundary embrittlement between the matrix and the carbide, as previously described in section 3.2. This elevated concentration of elements on the carbide/matrix interface can be reduced by keeping the material at elevated temperatures for a prolonged time, and thus the carbide rejection mechanism can be classified as non-equilibrium segregation mechanisms as described in section 2.3.

As embrittlement due to carbide precipitation is a central symptom of tempered martensite embrittlement (as discussed in section 3.1), the theory of solute rejection during or after carbide formation is often discussed in publications on the general phenomenon. Publications by Ohtani et al. [16], Horn et al. [18], Olefjord [14], Briant et al. [20], and Bowen et al. [29] all agree that there is rejection of elements from carbides. However, no clear consensus appears to form on whether the mechanism proposed by Kula and Anctil [28] or Rellick and McMahon [27] is more important, though there does seem to

be a consensus that both can occur, even simultaneously. Kula and Anctil argued that the solutes segregate from the carbide to the surrounding ferrite *after* it formed due to the higher solubility of these solutes in the surrounding ferrite phase, creating a driving force for solid diffusion in an environment where mobility is sufficient due to the elevated temperature during temperature. This would result in a transient build up of solutes in the boundary between the carbide and surrounding ferrite phase. Rellick and McMahon [27] on the other hand argued that because the solubility of these elements is so low in the carbide phase, that most of the solutes are already rejected during the formation of the carbides, with the rest possibly also diffusing out by the mechanism proposed by Kula and Anctil [28].

Interestingly, Briant later refuted the theory of solute rejection from carbides in general in a publication in conjunction with Lewis [26], citing the study by Bowen et al. [29]. They present two problems with the study:

1. ”Boundaries which had sufficient phosphorus segregation to fracture apart after aging at and below 250°C should have even more segregation after rejection has occurred. This should increase the average phosphorus concentration.”
2. ”Boundaries that fracture open in samples aged at 250°C have very similar values of phosphorus segregation to those aged at 350°C.”

The astonishing part of this argumentation is the clear contradiction that these statements have with Briant’s own publication six years earlier [20], in which he himself argues that the majority of segregation occurs during austenisation (this is also supported by[30]). Because the amount of rejected impurities is dictated by the impurity content of the preceding austenite film, which in turn is dictated by the amount of segregation that occurred during austenisation, the tempering temperature is only a factor if it is too low for the destabilisation of austenite to occur or it is too high for the formed carbides to remain stable. Neither is the case here, so the tempering temperature has no influence on the amount of impurities rejected from carbides in the case that the austenisation procedure is identical, invalidating both arguments. Without any other evidence supporting this claim, their rebuttal can be dismissed.

In the end, Horn [18] summarises very well that this scenario, in which embrittling elements are rejected from carbides, compounds the already hard and brittle carbide phase on the prior austenite grain boundary, with a weak boundary between this phase and the matrix, which together act to promote both the nucleation of microcracks due to the cyclical loading and the subsequent growth and propagation of these cracks.

4

Experimental Methodology

In this chapter, a comprehensive description of methodologies is presented to evaluate grain boundary composition, assess the efficacy of shot-peening treatment and characterise microstructural features. The initial section addresses the prerequisites concerning grain boundary composition measurement, elucidating several methodologies, and culminating in the rationale behind the selection of a specific method. Subsequently, the methodology for quantifying the effectiveness of the shot peening treatment is delineated, encompassing sample preparation techniques and the use of residual stress measurement methodologies. The third section focusses on characterising the microstructure and incorporating the possible use of Light Optical Microscopy (LOM) or Scanning Electron Microscopy (SEM) to delve into structural intricacies. Finally, a comprehensive account of the methodology used is provided, which includes exhaustive details on sample preparation methodologies and precise equipment used throughout the investigation process.

4.1. Grain Boundary Composition

Measuring the local composition on the grain boundary is not as straightforward as it may seem when analysed in the context of grain boundary segregation or embrittlement. For these purposes, only several layers of atoms close to the grain boundary are relevant, since these are the only places where elevated concentrations of segregates will arise and where segregates significantly influence the grain boundary cohesion. With this in mind, the requirement for chemical analysis of the grain boundary will be discussed next, followed by the discussion of practical analysis techniques.

4.1.1. Requirements

Due to this particular nature of grain boundary segregation and grain boundary embrittlement, there are specific technical requirements for the experimental investigation of the grain boundary in this context, which were identified and formulated by Hondros [31].

1. High Spatial Resolution

The technique should have a resolution on the same order as the width of a grain boundary in at least one direction, two if heterogeneous distribution within a grain boundary is to be measured. Ideally, the resolution would be on the atomic level.

2. Chemical Identification

The technique should be able to chemically identify any species, with the possible exception of hydrogen and inert gasses. This should be done at least consecutively, but preferably concurrently, and without any prior knowledge of segregated elements.

3. Quantitative Measurement

The technique should be able to quantify any segregated species with a lower level of at least 1%, although a lower detection limit is always preferential.

4. Determination of Chemical Bonding
The technique should be able to characterise the state of chemical bonding of atoms at the grain boundary.

5. Non-exposure of a Grain Boundary by fracture
The technique should be able to measure the quantities mentioned above without fracture of the sample, since this limits the measurements to samples that have strongly embrittled grain boundaries and thus fracture intergranularly. This could be potentially mitigated by cooling the sample below its DBTT; however, this adds even more complexity to an already difficult and time-consuming procedure.

4.1.2. Analysis techniques
From the stringent requirements mentioned above, it may already become obvious that there are very few techniques that can meet all requirements simultaneously. Next, some possible techniques are discussed, some of which unfortunately do not fulfil every single previously mentioned requirement.

Auger Electron Spectroscopy
Auger Electron Spectroscopy (AES) is a powerful analytical technique used to determine the elemental composition of surfaces, as explained by Briggs [32]. It operates on the principle of analysing the energies of Auger electrons emitted when atoms in a sample undergo transitions following the ejection of a core electron. When these electron energies are measured, AES provides detailed information on the elemental composition and chemical state analysis of materials. Its high sensitivity, high spatial resolution, and a shallow analysis depth of only about 5 nm make AES a powerful tool to analyse grain boundary segregation if used on an intergranular fracture surface to measure a grain boundary, which must be created by fracturing the sample under ultra-high vacuum (UHV) to prevent contamination of the grain boundary. This means that AES does not meet the fifth requirement mentioned in section 4.1.1, though this has not prevented the technique from historically being one of the most popular techniques for studying grain boundary segregation. Another limitation due to it being a surface analysis technique is it's inability to measure depth profiles, although it is still possible to measure the difference in segregation between the bulk. Fractures are actually almost never fully intergranular, meaning that if local areas in the fracture surface can be adequately characterised as intergranular and transgranular, then separate measurements can be done both on a grain boundary and in the bulk of a grain. Sadly, although Auger Electron Spectroscopy is an available technique at the Department of Materials Science and Engineering at Delft University of Technology, it cannot be set up to allow samples to be fractured under UHV within the timescale allotted to the present study, and thus using this technique is not possible under these circumstances.

Atom Probe Tomography
Atom Probe Tomography (APT) is another powerful analytical technique used to characterise the three-dimensional arrangement of atoms in materials, as explained by Tsong [33]. It is a type of field ion microscopy (FIM) that uses a focused ion beam to image and analyse the chemical composition of a sample at the atomic level. APT can be used to study a wide range of materials, from metals and alloys to semiconductors and ceramics, and can provide valuable insight into the structure and properties of materials. When used to study grain boundary segregation, it can measure the distribution of atoms in a small volume with a spatial accuracy as low as 0.5 nm, allowing for accurate measurement of the concentration of segregated atoms at the grain boundary. A good example of this can be seen in a recent study by Liu [34], where APT was used to produce a measurement of the linear distribution of segregated manganese perpendicular to the grain boundary. Atom probe tomography is possibly the best currently available technique when it comes to studying even faintly segregated samples; however, it is not yet available at Delft University of Technology, although it will be in the near future. This does, however, rule out its use in the present study.

Energy Dispersive X-ray Spectroscopy
Energy Dispersive X-ray Spectroscopy (EDS) is a technique used to identify the elemental composition of a sample, as explained by [35]. Similar to AES, it works by bombarding the sample with electrons and measuring the energy of the X-rays that are emitted from the sample. This energy is then used to identify the elements present in the sample. EDS is a powerful tool for material characterisation,

as it can provide information on the elemental composition of a sample in a non-destructive manner. Its spatial resolution is very similar to that of AES; however, the depth of the analysis is much higher than that of AES. The bell-shaped analysis volume can be 1-3 μm deep, which makes it unsuitable for measuring grain boundaries on an intergranular fracture surface. From a practical point of view, it is often part of a Scanning Electron Microscopy (SEM) setup (see section 4.3), which is another characterisation technique that will be used in the present study. The diameter of the analysis volume is too large to provide ample spatial accuracy when measuring the grain boundary as a line on a cross section of the microstructure, where it will also measure a large area farther from the grain boundary, which is unlikely to have a higher concentration due to segregation. This will mean that any potential elevated concentration close to the grain boundary will be averaged over a relatively large analysis area, severely limiting the possibility of measuring any segregation to samples containing heavily segregated grain boundaries. This makes this possibly the least suitable technique mentioned in the present study; however, it is the best option currently available at the department and will thus be used to attempt the measurement of grain boundary segregation.

4.2. Shot-Peening Effectiveness

With the difference in surface quality between the trailing arms, combined with the large influence the shot-peening treatment can have on fatigue life, it is essential to quantify the possible difference in the efficacy of this surface treatment. In this section, two possibilities for this measurement will be discussed: microhardness depth profiling and residual stress depth profiling.

4.2.1. Micro-hardness Depth Profile

Although relatively simple to execute, it is difficult to separate the effect of shot-peening on the local hardness near the surface from other possible effects in the material near the surface, most notably decarburisation. Since it cannot be excluded that the change of austenisation procedure also affects the level of decarburisation while simultaneously also changing the effectiveness of the shot-peening treatment, measurement of micro-hardness can only be used to measure the combined effect of both of these changes and is thus unsuitable to solely measure the effectiveness of the shot-peening treatment.

4.2.2. Residual Stress Depth Profiling

Since the primary objective of shot-peening is to induce a local residual compressive stress at the surface, it makes sense to measure the depth profile of this effect directly. Although there are possibly other effects in the production process that may also influence the residual stress, for example from the martensite transformation [36], most of the residual stress measured near the surface will most certainly be from the shot-peening treatment, thus making measurement of the residual stress depth profile a suitable way to quantify the effectiveness of the shot-peening. The standard measurement procedure is described by Kumagai [37], which involves progressively removing layers of the material using electropolishing while intermittently measuring the strain in the crystal lattice by X-Ray Diffraction (XRD). Since this is labour- and time-intensive process, instead a very shallow slope could be cut into the sample using Electrical Discharge Machining. This should induce very little residual stress if done carefully, and in case it is substantial, the effect is homogeneous [38], which means that the measured data can be corrected for this effect.

4.3. Microstructural Characterisation

Microstructural characterisation is the process of studying the microstructure of a material. It is typically done using Light Optical Microscopy (LOM), although Scanning Electron Microscopy (SEM) can also be used. LOM is used to observe the microstructure at a relatively low magnification, while SEM can be used at much higher magnifications. The main objective for the microstructural analysis is to quantify the differences in heterogeneous carbide precipitation on the PAGB, which are relatively small and require a relatively high magnification, making SEM an ideal candidate. Because the SEM setup also includes EDS, it can also be used to identify the chemical composition of the carbides, possibly providing more insight on their origin. These two aspects lead to the decision to use SEM for microstructural characterisation.

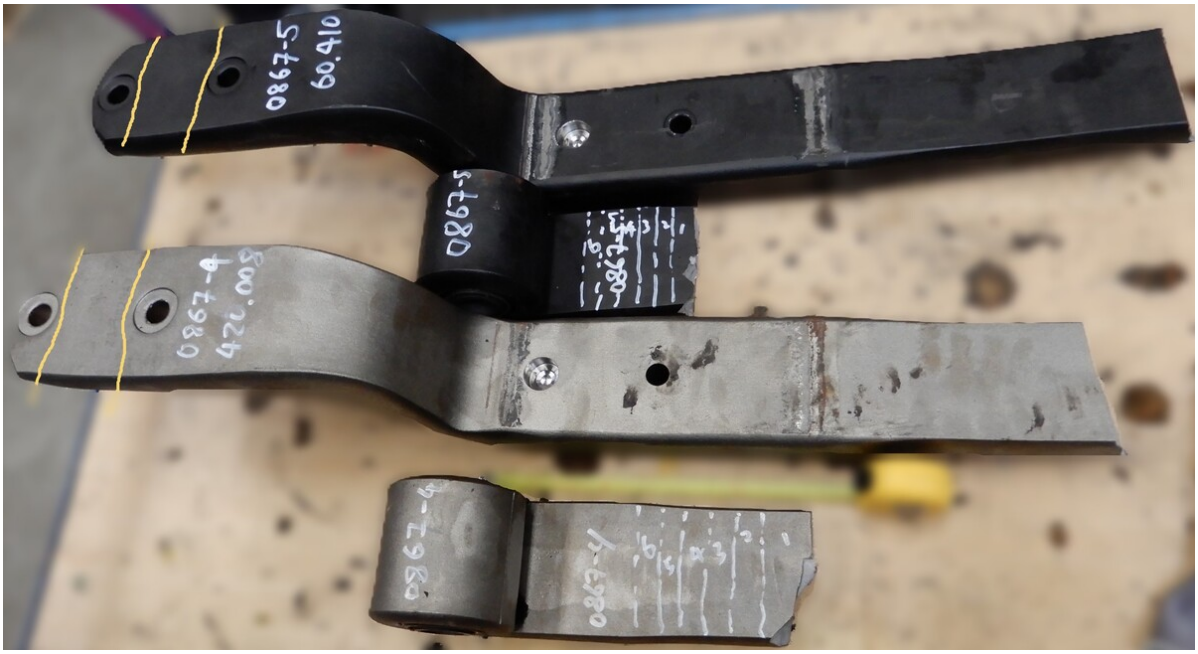

Figure 4.1: Trailing arms after bending fatigue testing. Fracture surfaces were cut from the right end, extra sections of material were cut from the left end indicated with yellow lines.

4.4. Applied Methodology

Sample material was cut from two trailing arms, one produced using the Reference heat treatment approach and another using the Gasloos method. An important distinction that should be mentioned, is that the Reference trailing arm received the usual expoy-ester coating while the Gasloos Both trailing arms did not. Both were subjected to cyclic bending fatigue testing until failure. The fracture surfaces, as well as extra material from the ends of both trailing arms were cut and collected for further analysis as can be seen in figure 4.1. The expoy-ester coating on the material taken from the Reference trailing arm was removed using careful glass-blasting as visible in figure 4.3. The material cut from the ends were cut into further pieces to prepare samples for SEM and XRD analysis which is shown in figure 4.2.

Samples for the SEM were embedded in conductive resin, and were sanded and polished to 1μ using a Struers Tegramin 30, after which they were etched using Nital 2% for 15 seconds. The SEM samples can be seen in figure 4.4a. SEM and EDS analysis was performed using a JOEL JSM-IT100(LA). The sample material for XRD was first measured for residual stress and texture at the shot-peened surface. After this initial measurement, a very shallow slope was cut into the material using EDM, so that residual stress measurements could be performed at depth increments of around $0.05mm$ using XRD. On the other side of the material, a parallel surface was cut using the same process to make sure the sample could be properly mounted in the XRD equipment. The cut samples are shown in figure 4.4b. XRD analysis was performed using a Bruker D8 Discover with Eulerian cradle with parallel beam geometry, with the following settings:

- Incident beam side: polycap (polycapillary optics), divergence 0.25°.
- Diffracted beam side: Parallel sollerslit, divergence 0.35°.
- Graphite monochromator. Co Kα radiation, 45 kV 25 mA. Beam height $2mm$, width $4mm$.
- Scans: Locked coupled 98 - 102° 2θ, step 0.02, time 5 s, sin2psi 0 to 0.5°, steps 0.1, Phi=0.

Data evaluation was done using Panalytical Expert Stress 2.0. The value for residual stress and stress-free lattice parameters were calculated using the $sin^2\psi$ technique [39]. For these steel samples the following X-ray elastic constants were used: $s1 = -1.36$ (1/TPa), $s2 = 6.10$ (1/TPa), $sin^2\psi_0 = 0.446$ (Panalytical Xpert Stress), Modified Lorenztian or Gauss peak shape. Unidirectional stress analysis.

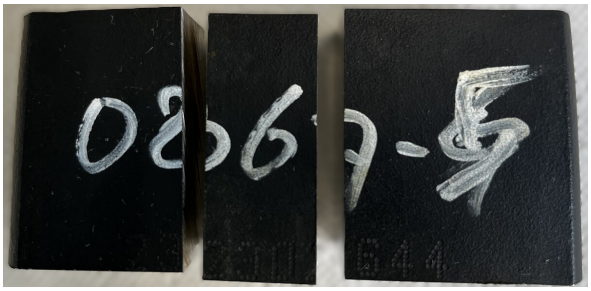

(a) Section from Reference trailing arm, with coating. Left part was used for XRD, sample for SEM was cut from middle part.

(b) Section from Gasloos trailing arm, without coating. Right part was used for XRD, sample for SEM was cut from middle part.

Figure 4.2: Material cut from the trailing arms

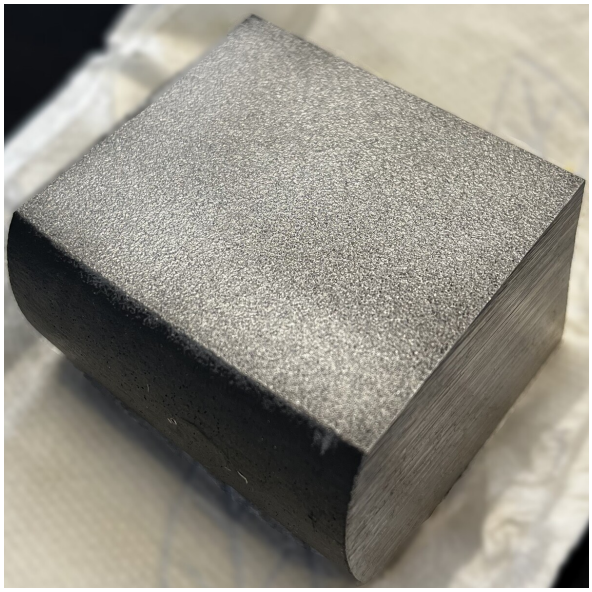

Figure 4.3: Cut material from Reference trailing arm after removal of coating using sandblasting.

(a) SEM samples, Reference is on the left, Gasloos on the right. Cross-sections were cut so that the microstructure is viewed in the rolling direction. The left edge of the sample is the surface edge of the trailing arm.

(b) Residual stress depth profile samples, Reference is on the left, Gasloos on the right. The slope was cut starting from the top edge as pictured here, with the slope ending at a depth of 0.6mm at the edge pictured here at the bottom.

Figure 4.4: Prepared samples

5

Experimental Results

The results of the experiments carried out, as described in the previous chapter, will be covered in this chapter. First, SEM images taken for the analysis of the fracture surfaces of the Reference and Gasloos trailing arms are presented. This is followed by SEM micrographs for the purpose of characterising carbide precipitation. Next, both the measured residual stress depth profiles and the depth profiles corrected for the effect by the EDM process are covered. Lastly, more SEM micrographs are shown to detail the difference in the morphology in the microstructure near the surface, as well as some measurements of the composition in this region of the microstructure. From all the experimental data and imagery acquired during this study, only the most relevant material is covered in this chapter. The full set of data and images are included in the Appendices.

5.1. Fracture Analysis

The second most striking difference between the two trailing arms, second only after the incredible difference in fatigue life, is the difference between the fracture surfaces, which can be seen in figure 5.1. Where the fracture surface of the Gasloos trailing arm (figure 5.1b) is essentially a very standard fracture for this type of steel, the fracture surface of the Reference trailing arm (figure 5.1a) has two distinct regions on its fracture surface, quantified in table 5.1. Although both fracture surfaces seem to have a point initiation on the upper left, the reference fracture surface also seems to have multiple initiations on the upper right. Around these initiations, there is a distinct intergranular fracture region in the Reference fracture surface, whereas there is no visible difference in the fracture surface around the initiation of the Gasloos trailing arm. In the next two sections, these features are covered in more detail.

	Intergranular	Transgranular
Reference	16%	84%
Gasloos	<0.1%	>99.9%

Table 5.1: Percentage of area per fracture mode

(a) Reference **(b)** Gasloos

Figure 5.1: Overview of the fracture surfaces of the reference and gasloos trailing arms

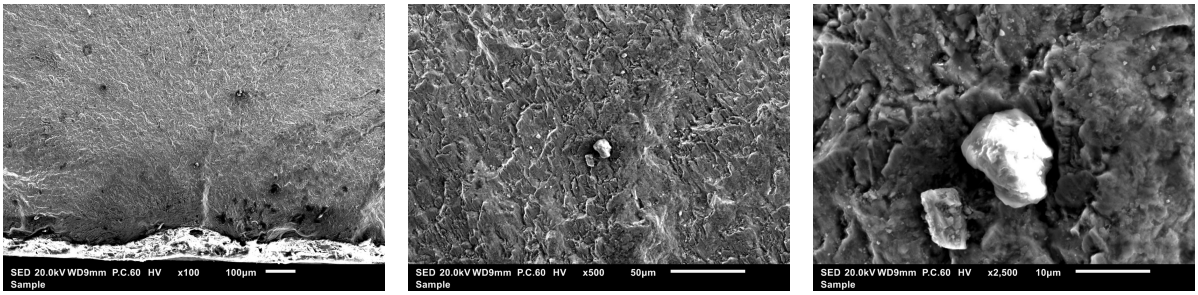

(a) (b) (c)

Figure 5.2: SEM images of the point initiation on the fracture surface of the reference trailing arm. More images in appendix A, figure A.1

C	O	Al	Si	Fe
8.10%	53.16%	0.4%	33.47%	4.87%

Table 5.2: Composition of the slag inclusion at the initiation point of the Reference fracture surface in weight%.

5.1.1. Reference Fracture Surface

Probably the most interesting of the two fracture surfaces is the one from the trailing arm produced using the Reference heat treatment approach, which included the dedicated recrystalisation and austenisation steps. It has a couple of significant details that will be covered in more detail, namely:

- A single point initiation near the upper left corner
- Multiple initiations on a horizontal line (line initiation) near the upper right corner
- An intergranular brittle fracture region around these initiations
- A transition from intergranular (brittle) fracture to (slightly more ductile) transgranular fracture
- A transgranular region of final fracture

Point initiation

At the point where faint lines converge in the area of the point intitiation, an inclusion of around $10\mu m$ is found at around $300\mu m$ from the surface. This is shown in figure 5.2, although it should be noted that these images are taken upside down compared to the overview seen in figure 5.1. Using EDS analysis, it was determined that the particle consists mostly of silicon and oxide as can be seen in table 5.2, possibly in the form of silicon oxide. It is very likely that this particle is a slag inclusion, a by-product of the steelmaking process. These inclusions of slag are found all over the fracture surface, although this particular inclusion seems likely to be the initiation point of this part of the fracture due to its location at the mentioned convergence of distinct lines in the fracture surface. Also clearly visible in figure 5.2b and figure 5.2c is the intergranular fracture mode around this initiation point.

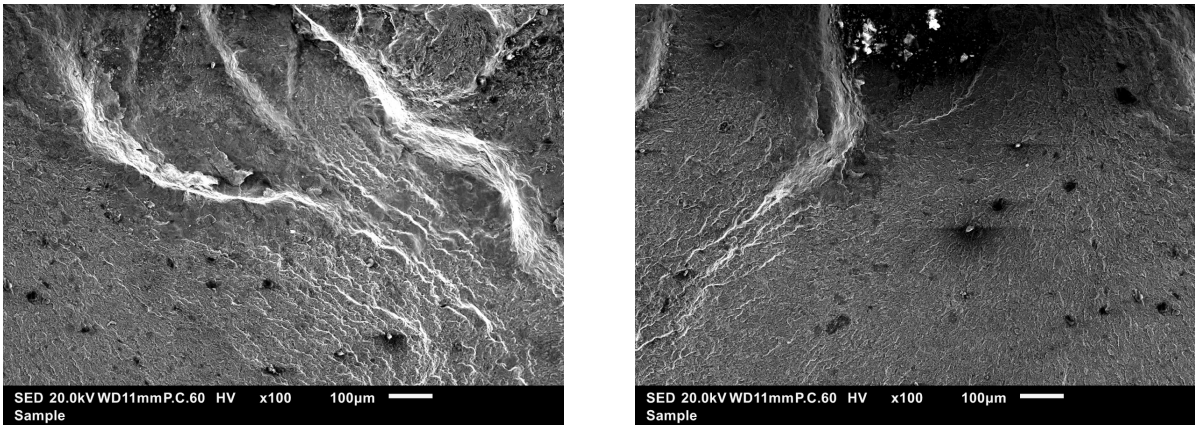

(a) (b)

Figure 5.3: SEM images of the line initiations on the fracture surface of the reference trailing arm. More images in appendix A, figure A.2

Line initiation

Near the upper right corner, another region of intergranular fracture is found, pictured in figure 5.3 in the same orientation as the overview in figure 5.1. In this region, it appears that the fracture originated from multiple points along the upper surface, which at some point merged into a single fracture, forming distinct ridges on the surface of the fracture. Although the fracture surface in this area is also riddled with slag inclusions, there are no clear candidates that could be initiation points. It is obvious that there was a clear preference for the fracture to develop around these inclusions. Note also the black spots, which are holes where slag inclusions could have been positioned before but are still on the other side of the fracture or were washed off during ultrasonic cleaning of the fracture surfaces. In the end, the abundance of these inclusions on this fracture surface does lend itself well to characterisation of the size of these inclusions, which can be seen in table 5.3.

Mean size	Standard deviation
16.09 μm	9.25 μm

Table 5.3: Size distribution of slag inclusions in the Reference trailing arm

Intergranular brittle fracture region

Zooming in on one of these potential former sites of a slag inclusion in figure 5.3, it is clear that in this area of line initiation, the fracture mode is also intergranular.

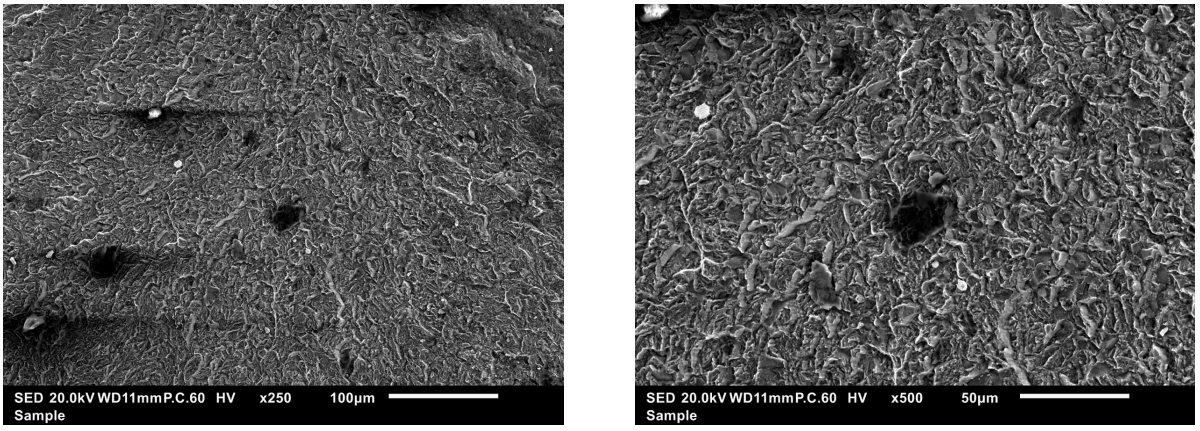

(a) (b)

Figure 5.4: SEM images of intergranular fracture region on the fracture surface of the reference trailing arm. More images in appendix A, figure A.3

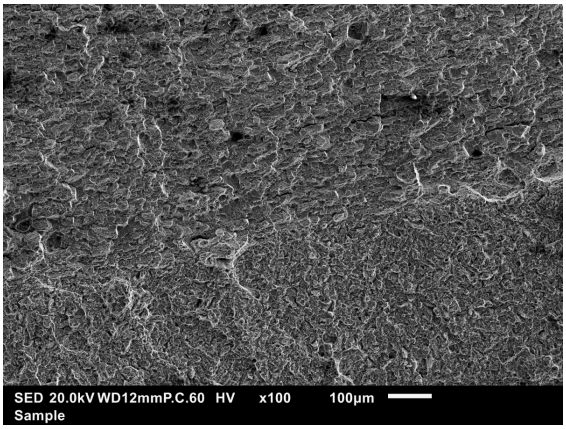

(a)

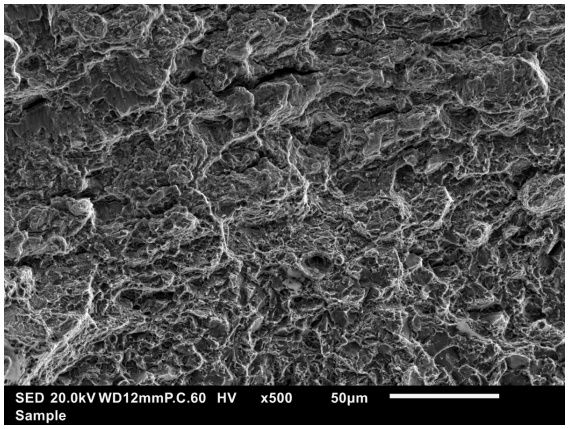

(b)

Figure 5.5: SEM images of the transition of fracture mode on the fracture surface of the reference trailing arm. More images in appendix A, figure A.4

Intergranular fracture to transgranular fracture transition

Moving further down the fracture surface, at a certain point a visible transition to a different fracture mode is observed, as shown in figure 5.5. From this point on, the fracture looks slightly more ductile and no longer systematically follows the grain boundary. However, it remains a relativly brittle fracture, looking like a brittle cleavage fracture, which is to be expected for this type of steel.

Final Fracture

In figure 5.6 this mode of cleavage fracture is clearly visible in what looks like the area of final fracture. Note also again the inclusion visible in figure 5.6a, which can still be found in this area of the fracture, although not as numerous or systematic as in the areas of intergranular fracture.

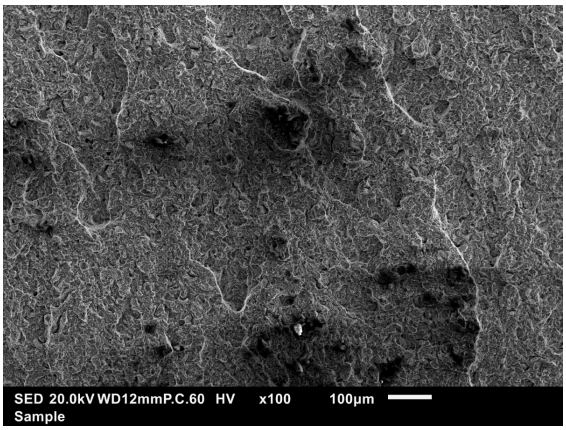

(a)

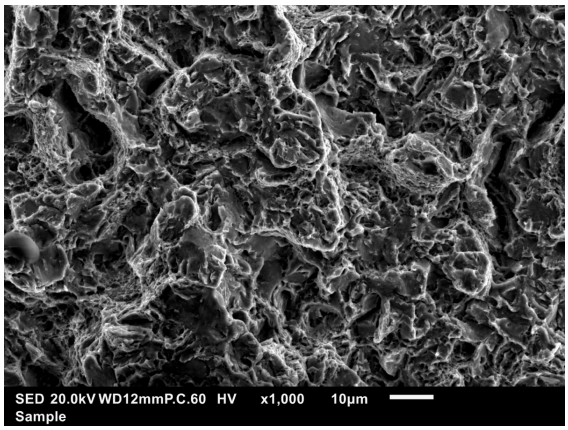

(b)

Figure 5.6: SEM images of the final fracture on the fracture surface of the reference trailing arm. More images in appendix A, figure A.5

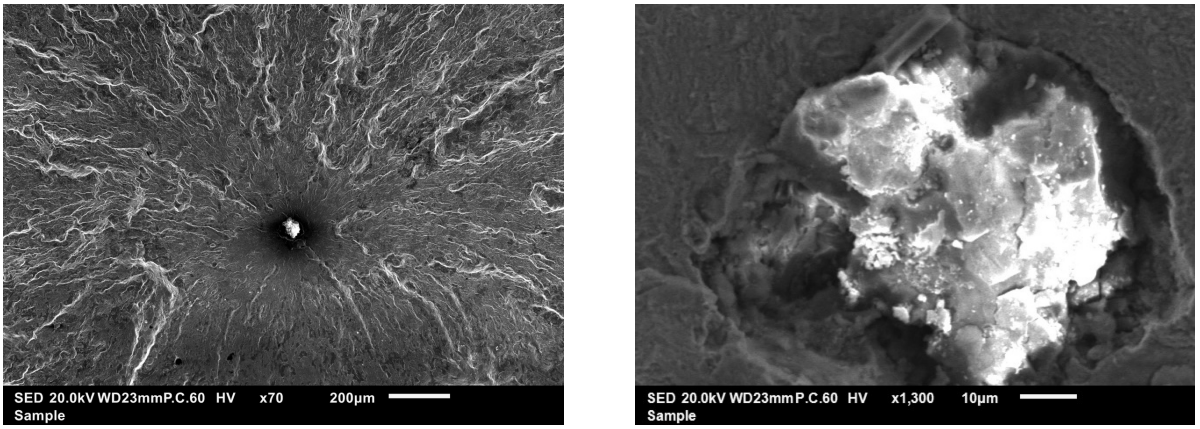

(a) (b)

Figure 5.7: SEM images of the point initiation on the fracture surface of the gasloos trailing arm. More images in appendix A, figure A.6

5.1.2. Gasloos Fracture Surface

Point initiation

At the centre of the point initiation, clearly visible in figure 5.7, is also an inclusion. EDS analysis, shown in table 5.4, also shows that it is likely a slag inclusion. Important to note is also the size of around $45\mu m$, which is around 4.5 times larger than the inclusion at the centre of the point initiation on the Reference fracture surface. It is also found much farther from the surface, around $550\mu m$. Around the initiation, there appears to have occurred a rather violent cleavage fracture.

C	O	Na	Mg	Al	Si	K	Ca	Fe
11.11%	43.13%	3.30%	5.46%	27.07%	5.48%	2.08%	6.9%	12.37%

Table 5.4: Composition of the slag inclusion at the initiation point of the Gasloos fracture surface in weight%.

Final fracture

Looking at an area of the large final fracture in figure 5.8, taken near the upper right corner looking at the overview in figure 5.1b, it becomes clear that this entire fracture seems to be of the type of cleavage fracture. Note, from figure 5.8b that this does not mean that intergranular fracture never happens. There may be local regions, where the orientation of grain boundaries is favourable, for example, where the fracture propagation along the grain boundary is still favoured over transgranular fracture.

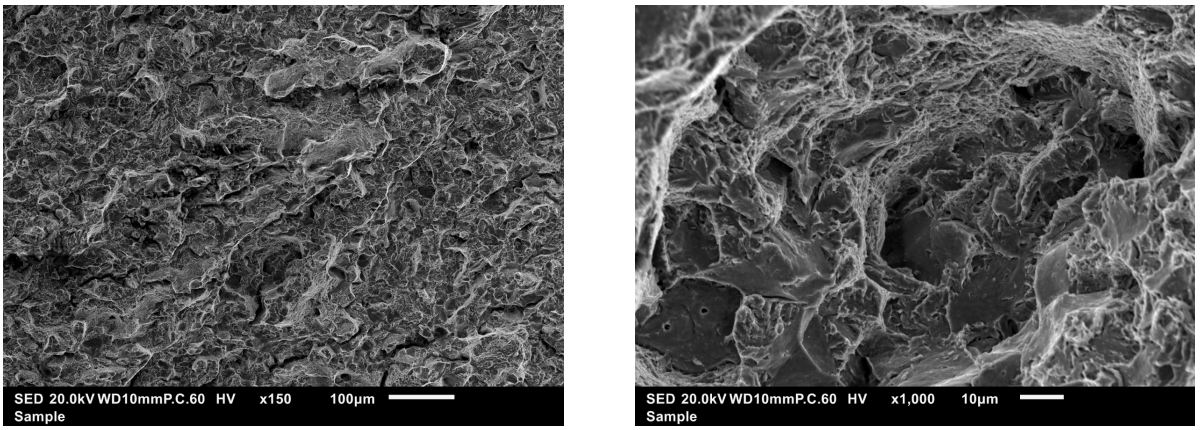

(a) (b)

Figure 5.8: SEM images of the final fracture on the fracture surface of the gasloos trailing arm. More images in appendix A, figure A.7

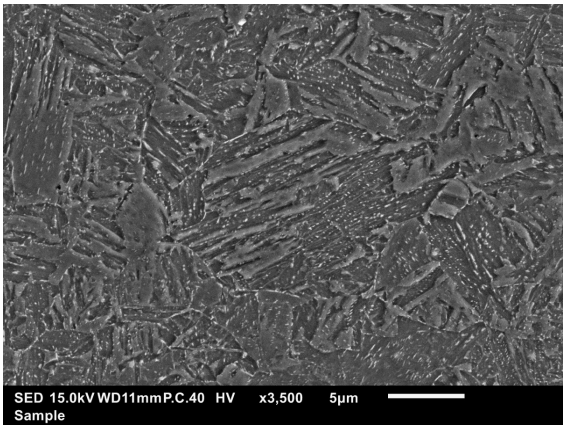

(a)

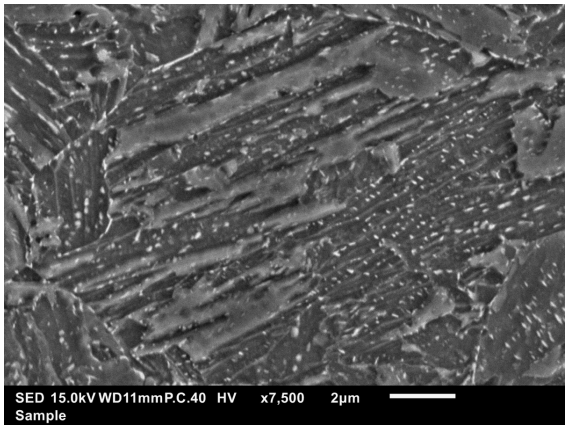

(b)

Figure 5.9: SEM images of the microstructure from the Reference trailing arm. More images in appendix A, figure A.8

5.2. Carbide precipitates

As mentioned in section 3.3, segregating solutes to the prior austenite grain boundary have the potential of causing heterogeneous carbide precipitation on that grain boundary, which can significantly embrittle it. In this section, micrographs from the Reference and Gasloos microstructure made using SEM will be presented to quantify the difference in carbide precipitation levels and location.

5.2.1. Reference Microstructure

Looking at the micrographs of the Reference microstructure in figure 5.9, the prior austenite grain boundary is clearly visible due to the high amount of heterogeneous carbide precipitation there, the density of which is shown in table 5.6. EDS analysis of these carbides, shown in table 5.5, shows that these carbides must be cementite. Note that there is also homogeneous carbide precipitation within the prior austenite grains, with overall carbide density shown in table 5.7. The average measured width of martensite laths is shown in table 5.8.

Fe	C
85.32%	14.68%

Table 5.5: Average composition of the carbides on the prior austenite grain boundary in Reference

Carbides on PAGB (#)	Length of PAGB measured (μm)	Carbide density on PAGB (μm^{-1})
139	70.6	1.97

Table 5.6: Carbide density on the prior austenite grain boundary in Reference

Carbides in measured area (#)	Measured area (μm^2)	Carbide density (μm^{-2})
5500	910.54	6.04

Table 5.7: Overall carbide density in microstructure of Reference

Average width (μm)	Standard deviation (μm)
0.61	0.26

Table 5.8: Average width of martensite laths in Reference

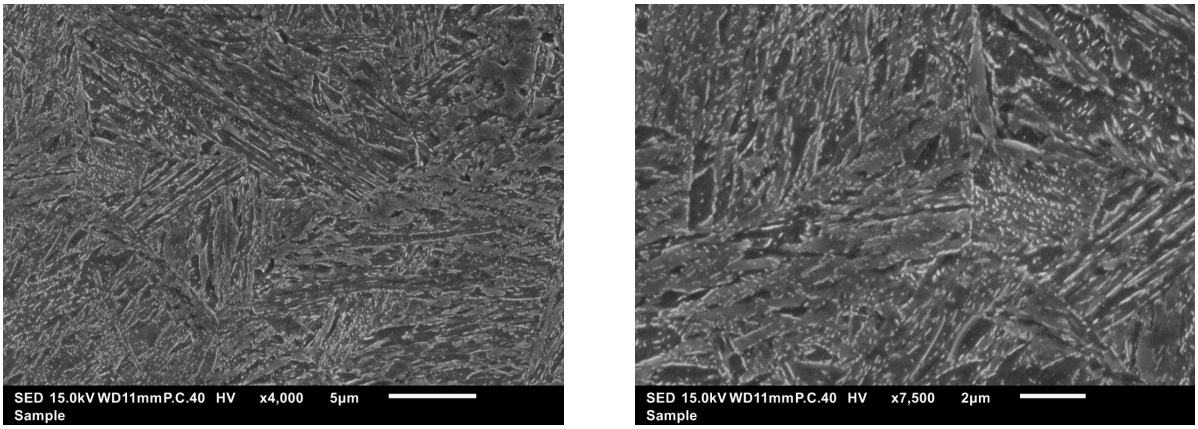

(a) (b)

Figure 5.10: SEM images of the microstructure from the Gasloos trailing arm. More images in appendix A, figure A.9

5.2.2. Gasloos Microstructure

The Gasloos microstructure is very different, as can be seen in figure 5.10. Here, the prior austenite grain boundary is difficult to identify, as there is significantly less heterogeneous carbide precipitation on it as can be seen from table 5.10. However, there is much more homogeneous carbide precipitation within the prior austenite grains, which can be seen in table 5.11. The composition of these carbides is shown in table 5.9, which interestingly shows that they contain manganese. The average measured width of martensite laths is shown in table 5.12.

Fe	C	Mn
92.60%	6.10%	1.30%

Table 5.9: Average composition of the carbides on the prior austenite grain boundary in Gasloos

Carbides on PAGB (#)	Length of PAGB measured (μm)	Carbide density on PAGB (μm^{-1})
97	101	0.96

Table 5.10: Carbide density on the prior austenite grain boundary in Gasloos

Carbides in measured area (#)	Measured area (μm^2)	Carbide density (μm^{-2})
4616	696.96	6.62

Table 5.11: Overall carbide density in microstructure of Gasloos

Average width (μm)	Standard deviation (μm)
0.417	0.108

Table 5.12: Average width of martensite laths in Gasloos

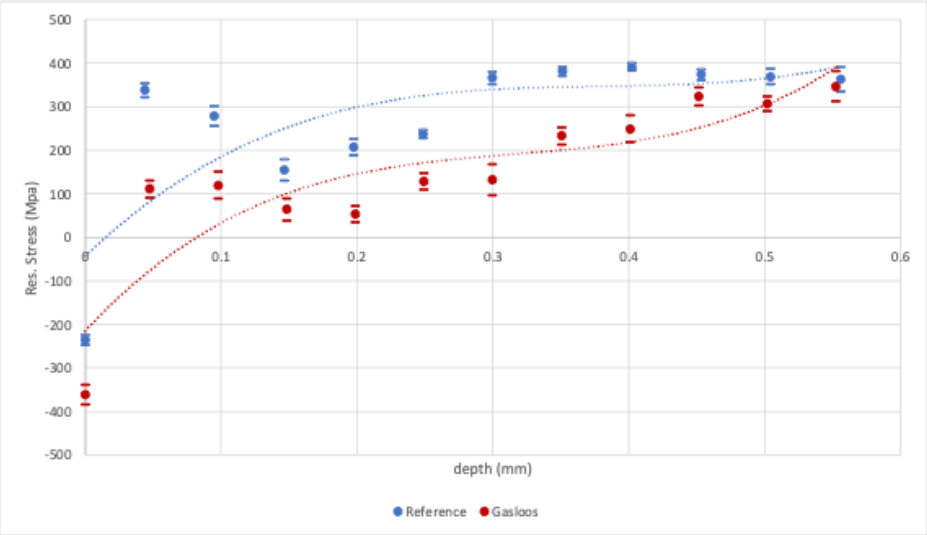

Figure 5.11: Depth profile of residual stress in Reference and Gasloos trailing arms, raw measurement

5.3. Residual stress depth profiles

5.3.1. Measured

The raw measurements are plotted in figure 5.11. This includes the surface measurements at $x = 0$, which was taken before cutting the sample using EDM, and the rest of the measurements done on the slope that was cut using EDM. It is clear from this that the EDM induced a residual tensile stress, although the profile itself has the distinct shape that was expected for this measurement [37], with the exception of the $x \approx 0.05mm$ and $x \approx 0.1mm$ data points of the Reference measurement. Because of the fact that the induced residual tensile stress from the EDM process is homogeneous [38], a correction can be estimated by extrapolating towards $x = 0$, and calculating the difference between this extrapolated value for $x = 0$ and the known surface measurement at $x = 0$. This leads to a calculated correction of $482MPa$.

5.3.2. Corrected for EDM

The measured data with the correction applied can be seen in figure 5.12. From this, it is clear that the residual compressive stress in Gasloos is not only significantly higher, but that the effect is also significantly deeper than in Reference.

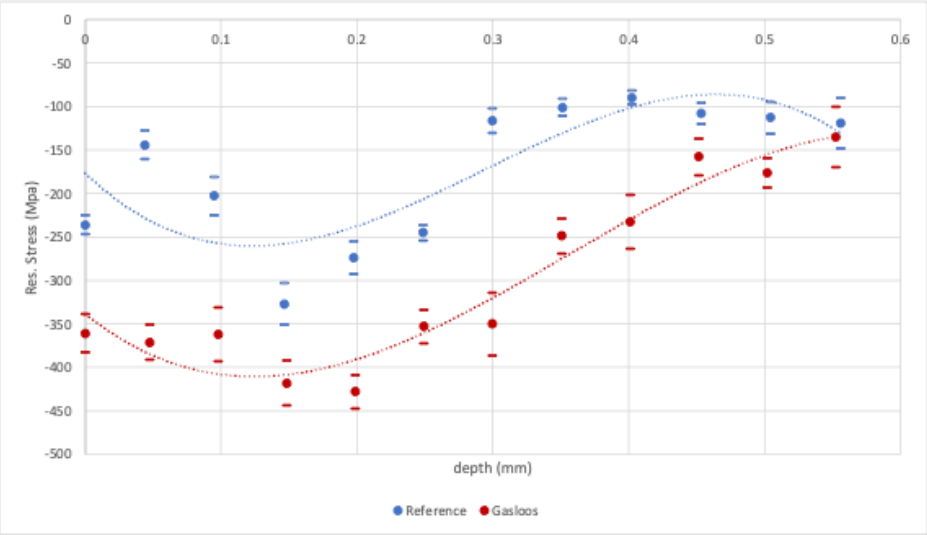

Figure 5.12: Depth profile of residual stress in Reference and Gasloos trailing arms, data corrected for influence of EDM

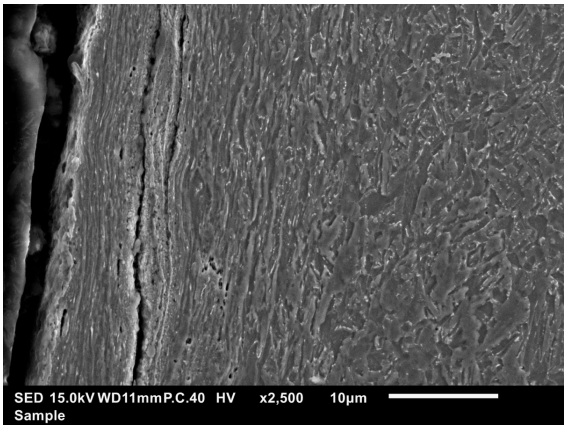

(a) Reference

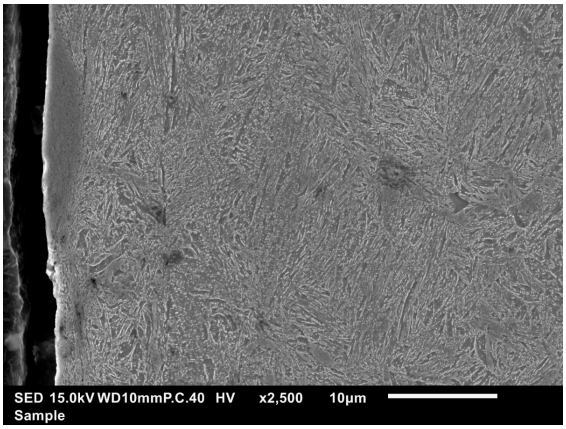

(b) Gasloos

Figure 5.13: SEM images of the microstructure near the surface of the Reference and Gasloos trailing arm

5.4. Morphology near the surface

To better characterise the difference in surface quality that affects the effectiveness of the shot peening treatment, micrographs of the microstructure near the surface, as well as measurements of the composition near the surface are presented.

5.4.1. Microstructure near the surface

The microstructure near the surface in the trailing arms of Reference and Gasloos is shown in figure 5.13. In figure 5.13a the scales are clearly visible in the Reference microstructure, along with many large and small voids in between. This morphology is clearly lacking in figure 5.13b showing the Gasloos microstructure.

5.4.2. Composition near the surface

EDS analysis near the surface, visible in table 5.13, shows an elevated oxygen content in the Reference sample at the edges of the scales, including the internal edges in large voids. Similar analysis in the Gasloos sample shows only a slightly elevated oxygen content at the very edge.

O	Fe
17.49%	82.51%

(a) Edges of scales in Reference

O	Fe
2.47%	97.53%

(b) Surface edge of Gasloos

Table 5.13: Average oxygen content at the surface of the trailing arms in weight%

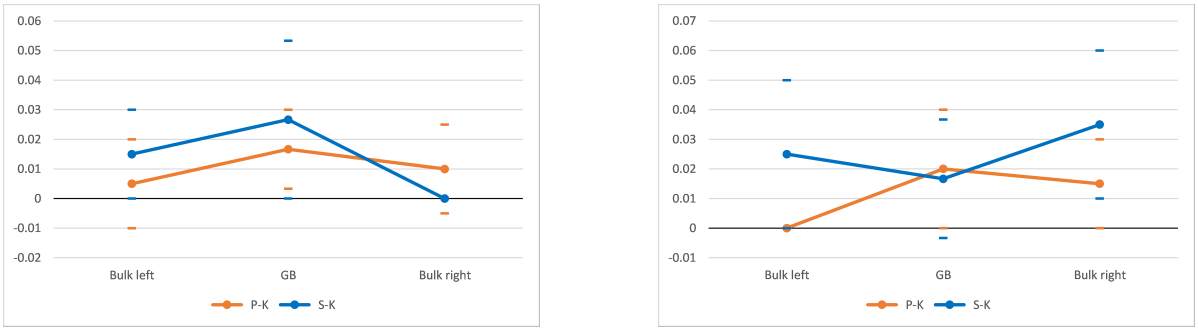

(a) Reference

(b) Gasloos

Figure 5.14: EDS measurements of grain boundary segregation of phosphorus and sulphur. Also detected but not plotted (in order from highest to lowest average weight%): Iron, Chromium, Manganese, Carbon, Silicon, Vanadium

5.5. Segregation of Solutes to the Grain Boundary

Grain boundary segregation of sulphur and phosphorus was measured using EDS by doing measurements on the prior austenite grain boundary and comparing this with measurements in the bulk left and right of this prior austenite grain boundary. This proved unsuccessful, with almost all measured values being within standard deviation of zero. Sulphur and phosphorus measurements are shown in figure 5.14. After this disappointing result, the further measurement of grain boundary segregation by EDS was abandoned.

6

Discussion on Results

6.1. Fracture Behaviour

Interestingly the fracture in both trailing arms appears to initiate on the slag inclusions, which are not affected by the heat treatment since they are present from the steel making process. However, the notable difference is the size, with the inclusion at the initiation point in Gasloos being about 4.5 times larger than that in Reference. This means that a significantly higher stress concentration was necessary to initiate the fracture in Gasloos [40], which means that the microstructure in Gasloos is likely much stronger. It should also be noted that the slag inclusion that nucleated the final fracture in Gasloos is more three standard deviations larger the average size of slag inclusions found in the material, while the slag inclusion found in the point initiation in Reference is below average, but within the standard deviation. Regarding the size distribution measured for the slag inclusions, it is important to acknowledge that this was only measured on the fracture surface of Reference, since this revealed many slag inclusions. However, since these are slag inclusions that are present from the steelmaking process, are unaffected by heat treatments, and the two trailing arms are made from the same batch of steel, this measured size distribution should be representative for both trailing arms.

With the fractures in Reference developing intergranularly from smaller inclusions, this could mean that the fatigue limit in the Reference microstructure is significantly reduced due to an embrittled grain boundary, allowing a crack to propagate along the weakened grain boundary, which would not have been able to propagate through the interior of the grain, since this is significantly stronger. Since the grain boundary is not embrittled in the Gasloos microstructure, such fatigue cracks are not able to propagate. Instead, when these cracks nucleate they likely stay contained around these slag inclusions or other microstructural features that cause stress concentrations. The build-up of these microscopic cracks throughout the microstructure also work to weaken the trailing arm as a whole, eventually leading to failure, although much later.

6.2. Solute Segregation to the Grain Boundary

Although a disappointing result, it was not unexpected that EDS would not be able to measure the potential segregation of elements to the grain boundary. However, this does not lead to the hypothesis being disproven. In the following sections, the possibility for equilibrium and non-equilibrium will be discussed based on the literature presented in chapter 2, followed by the possible effects that elements present in 51CrV4 can have if segregated to the grain boundary based on the literature presented in chapter 3.

6.2.1. Equilibrium Segregation

In general the equilibrium grain boundary concentration for a certain element increases with decreasing temperatures. However, it must be noted that this equates to an inverse relationship with mobility, which decreases with lowering temperatures. This leads to the lower limit of 650° K (377° C) [1], under which the equilibrium grain boundary segregation is practically never reached because of the low mobility of solutes. The upper limit of segregation, where mobility is certainly high enough, but equilibrium

concentration is too low to create a significant driving force, is harder to define. Clark et al. [41] was one of the few studies that focused on the influence of austenisation temperature on segregation effects and showed that above 1100° C, plain strain fracture toughness of untempered samples doubled.

Although the equilibrium of segregation is mainly influenced by temperature, the characteristic of this dependence is altered by the interaction between segregated solutes, as described in section 2.2. Namely, it should be noted that...

- ...site competition can lead to the suppression of certain less segregating solutes at the grain boundary when temperature is lowered, and these are replaced by other more readily segregating solutes that compete for the same grain boundary lattice site.
- ...repulsive interaction increases the segregation of a more readily segregating solute at the cost of a less readily segregating solute being even more suppressed, while attractive interaction can severely increase the level of segregation for a less readily segregating solute at the cost of the more readily segregating solutes segregating less. In the latter case, this leads to cases in which certain solutes are dragged along during segregation at levels that may seem unfathomable through regular diffusion [1].

To conclude, the temperature of the austenisation oven used in the Reference heat treatment approach definitely falls within the critical temperature window where there is sufficient mobility for diffusion to occur, and simultaneously sufficient driving force due to the high enough equilibrium grain boundary concentration. However, it is difficult to say whether the oven time is long enough for sufficient equilibrium segregation to occur on its own to embrittle the grain boundary.

6.2.2. Non-Equilibrium Segregation

The two mechanisms of non-equilibrium segregation that were discussed in section 2.3 were the only ones discussed out of many other possible mechanisms, since these two are the only ones which have the probability of occurring in the trailing arms during production. The first mechanism, thermally induced grain boundary segregation discussed in section 2.3.1, definitely seems relevant for the present study if it were not for two counterarguments:

- Even without calculation of the critical time (equation (2.7)) it can be concluded that the tempering time of one hour will erase any and all non-equilibrium segregation effects by the end of the tempering treatment.
- Between the two production methods, nothing changes in the tempering treatment. Thus, any difference in grain boundary segregation levels after heat treatment cannot be a direct effect of the tempering treatment.

The other effect of non-equilibrium grain boundary segregation due to grain boundary migration, as described in section 2.3.2, seems to have a reasonable possisibilty of occuring in the Reference heat treatment approach based on literature. Slow cooling below the Ae3 temperature causing recrystallisation followed by re-austenisation, as is done in the Reference heat treatment approach, is the perfect condition for this type of segregation to occur, as was shown by several studies. Great examples are:

- Zhang [12] showed that the boron segregation intensifies with continued recrystallisation.
- Briant and Banerji [20] showed that maraging steels cooled slowly through the 1000 C - 750 C range would become significantly embrittled.
- Horn and Ritchie [18] investigated two grades of stainless steel (300-M and 4340) and showed that air cooling these from the austenisation temperature of 870 C leads to a sharp decrease in impact strength and an intergranular fracture.
- Ohtani and McMahon [16] showed that even for very slow step cooling from below austenisation temperature, this slow cooling leads to grain boundary embrittlement.

There are many more studies that allude to this embrittlement by slow cooling rates from elevated temperatures; however, there remains the issue of the oven treatment after this cooling and recrystallisation phase of the reference heat treatment of the trailing arms in question and if this erases the previous segregation effects. The study by Maier and Faulkner [42] points to the fact that the final levels of segregation may very well be the product of the history of the material. When they investigated the weld chemistry in steel containing manganese and phosphorus, they showed that the final

segregation was the aggregate of all the preceding steps. Considering this, together with the fact that after recrystallisation the sample never gets heated to sufficient temperatures where the driving force for grain boundary segregation becomes significantly low, it seems likely that if segregation were to occur during the recrystallisation phase, this can persist throughout the rest of the heat treatment.

In the end, it is possible that non-equilibrium segregation aids in increasing the grain boundary concentration of certain elements in the Reference heat treatment approach, especially if the time in the austenisation oven on its own is not enough to reach sufficient levels of segregation.

6.2.3. Embrittling Elements present in 51CrV4

Figure 3.2 provides an intuitive overview of the embrittling potential for any matrix material. In this case, the enthalpy of sublimation for iron is represented by a dashed line, with elements below the line decreasing the grain boundary cohesion and elements above the line enhancing it. From this figure, the embrittling potential of the elements in 51CrV4 can be derived.

Carbon

The one element that distinguishes steel from pure iron is, of course, carbon. Figure 3.2 gives one reason why carbon is so important in steel, showing that carbon significantly enhances the grain boundary cohesion in steel when it is present at the grain boundary. The flip side to this is that a lack of carbon at the grain boundary will decrease the grain boundary cohesion, which could be part of the explanation for why edge decarburisation in steel leads to a lower fatigue life. The decrease of carbon near the surface locally decreases the grain boundary cohesion, potentially making it easier for small surface imperfections or other stress concentrations near the surface to nucleate and propagate intergranular fatigue cracks, or otherwise provide a smaller barrier to arrest transgranular fatigue cracks.

Alloying Elements

Apart from vanadium giving a slight increase in grain boundary cohesion, the other alloying elements in 51CrV4 actually negatively influence grain boundary cohesion in this alloy. When considering the alloying elements, the important conclusions are that...

- ...chromium, which is the most abundant alloying element, slightly decreases grain boundary cohesion, but the relative potency to iron is fairly low.
- ...vanadium is slightly more potent and actually increases the grain boundary cohesion, but its bulk concentration is the lowest of all alloying elements.
- ...manganese has by far the highest potency and decreases grain boundary cohesion in iron, while it is only slightly less abundant than chromium.

This last conclusion is beautifully supported by Liu et al. [34], where a steel alloy with almost 10% manganese is used to make Mn-enriched grain boundaries, which lowers the strength of the grain boundary compared to the interior of the grain. Through atom-probe tomography, the authors show that there is segregation of manganese and carbon to the grain boundary. Although carbon is more potent in increasing grain boundary cohesion than manganese is in decreasing grain boundary cohesion, the concentration of manganese at the grain boundary is about five times higher than that of carbon, significantly overpowering the carbon and making for a relatively weak grain boundary in this example. The most interesting thing is that this is used by Liu et al. [34] to make an ultra-strong steel, instead of it being a negative factor.

Impurities

With only three elements (four if you count carbon) intentionally present in the iron matrix of 51CrV4 and thus there as alloying elements, this leaves the rest of the periodic table to be theoretically branded as potential impurities. To keep this section concise, only a handfull of likely suspects will be considered. These include antimony, tin, sulphur, phosphorous, and silicon. These are all elements from groups 14-16 of the periodic table and are recognised as common grain boundary embrittlers in steel [20]. This is confirmed by observing their relative postition to iron in figure 3.2. It is interesting to observe however, that even though carbon and nitrogen are also in group 14 and 15 respectively (and for that matter boron in group 13), they are grain boundary enhancers. This alludes to further complexity of grain boundary cohesion that stays hidden behind equation (3.4). Several studies [43, 44] have been done involving ab initio calculations of chemical bonding of clusters of iron with antimony, sulphur, boron,

and carbon, representing the same atomic structures that are found on the grain boundary, revealing a redistribution of electron charge density in the grain boundary.

6.3. Carbide Precipitation

The results shown in section 5.2 clearly show the apparent heterogeneous precipitation of cementite in the Reference microstructure. Reference has a prior austenite grain boundary carbide density that is more than twice as high as the Gasloos microstructure, while the overall carbide density is higher in Gasloos. Due to this higher overall density in Gasloos, it is likely that this also inflates the PAGB carbide density in Gasloos since this means there are more homogeneously precipitated carbides that precipitated on the PAGB just by random chance. As mentioned in section 3.3.1 and section 3.3.2, a multitude of studies have confirmed the role of retained austenite in the subsequent formation of cementite on the prior austenite grain boundary. Only the study by Horn [18] alludes to the fact that this stabilised austenite itself is also a product of grain boundary segregation, but does not provide conclusive evidence. However, the theory remains grounded in the fact that certain elements in 51CrV4, namely carbon and manganese, are widely known as austenite stabilising elements. Since only carbon was detected in the carbides on the prior austenite grain boundary in Reference, it may be unlikely that manganese can segregate in sufficient quantities, and it may be that segregation of carbon alone is enough to stabilise a fine film of austenite during quenching. However, this measurement on its own is not enough evidence to conclusively prove this.

It should also be noted that the slightly larger density of carbide precipitates in Gasloos is likely a positive aspect in the context of fatigue, since this causes precipitation hardening in the steel, and higher hardness is desired for better fatigue behaviour.

6.4. Effectiveness of Shot-Peening

From the measurements presented in section 5.3 it is clear that the shot-peening treatment is much more effective in the Gasloos trailing arm than in the Reference trailing arm, with a peak residual compressive stress about 1.5 times higher and the effect reaching almost twice as deep. However, it remains difficult to accurately quantify this difference in residual stress, since the final measurements are calculated with estimated parameters for the Young's modulus and Poisson ratio, and a correction had to be applied for the effect of the EDM procedure that was found through extrapolation towards a known surface measurement. Although this method of measurement is much less time- and labour-intensive than the traditional method of incremental removal of material by electropolishing between XRD measurements, work still needs to be done to further improve this measurement procedure and remove the effect of the EDM process in the measured value for the residual stress.

Notable are also the potential outliers in Reference at $x \approx 0.05mm$ and $x \approx 0.1mm$. It is difficult to conclude whether these deviations are due to mistakes made in sample preparation, particularly during the sand-blasting procedure that was used to remove the expoy-ester coating from the reference trailing arm, or that the measurements are in fact accurate, and the deviation comes from other effects in the Reference microstructure in this location.

Comparing these results with the observation made in the fracture analysis, it is interesting to note that the depth of the initiation points match perfectly with the depth where the effect of the residual compressive stress drops off in both trailing arms, showing that in areas where there is significant residual compressive stress, initiation of cracks is effectively mitigated. The fact that this effect is much deeper for Gasloos means that a larger region with high stress is negated by this effect, since the bending stresses are highest near the surface.

6.5. Oxide scales on the surface

Looking at the surface morphology and composition of the two trailing arms, it is clear that the outer layer consisting of oxide scales on the Reference trailing arms are to blame for the lesser effectiveness of the shot-peening treatment. Almost certainly, much of the energy from the shot is absorbed through the compression of the loosely stacked oxide scales. Combined with the fact that this oxide is also much less ductile than steel, this leads to a very ineffective transfer of strain into the steel below, leading to a lower peak residual compressive stress as well as a much shallower effect in the material. The Gasloos trailing arm has a more ductile steel surface, which is much more able to deform from the impact of the shot and transfer that strain into the material in this process, leading to an effective shot-peening treatment.

However, it is not clear what happens exactly with the oxide scales in the austenisation oven that makes it stick to the Reference trailing arm, and not get washed of during the subsequent quenching like what happens for the Gasloos trailing arm. It is possible that the low integrity of the protective gas in the furnace allows for further oxidation of both the scales and the surface of the trailing arms, which leads to the oxide scales essentially growing to the surface.

6.6. Increase in Fatigue Life

Considering all results discussed in previous sections, it seems likely that the embrittlement of the grain boundary in the reference trailing arm allows cracks nucleated on the slag inclusions to grow and propagate along the prior austenite grain boundary with each cycle in the fatigue test. This is not possible in the unembrittled Gasloos trailing arms, where cracks nucleated on slag inclusions do not have this easy path for growth and will thus hardly grow relative to cracks in Reference with each cycle. This relatively easy propagation of cracks in the Reference trailing arm progressively weakens it with each cycle, leading to early failure of the trailing arm. On the other hand, since cracks can hardly grow in the Gasloos trailing arm, it will take much longer for the progressive build-up of more and more microscopic cracks in the material to eventually also weaken the trailing arm enough to the point where it will fail.

7

Conclusions

- The Reference grain boundary is much weaker compared to that of Gasloos. This is apparent from the partially intergranular fracture observed on 16% of the Reference fracture surface area. (section 5.1)
- The intergranular fracture surface of Reference is riddled with slag inclusions, with an average size of 16.09μm. Since these slag inclusions should not be an effect of or affected by the different heat treatment approaches used, and both trailing arms are made from the same batch of steel, this quantity should be representative for both. (section 5.1)
- Cracks nucleate on slag inclusions in both trailing arms, although the inclusion that caused the final fracture is 4.5 times larger in Gasloos at 45μm, while the inclusion in the point initiation in Reference is only 10μm. (section 5.1)
- This weakening of the grain boundary is in part due to heterogeneous precipitation of carbides on the prior austenite grain boundary, which is more than twice as high in density in Reference. (section 5.2)
- On the contrary, the overall density of carbides in the microstructure is 10% higher in Gasloos. (section 5.2)
- The segregation of the embrittling elements to the prior austenite grain boundary could not be accurately measured using energy dispersive X-ray spectroscopy. (section 5.5)
- The outer surface of the Reference trailing arm is made up of a thin layer of oxide scales containing on average 17.49 weight% of oxygen. These are left there from the hot-forming process. This results in a very brittle surface, with lots of voids in between the oxide scales. The Gasloos trailing arm does not have this. (section 5.4)
- The effect of the shot-peening treatment is much less effective in the Reference trailing arm, inducing lower residual compressive stresses in the material and having a shallower effect. This is likely due to the layer of oxide scales with voids on the surface. The Gasloos trailing arm does not have this outer oxide layer, resulting in a peak residual compressive stress about 1.5 times higher and the effect reaching almost twice as deep. (section 5.3)

8

Recommendations

- More research with better-suited equipment is needed to confirm or deny the occurrence grain boundary segregation in these trailing arms. Studies [14] have shown that certain etchants could be used to reveal grain boundary embrittlement, this could be explored as an alternative.
- This study only analysed one trailing arm per heat treatment approach, so more trailing arms should be studied to enhance the statistical validity of the findings of this study.
- Although the measurement of the residual stress depth profile on a slope cut by EDM is much less time- and labour-intensive compared to the traditional method that uses consecutive measurements between material removal using electropolishing, this new method produces distorted measurements because of the induced residual tensile stress from the EDM process itself. Further development of this method is advised to remove this influence in the measurement, perhaps by removing the distorted layer of material using electropolishing.
- Since it may be possible that the removal of the expoy-ester coating using glass-blasting had some effect on the measured residual stress up to a depth of $0.1mm$ in the Reference sample, it is recommended that the trailing arms selected for testing do not receive the expoy-ester coating in the first place.
- Although theories on the matter were discussed, the exact reason behind the adherence of the oxide scales to the trailing arms during the Reference heat treatment approach has not been conclusively determined. The exact mechanism behind this, and more importantly how this can be prevented, should be subject of further inquiry.

References

[1] Pavel Lejček. *Grain Boundary Segregation in Metals*. Vol. 136. Springer Series in Materials Science. Berlin, Heidelberg: Springer Berlin Heidelberg, 2010. ISBN: 978-3-642-12504-1. DOI: 10.1007/978-3-642-12505-8. URL: https://link.springer.com/10.1007/978-3-642-12505-8.

[2] S Hofmann. "Segregation at Grain Boundaries". In: *Surface Segregation Phenomena*. Ed. by Peter A Dowben and Allen Miller. Boca Raton: CRC Press, 1990. Chap. Chapter 4, pp. 107–134. ISBN: 0849368936. URL: https://books.google.nl/books?hl=en&lr=&id=cQag_EFxt-wC&oi=fnd&pg=PA107&dq=S.+Hofmann+Segregation+at+grain+boundaries,&ots=bebU5GZxgc&sig=FQkUaz9FwsltBICedlOWv79Wsh0&redir_esc=y#v=onepage&q=S.%20Hofmann%20Segregation%20at%20grain%20boundaries%2C&f=false.

[3] Josiah Willard Gibbs. "On the Equilibrium of Heterogeneous Substances". In: *Transactions of the Connecticut Academy* 3.10 (1878), pp. 343–524.

[4] Donald McLean. *Grain Boundaries in Metals*. Oxford: Clarendon Press, 1957. ISBN: 9780598673435.

[5] E D Hondros and M P Seah. "Segregation to interfaces". In: *International Metals Reviews* 22.1 (Jan. 1977), pp. 262–301. ISSN: 0308-4590. DOI: 10.1179/imtr.1977.22.1.262.

[6] M Guttmann and Donald McLean. "Grain boundary segregation in multicomponent systems". In: *Interfacial Segregation*. Ed. by W.C. Johnson and J.M. Blakely. Metals Park: ASM, 1979, pp. 261–348.

[7] R G Faulkner. "Combined grain boundary equilibrium and non-equilibrium segregation in ferritic/martensitic steels". In: *Acta Metallurgica* 35.12 (Dec. 1987), pp. 2905–2914. ISSN: 0001-6160. DOI: 10.1016/0001-6160(87)90289-6.

[8] Isaac Newton. *The Mathematical Principles of Natural Philosophy*. Ed. by Andrew Motte. 1729. URL: https://en.wikisource.org/wiki/The_Mathematical_Principles_of_Natural_Philosophy_(1729).

[9] G Gottstein and L S Shvindlerman. *Grain boundary migration in metals : thermodynamics, kinetics, applications*. 1st ed. Boca Raton, Fl: CRC Press, June 1999. ISBN: 9780849382222.

[10] Pil Ryung Cha et al. "A phase field model for the solute drag on moving grain boundaries". In: *Acta Materialia* 50.15 (Sept. 2002), pp. 3817–3829. ISSN: 1359-6454. DOI: 10.1016/S1359-6454(02)00187-8.

[11] Sanhong Zhang, Xinlai He, and T Ko. "Non-equilibrium segregation of solutes to grain boundary". In: *Journal of Materials Science* 29.10 (May 1994), pp. 2663–2670. ISSN: 0022-2461. DOI: 10.1007/BF00356815.

[12] Sanhong Zhang, Xinlai He, and T Ko. "Non-equilibrium segregation of solute to grain boundary". In: *Journal of Materials Science* 29.10 (May 1994), pp. 2655–2662. ISSN: 0022-2461. DOI: 10.1007/BF00356814.

[13] M Sarikaya, A K Jhingan, and G Thomas. *Retained Austenite and Tempered Martensite Embrittlement in Medium Carbon Steels*. Tech. rep. 1983, p. 1121.

[14] I Olefjord. "Temper embrittlement". In: *International Metals Reviews* 23.1 (Jan. 1978), pp. 149–163. ISSN: 0308-4590. DOI: 10.1179/imtr.1978.23.1.149.

[15] Pavel Lejček, Mojmír Šob, and Václav Paidar. "Interfacial segregation and grain boundary embrittlement: An overview and critical assessment of experimental data and calculated results". In: *Progress in Materials Science* 87 (June 2017), pp. 83–139. ISSN: 0079-6425. DOI: 10.1016/J.PMATSCI.2016.11.001.

[16] H Ohtani and C J McMahon. "Modes of Fracture in Temper Embrittled Steels". In: *Acta Metalurgica* 23 (1975), pp. 377–386.

[17] Harshad Bhadeshia and Robert Honeycombe. “The Embrittlement and Fracture of Steels”. In: *Steels: Microstructure and Properties*. Butterworth-Heinemann, Jan. 2017, pp. 303–341. ISBN: 978-0-08-100270-4. DOI: 10.1016/B978-0-08-100270-4.00011-1.

[18] R M Horn and Robert O Ritchie. “Mechanisms of tempered martensite embrittlement in low alloy steels”. In: *Metallurgical Transactions A* 9.8 (Aug. 1978), pp. 1039–1053. ISSN: 03602133. DOI: 10.1007/BF02652208/METRICS. URL: https://link-springer-com.tudelft.idm.oclc.org/article/10.1007/BF02652208.

[19] Harshad Bhadeshia and Robert Honeycombe. “Tempering of Martensite”. In: *Steels: Microstructure and Properties*. Butterworth-Heinemann, Jan. 2017, pp. 237–270. ISBN: 978-0-08-100270-4. DOI: 10.1016/B978-0-08-100270-4.00009-3.

[20] C L Briant and S K Banerji. “Intergranular failure in steel: the role of grain-boundary composition”. In: *International Metals Reviews* 23.1 (Jan. 1978), pp. 164–199. ISSN: 0308-4590. DOI: 10.1179/imtr.1978.23.1.164.

[21] S K Banerji, C J McMahon, and H C Feng. “Intergranular Fracture in 4340-Type Steels: Effects of Impurities and Hydrogen”. In: *Metallurgical Transactions A* 9A (1978), pp. 237–247. ISSN: 0360-2133/78/0210-0237500.75/0. DOI: https://doi.org/10.1007/BF02646706.

[22] J P Hirth and J R Rice. “On the thermodynamics of adsorption at interfaces as it influences decohesion”. In: *Metallurgical Transactions A* 11.9 (Sept. 1980), pp. 1501–1511. ISSN: 0360-2133. DOI: 10.1007/BF02654514.

[23] M P Seah. “Adsorption-induced interface decohesion”. In: *Acta Metallurgica* 28.7 (July 1980), pp. 955–962. ISSN: 00016160. DOI: 10.1016/0001-6160(80)90112-1.

[24] R D K Misra. “Grain boundary segregation and fracture resistance of engineering steels”. In: *Surface and Interface Analysis* 31.7 (July 2001), pp. 509–521. ISSN: 0142-2421. DOI: 10.1002/sia.1079.

[25] Harshad Bhadeshia and Robert Honeycombe. “Solutes that Substitute for Iron”. In: *Steels: Microstructure and Properties*. Butterworth-Heinemann, Jan. 2017, pp. 101–134. ISBN: 978-0-08-100270-4. DOI: 10.1016/B978-0-08-100270-4.00004-4.

[26] C L Briant and N Lewis. “Effect of tempering on fracture mode in high–strength, phosphorus–doped Ni-Cr steels”. In: *Materials Science and Technology (United Kingdom)* 2.1 (1986), pp. 34–41. ISSN: 17432847. DOI: 10.1179/mst.1986.2.1.34.

[27] J R Rellick and C J McMahon. “Intergranular Embrittlement of Iron-Carbon Alloys by Impurities”. In: *Metall Trans* 5.11 (Nov. 1974), pp. 2339–2450. ISSN: 0026-086X. DOI: 10.1007/BF02644027/METRICS. URL: https://link.springer.com/article/10.1007/BF02644027.

[28] Eric B Kula and Albert A Anctil. *Tempered martensite embrittlement and fracture toughness in SAE 4340 steel*. Tech. rep. Watertown, Massachusetts: U.S. Army Materials Research Agency, Jan. 1967.

[29] P Bowen, C A Hippsley, and J F Knott. “Effects of segregation on brittle fracture and fatigue crack growth in coarse-grained, martensitic A533B pressure vessel steel”. In: *Acta Metallurgica* 32.5 (May 1984), pp. 637–647. ISSN: 0001-6160. DOI: 10.1016/0001-6160(84)90137-8.

[30] B C Edwards et al. “An AES study of temper embrittlement in a low alloy steel”. In: *Acta Metallurgica* 24.10 (Oct. 1976), pp. 957–967. ISSN: 0001-6160. DOI: 10.1016/0001-6160(76)90043-2.

[31] E D Hondros. “Grain boundary segregation assessment of investigative techniques”. In: *Grain boundary structure and properties*. Ed. by G A Chadwick and D A Smith. London, New York: Academic Press, 1976. Chap. 8, pp. 265–298.

[32] D Briggs and M P Seah. *Practical surface analysis, Volume 1: Auger and X-ray photoelectron spectroscopy*. 2nd ed. Vol. 1. Chichester: Wiley, 1990.

[33] Tien Tsou Tsong. *Atom-probe field ion microscopy: field ion emission and surfaces and interfaces at atomic resolution*. Cambridge ; Cambridge University Press, 1990. ISBN: 0521363799.

[34] L. Liu et al. “Making ultrastrong steel tough by grain-boundary delamination”. In: *Science* 368.6497 (June 2020), pp. 1347–1352. ISSN: 0036-8075. DOI: 10.1126/science.aba9413.

[35] D J O'Connor, B A Sexton, and R St C Smart. *Surface analysis methods in materials science*. Ed. by Roger St. C. Smart D. John O'Connor Brett A. Sexton. Berlin: Springer-Verlag, 1992. ISBN: 3540536116.

[36] T Ericsson. "Residual Stresses Produced by Quenching of Martensitic Steels". In: *Comprehensive Materials Processing*. Elsevier, 2014, pp. 271–298. DOI: 10.1016/B978-0-08-096532-1.01209-7.

[37] Masayoshi Kumagai et al. "Depth-profiling of residual stress and microstructure for austenitic stainless steel surface treated by cavitation, shot and laser peening". In: *Materials Science and Engineering: A* 813 (May 2021), p. 141037. ISSN: 09215093. DOI: 10.1016/j.msea.2021.141037. URL: https://linkinghub.elsevier.com/retrieve/pii/S0921509321003063.

[38] Sebastian Schneider et al. "Investigation on residual stress induced by multiple EDM discharges". In: *Procedia CIRP* 102 (Jan. 2021), pp. 482–487. ISSN: 2212-8271. DOI: 10.1016/J.PROCIR.2021.09.082.

[39] Ismail Cevdet Noyan and Jerome B. Cohen. *Residual stress : measurement by diffraction and interpretation.* New York : Springer, 1987, 276 blz. ISBN: 0387963782.

[40] Y. Murakami and H. Usuki. "Quantitative evaluation of effects of non-metallic inclusions on fatigue strength of high strength steels. II: Fatigue limit evaluation based on statistics for extreme values of inclusion size". In: *International Journal of Fatigue* 11.5 (Sept. 1989), pp. 299–307. ISSN: 0142-1123. DOI: 10.1016/0142-1123(89)90055-8.

[41] G Clark, Robert O Ritchie, and J F Knott. "Segregation Effects and the Toughness of Untempered Low-Alloy Steels". In: *Nature Physical Science* 239.94 (Oct. 1972), pp. 104–106. ISSN: 0300-8746. DOI: 10.1038/physci239104a0.

[42] P Maier and R G Faulkner. "Effects of thermal history and microstructure on phosphorus and manganese segregation at grain boundaries in C–Mn welds". In: *Materials Characterization* 51.1 (Aug. 2003), pp. 49–62. ISSN: 1044-5803. DOI: 10.1016/J.MATCHAR.2003.09.010.

[43] R P Messmer and C L Briant. "The role of chemical bonding in grain boundary embrittlement". In: *Acta Metallurgica* 30.2 (Feb. 1982), pp. 457–467. ISSN: 0001-6160. DOI: 10.1016/0001-6160(82)90226-7.

[44] C L Briant and R P Messmer. "An electronic model for the grain boundary embrittlement of iron, nickel and chromium and their alloys by antimony". In: *Acta Metallurgica* 32.11 (Nov. 1984), pp. 2043–2052. ISSN: 0001-6160. DOI: 10.1016/0001-6160(84)90183-4.

A

SEM Images

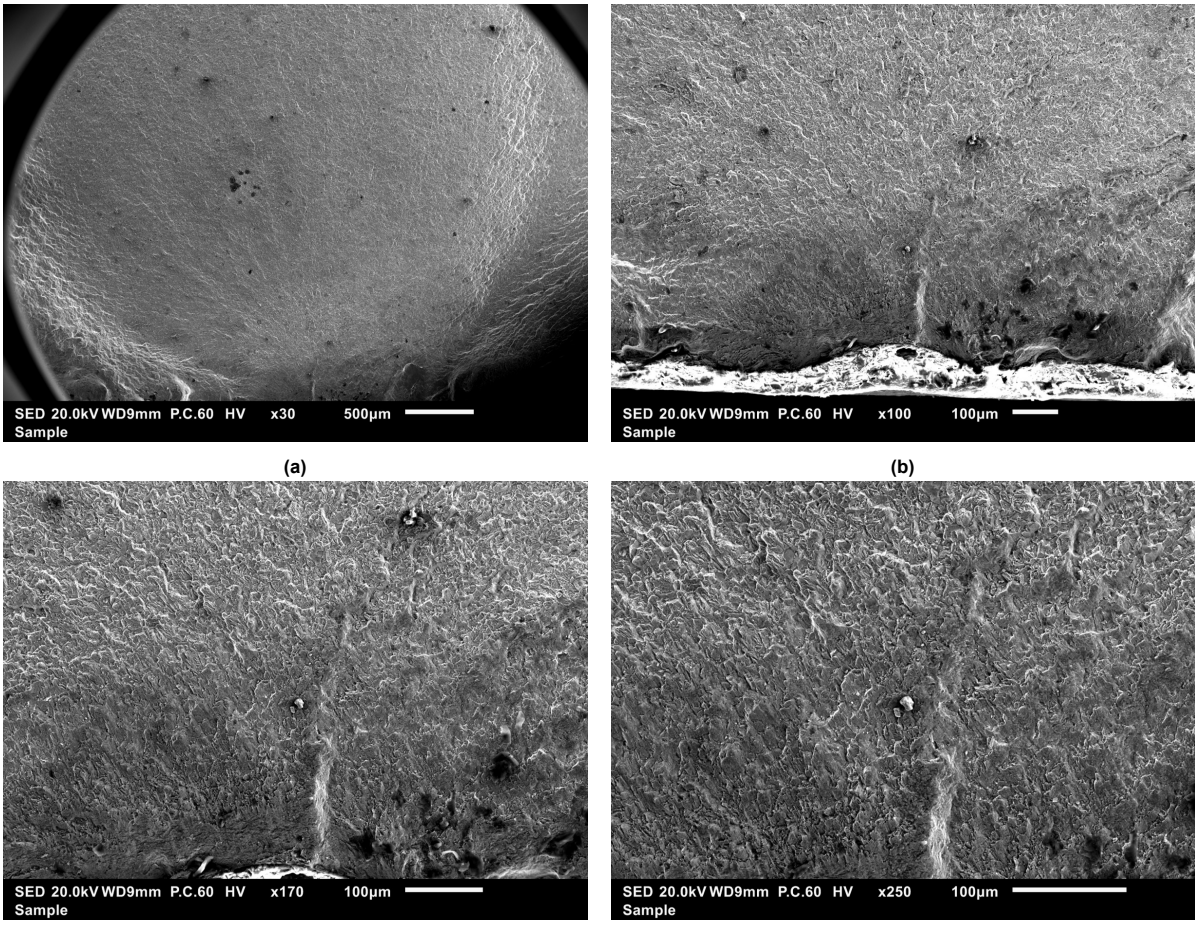

Figure A.1: SEM overview of the point initiation in Reference

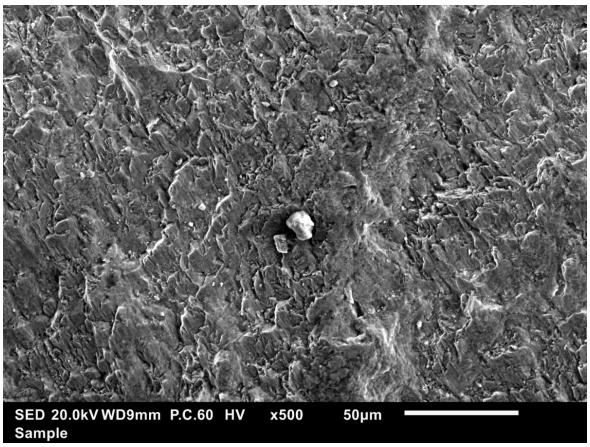

(e)

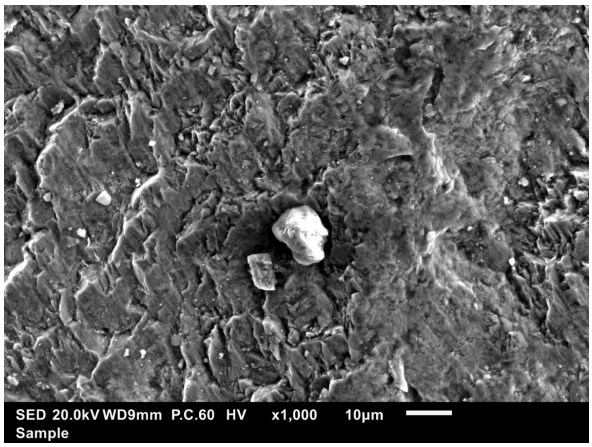

(f)

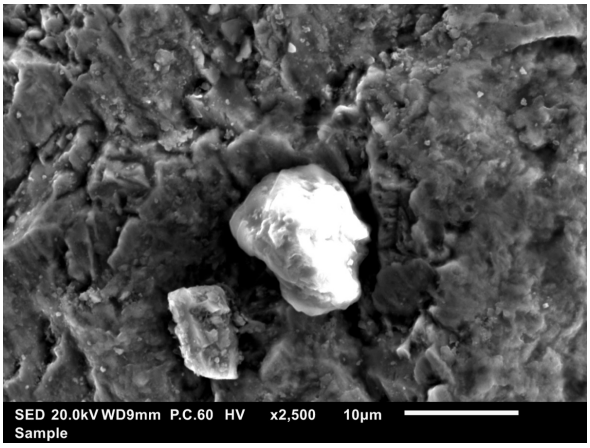

(g)

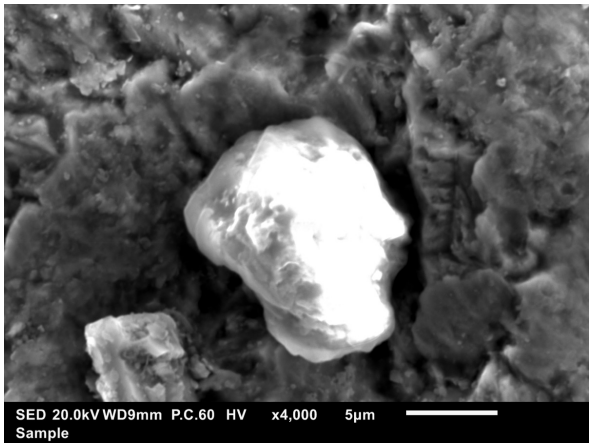

(h)

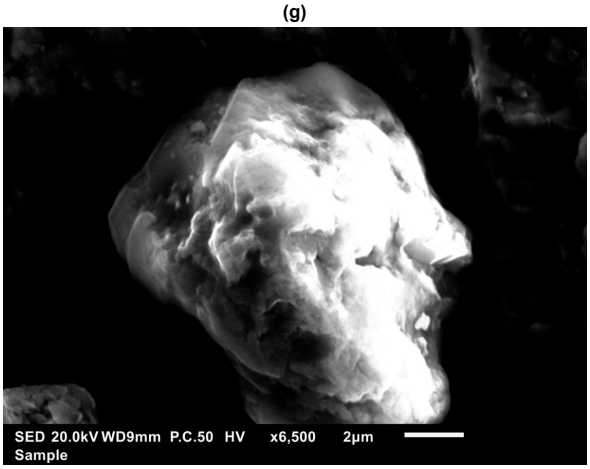

(i)

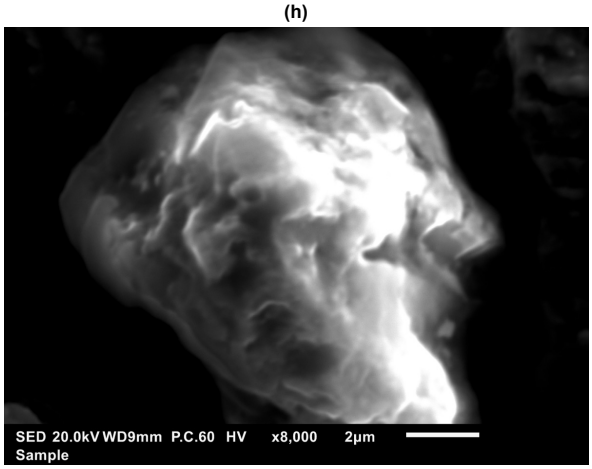

(j)

Figure A.1: SEM overview of the point initiation in Reference

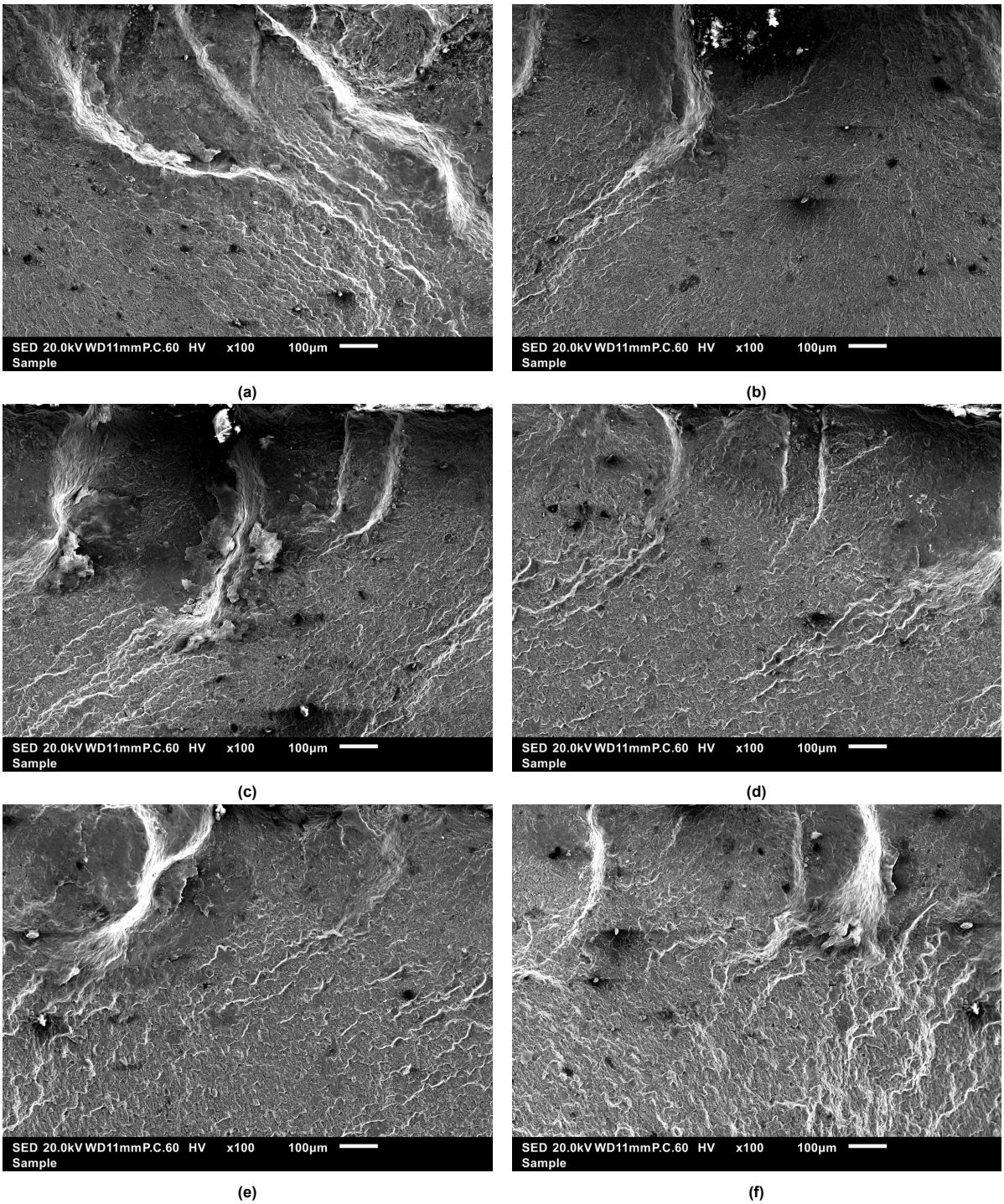

Figure A.2: SEM overview of the line initiation in Reference

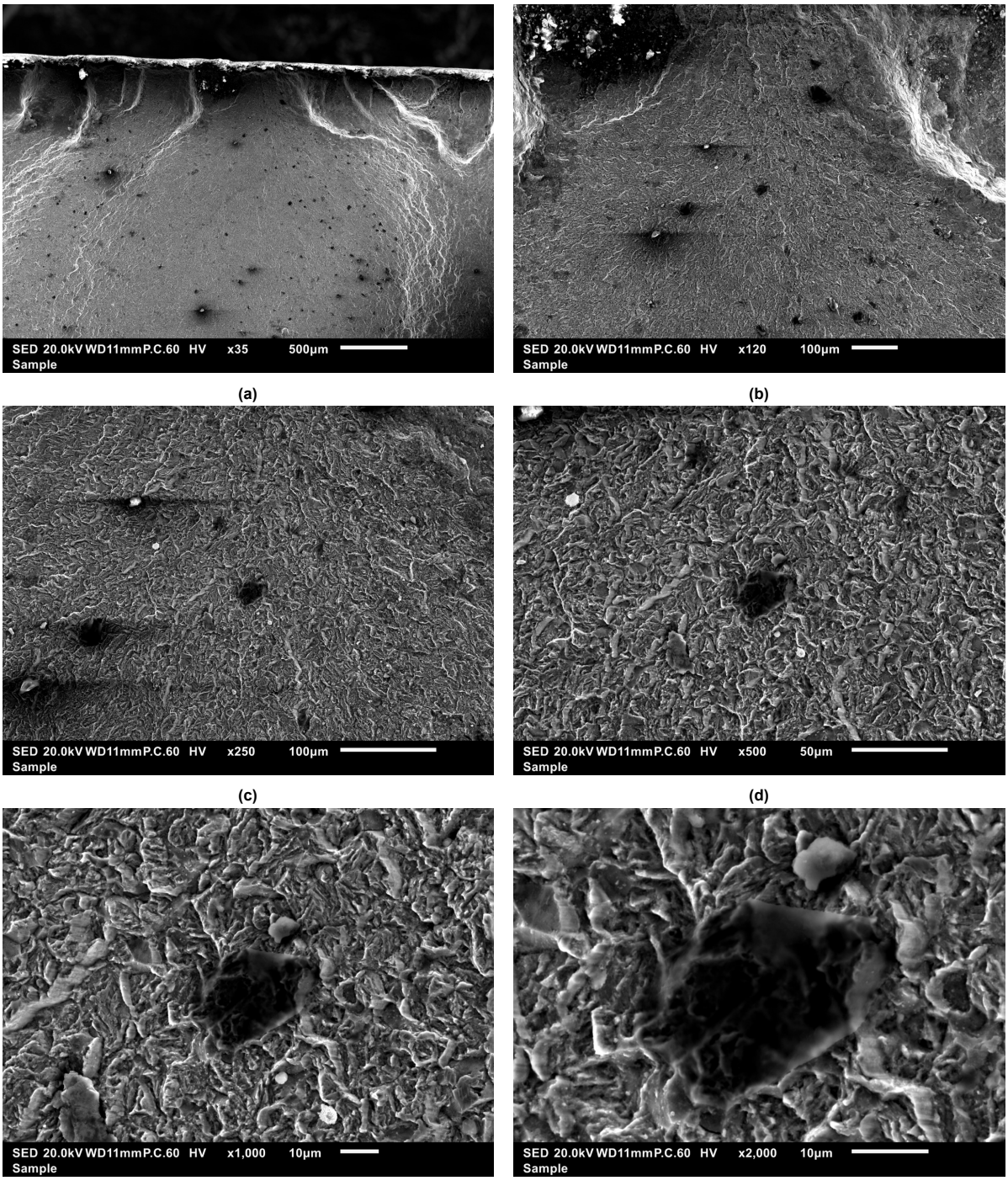

Figure A.3: SEM overview of the intergranular fracture in Reference

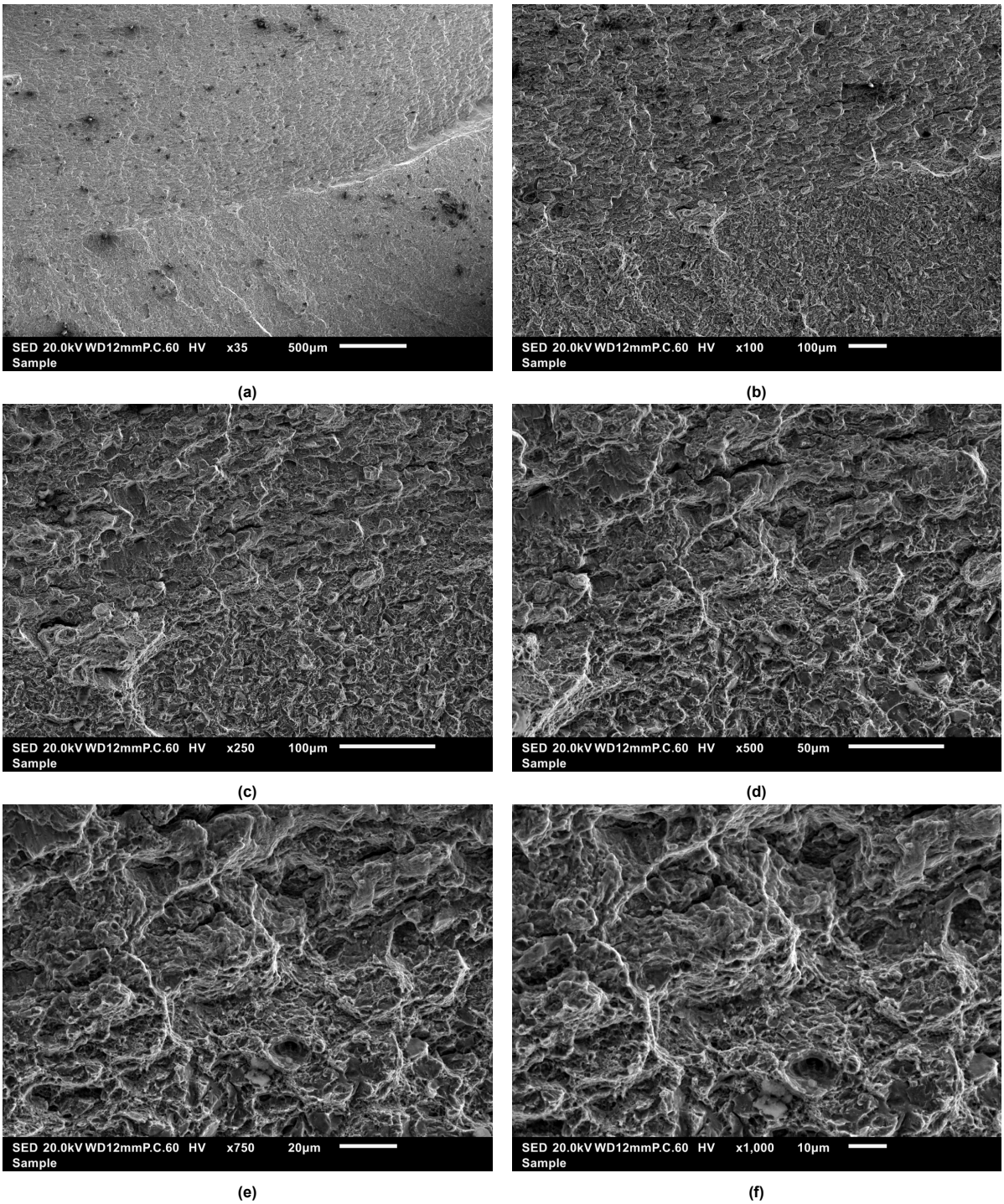

Figure A.4: SEM overview of the transition of fracture mode in Reference

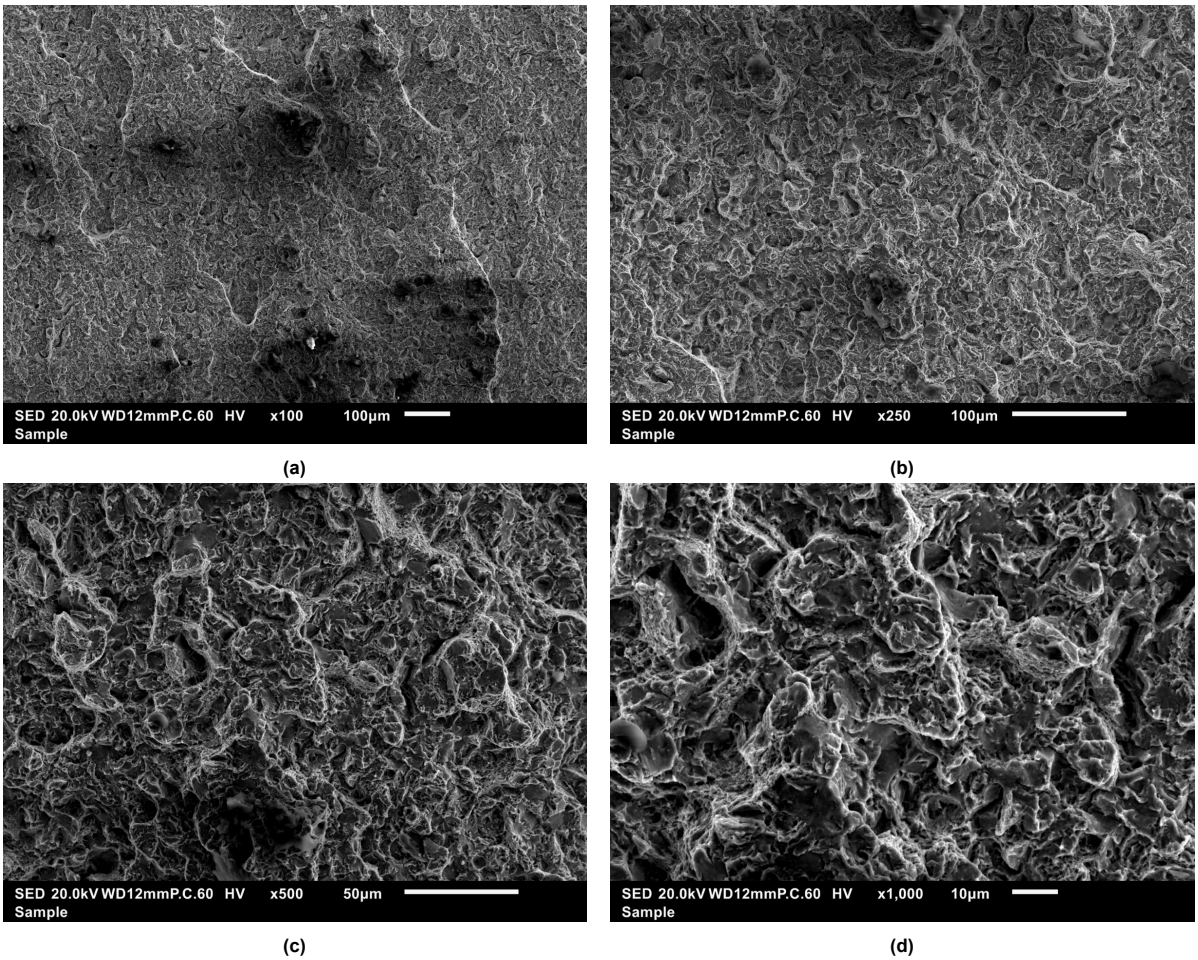

Figure A.5: SEM overview of the final fracture in Reference

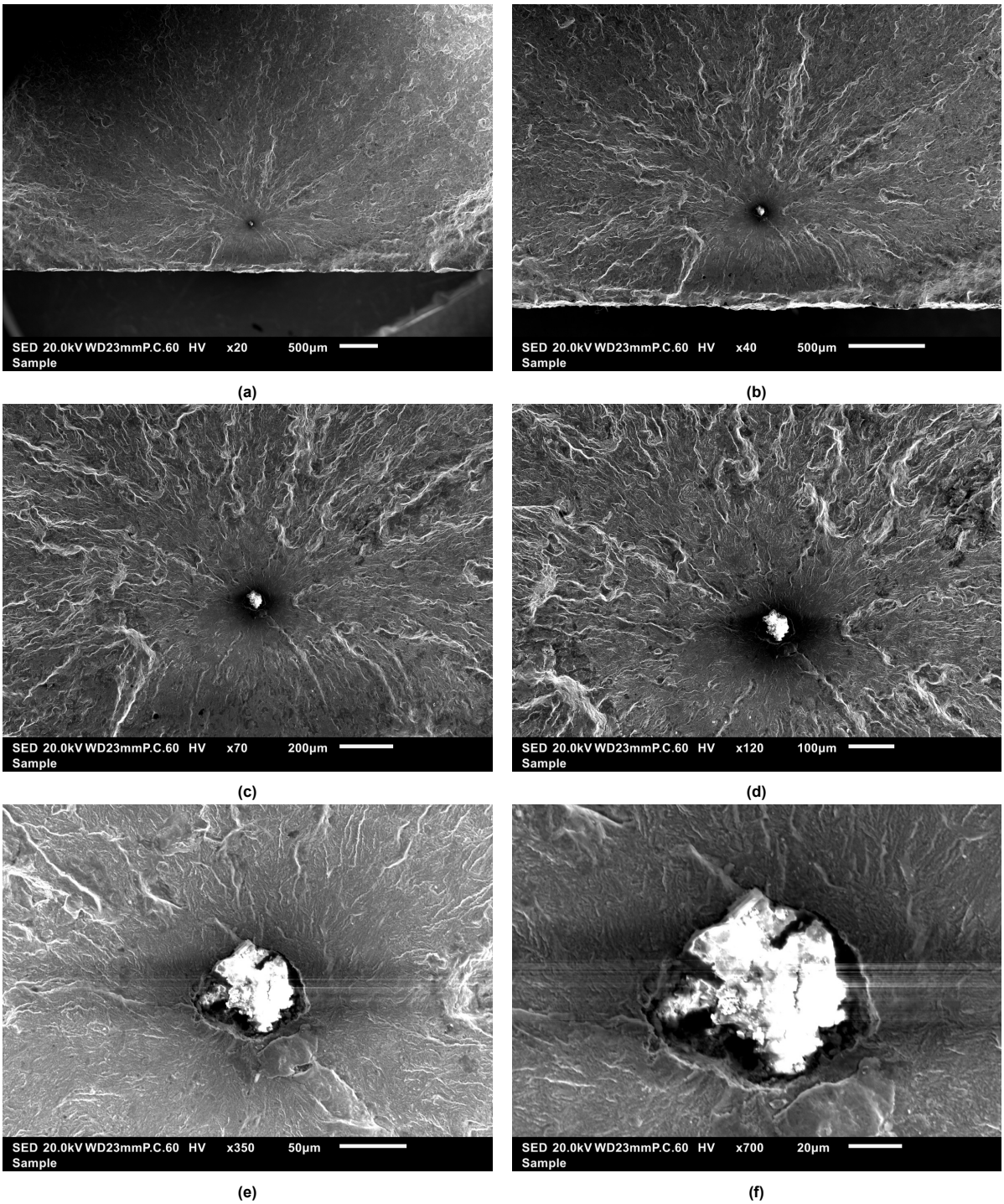

Figure A.6: SEM overview of the initiation in Gasloos

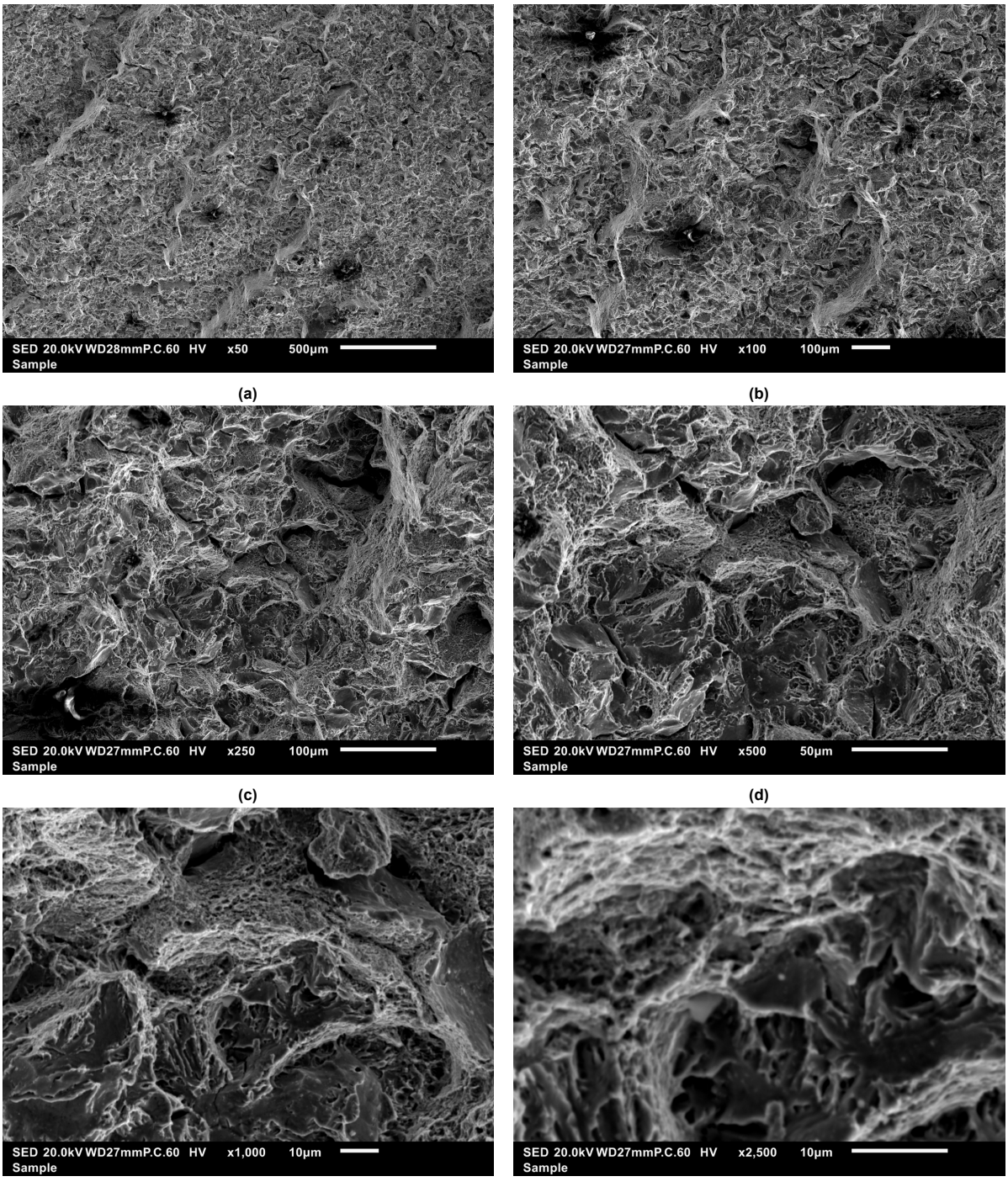

Figure A.7: SEM overview of the final fracture in Gasloos

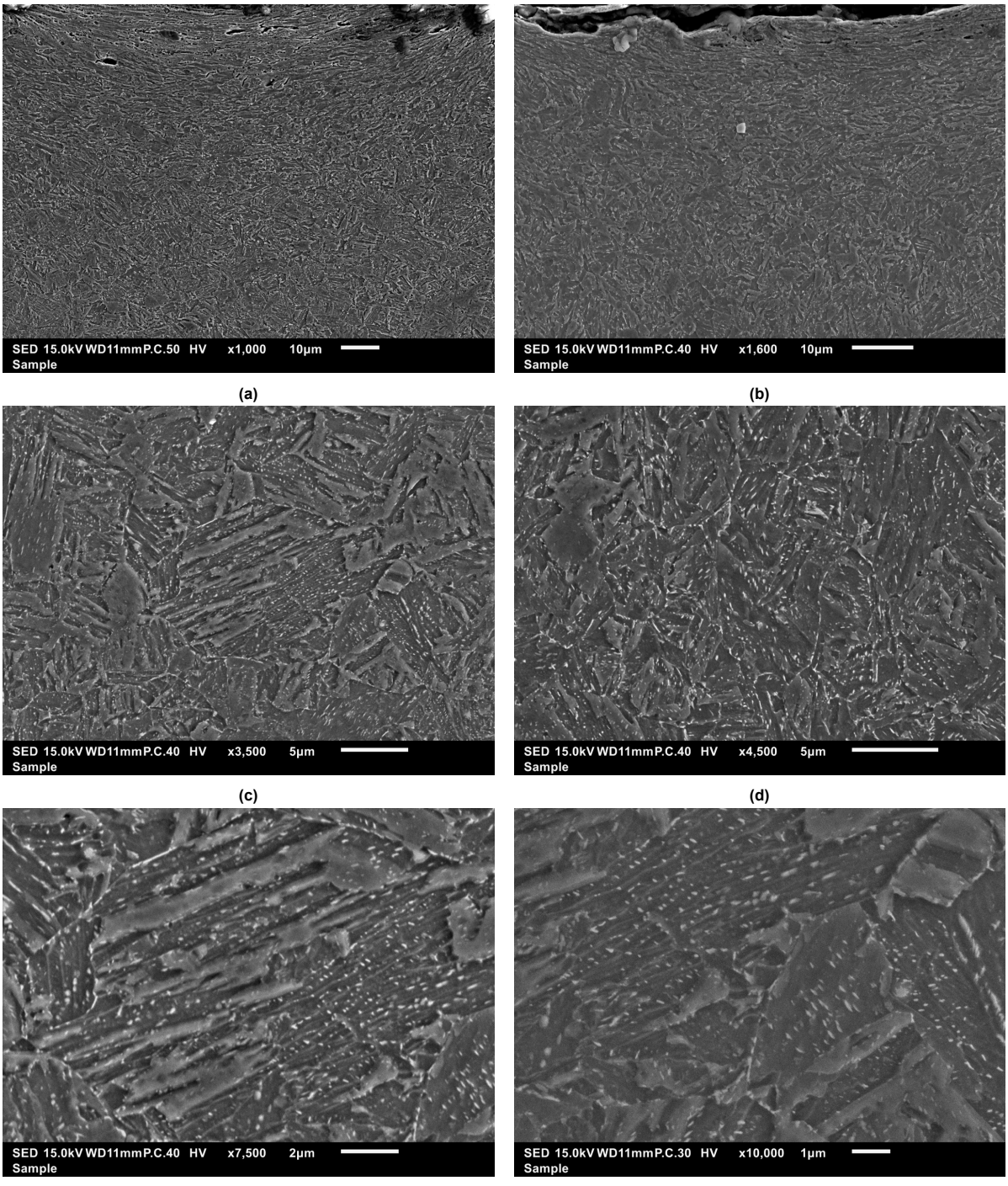

Figure A.8: SEM overview of the microstructure of Reference

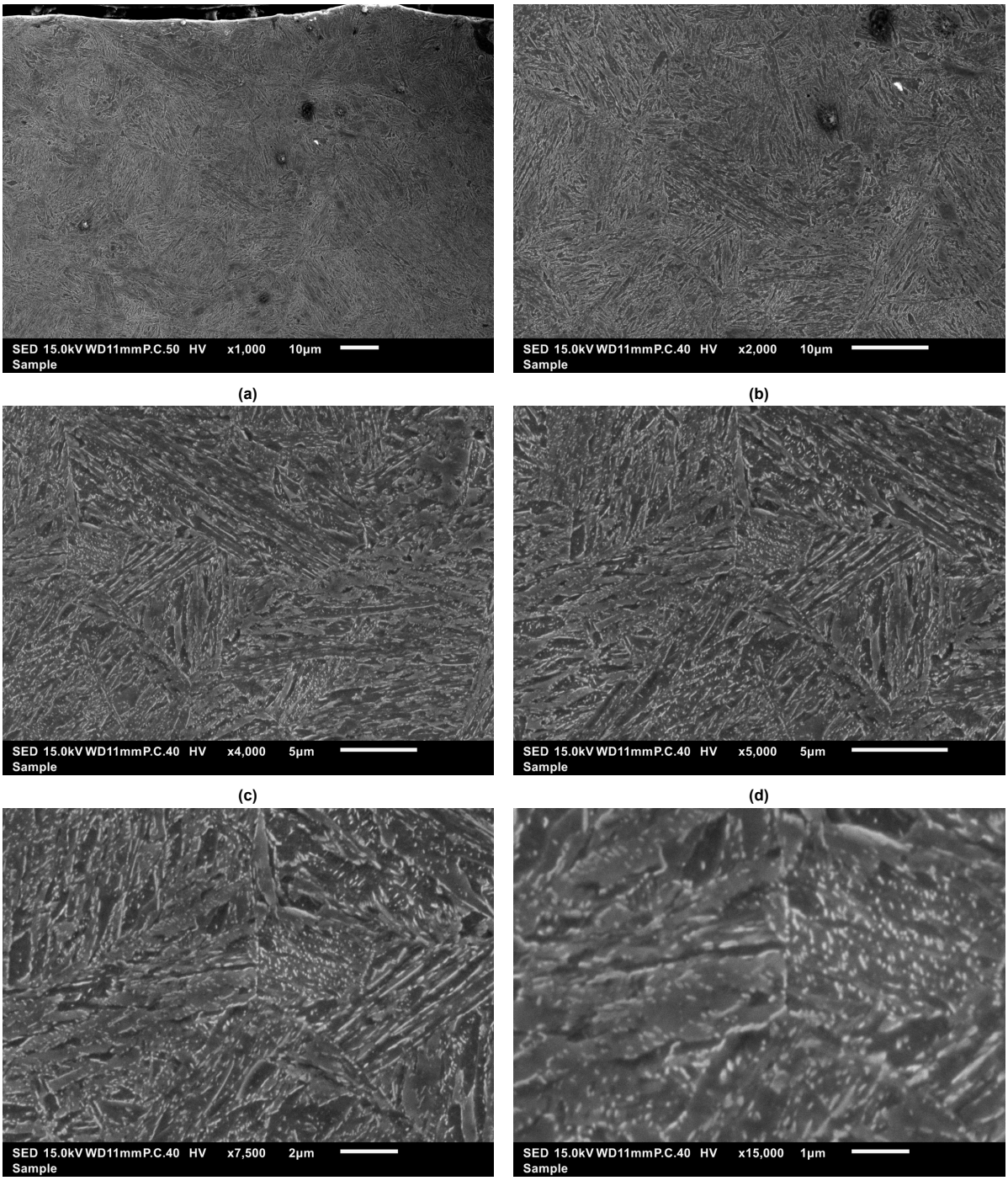

Figure A.9: SEM overview of the microstructure of Gasloos

B

XRD Measurements

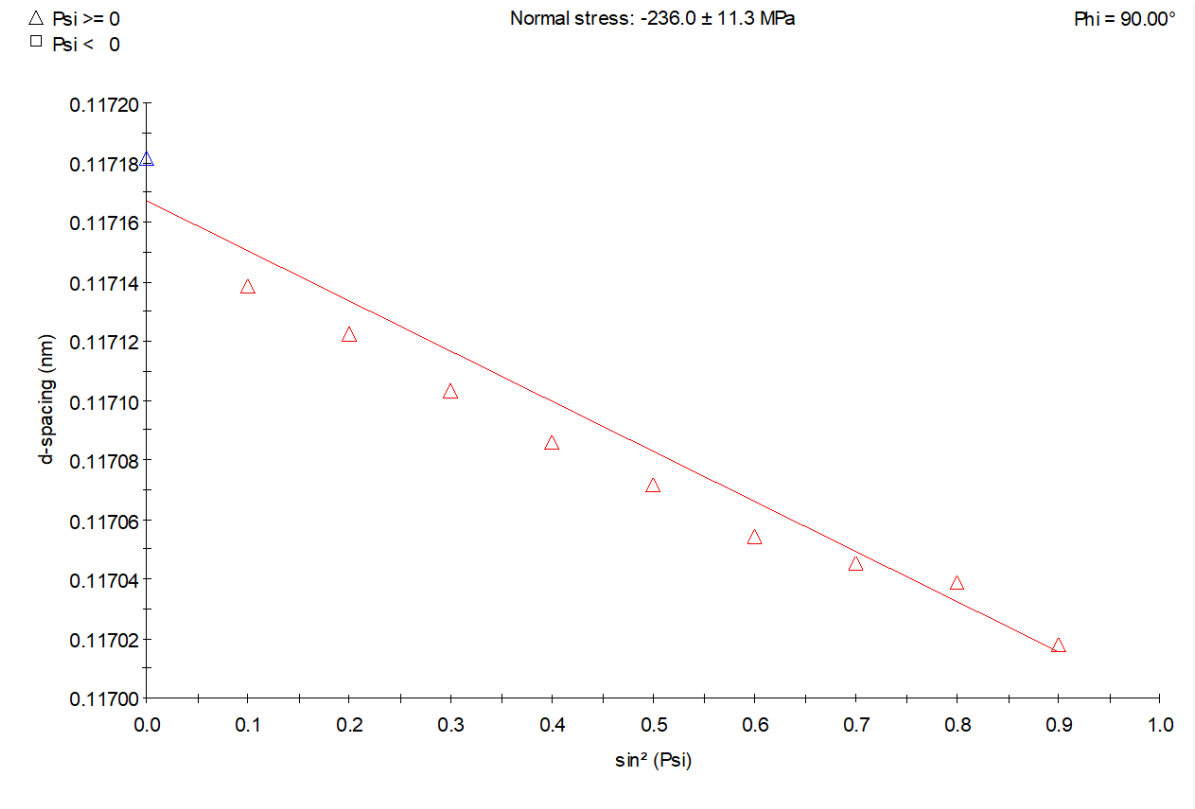

Figure B.1: Reference d vs $\sin^2\psi$ plot of the ferrite(211) reflection for $x = 0mm$

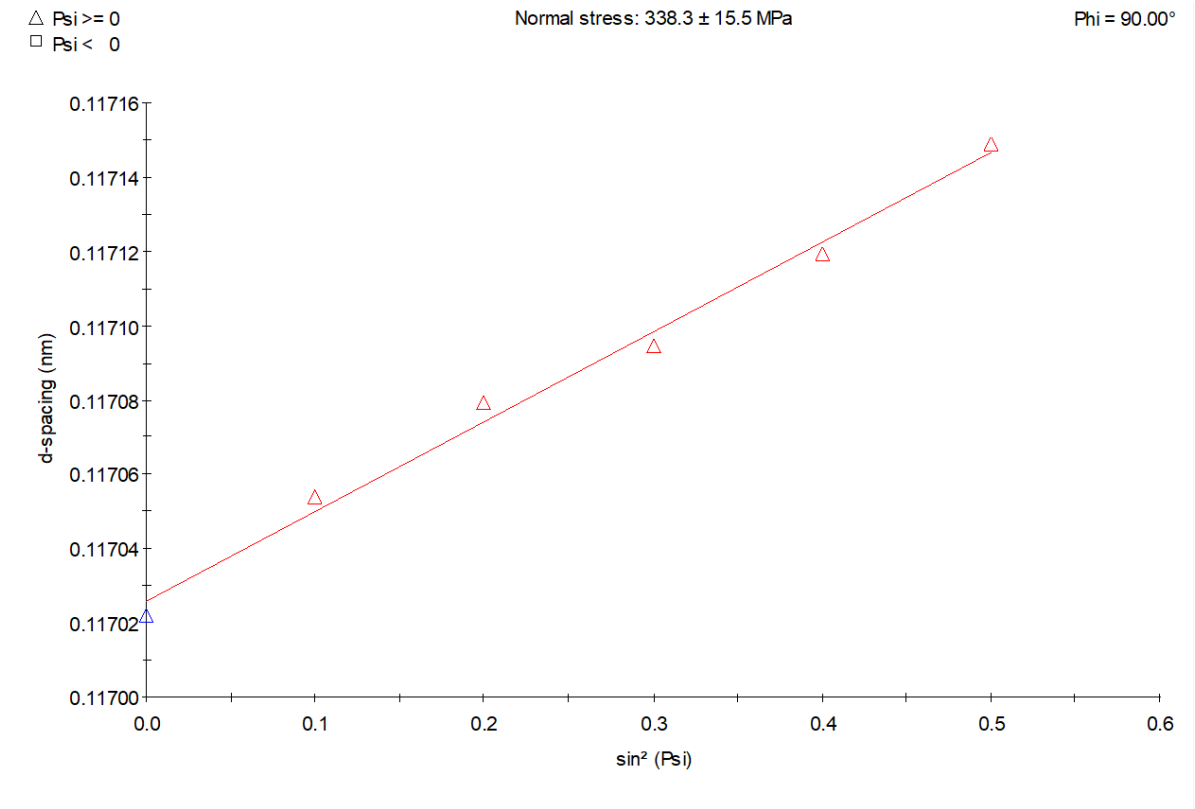

Figure B.2: Reference d vs $\sin^2\psi$ plot of the ferrite(211) reflection for $x \approx 0.05mm$

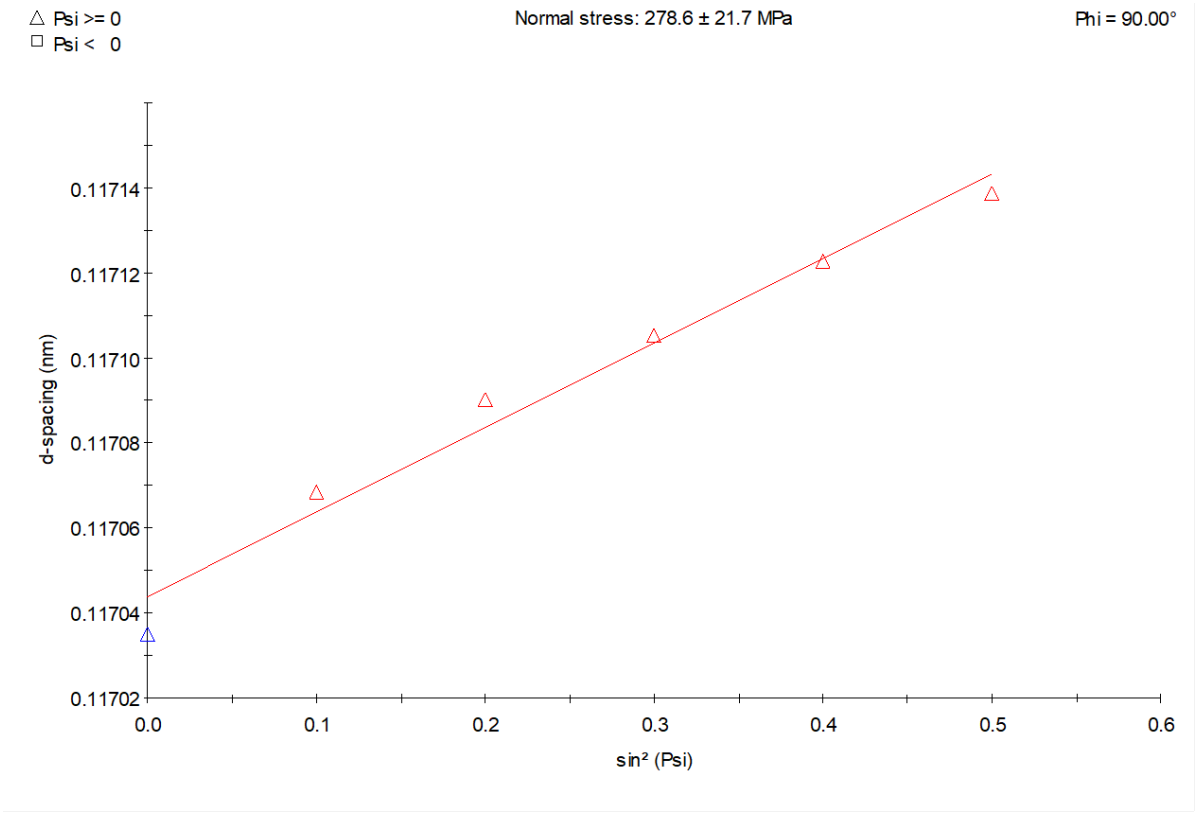

Figure B.3: Reference d vs $\sin^2\psi$ plot of the ferrite(211) reflection for $x \approx 0.10mm$

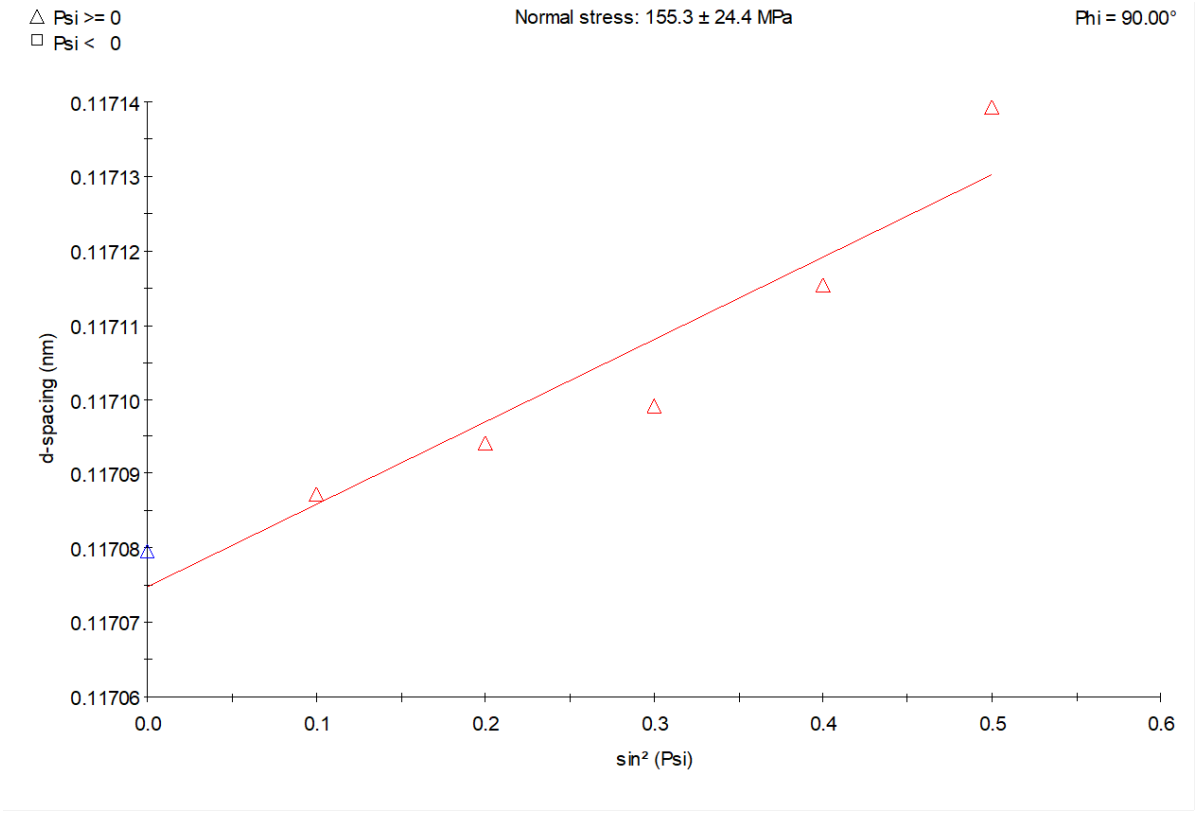

Figure B.4: Reference d vs $\sin^2\psi$ plot of the ferrite(211) reflection for $x \approx 0.15mm$

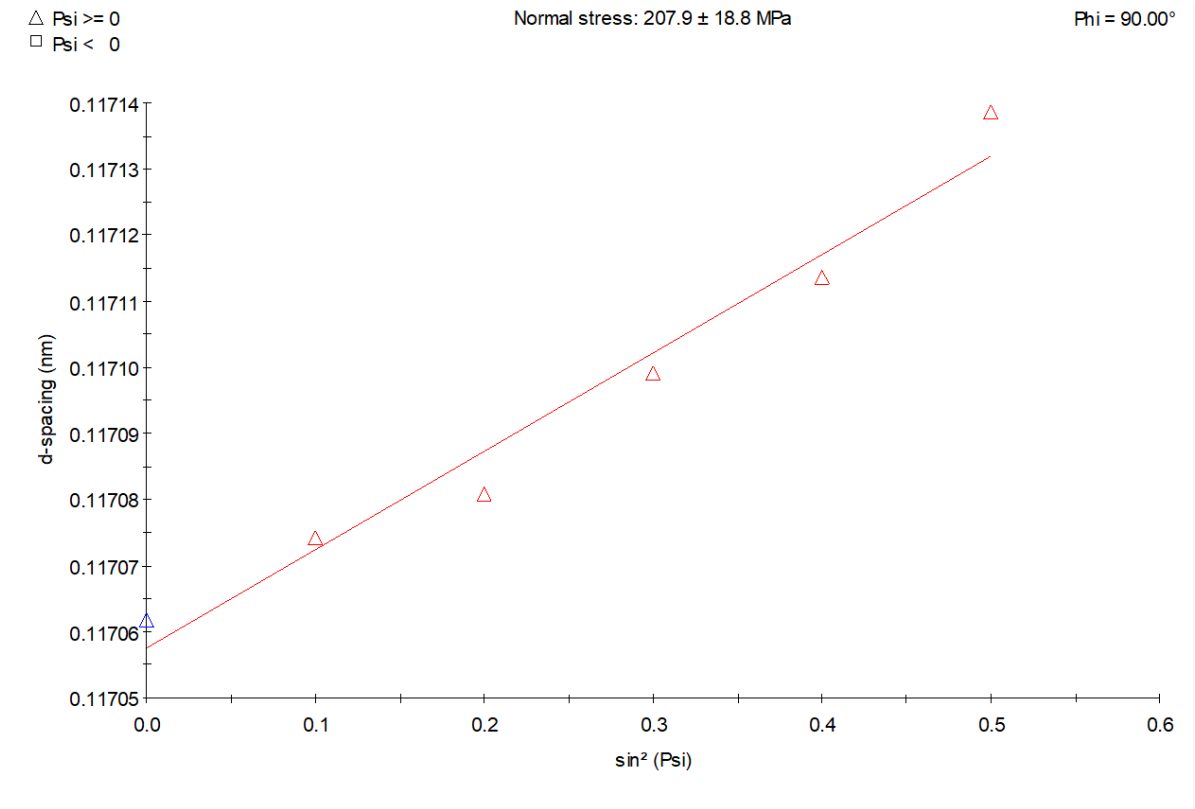

Figure B.5: Reference d vs $\sin^2\psi$ plot of the ferrite(211) reflection for $x \approx 0.20mm$

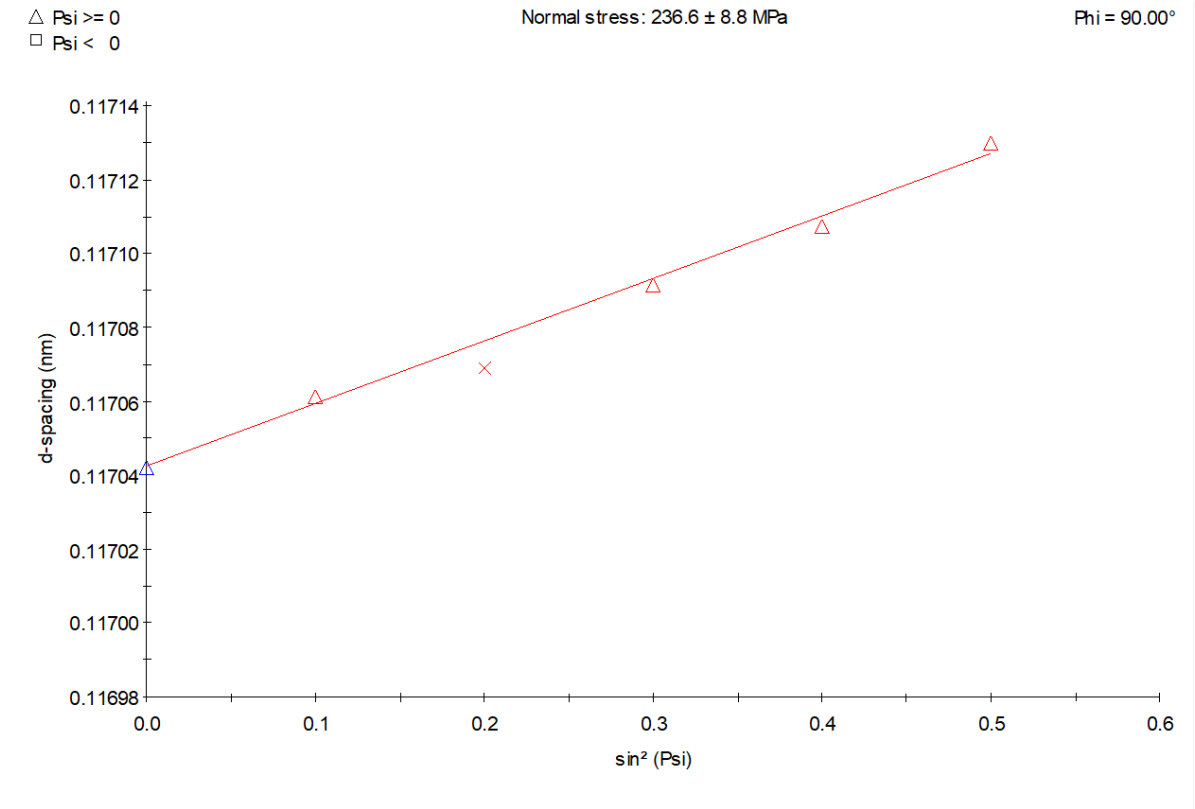

Figure B.6: Reference d vs $\sin^2\psi$ plot of the ferrite(211) reflection for $x \approx 0.25mm$

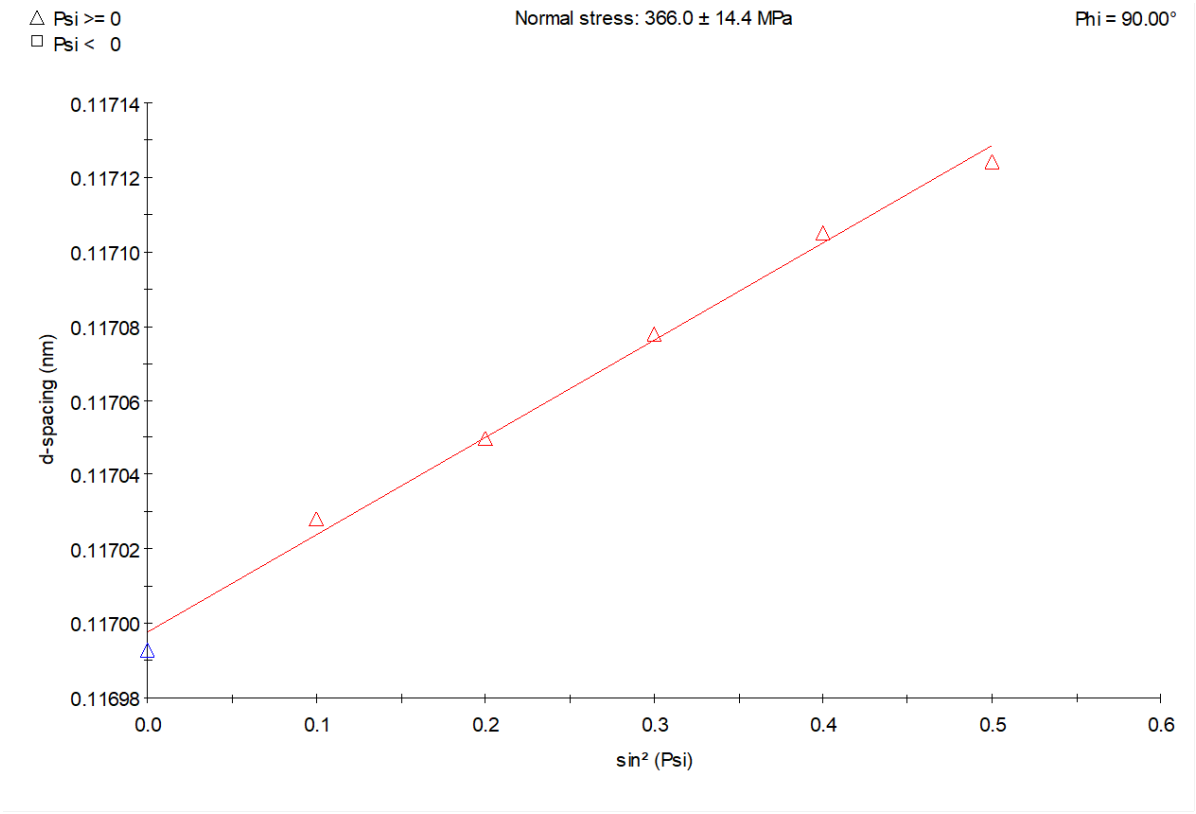

Figure B.7: Reference d vs $\sin^2\psi$ plot of the ferrite(211) reflection for $x \approx 0.30mm$

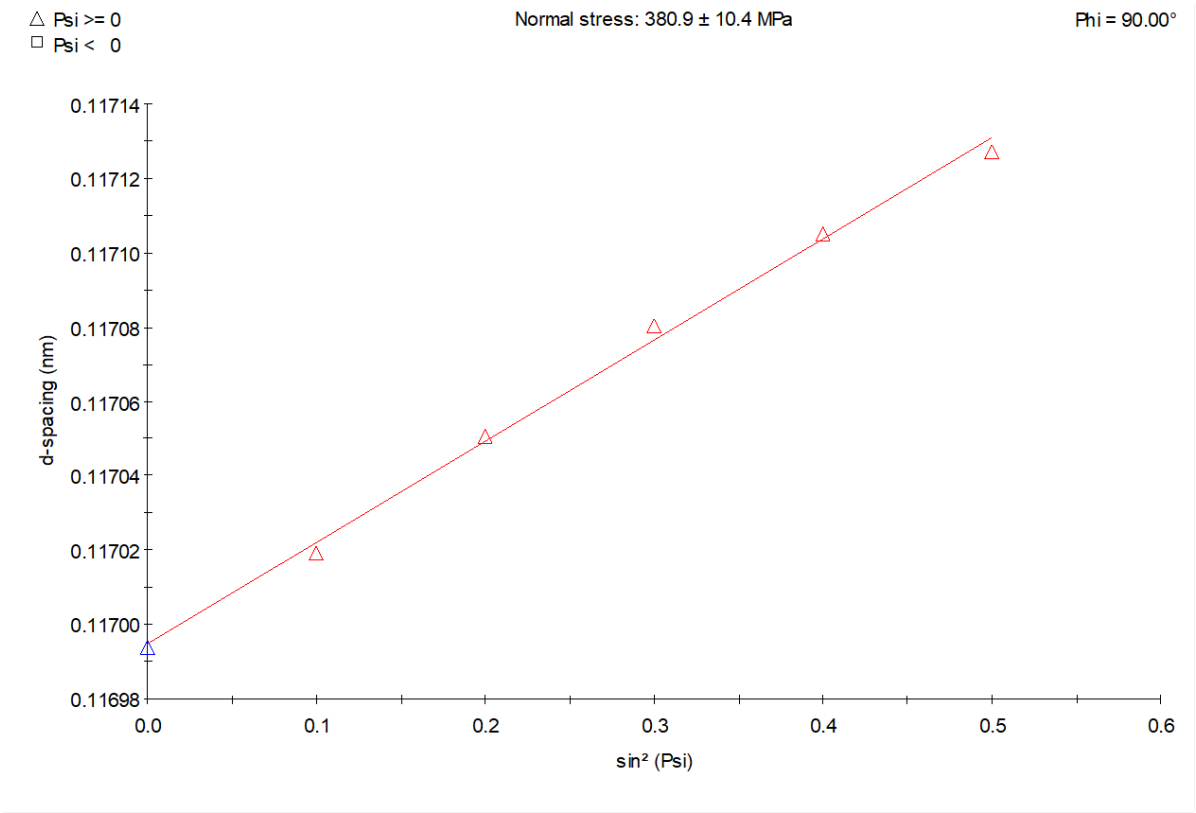

Figure B.8: Reference d vs $\sin^2\psi$ plot of the ferrite(211) reflection for $x \approx 0.35mm$

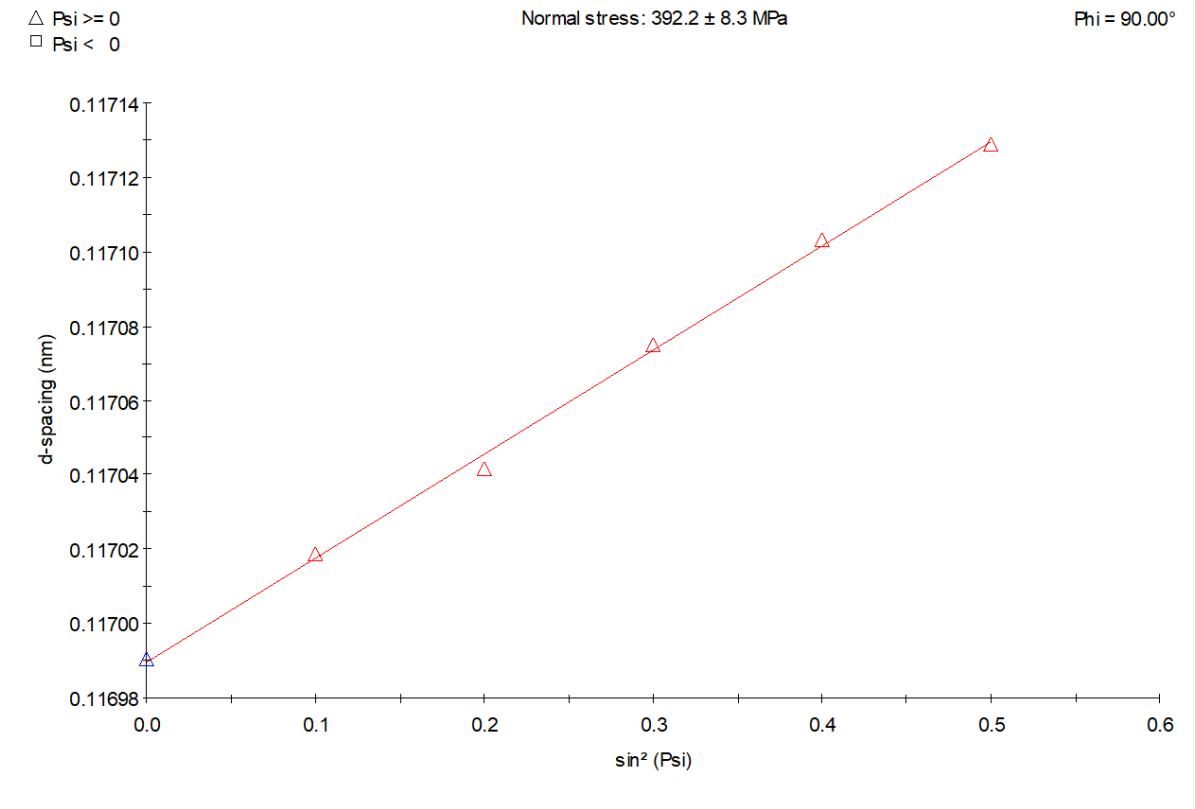

Figure B.9: Reference d vs $\sin^2\psi$ plot of the ferrite(211) reflection for $x \approx 0.40mm$

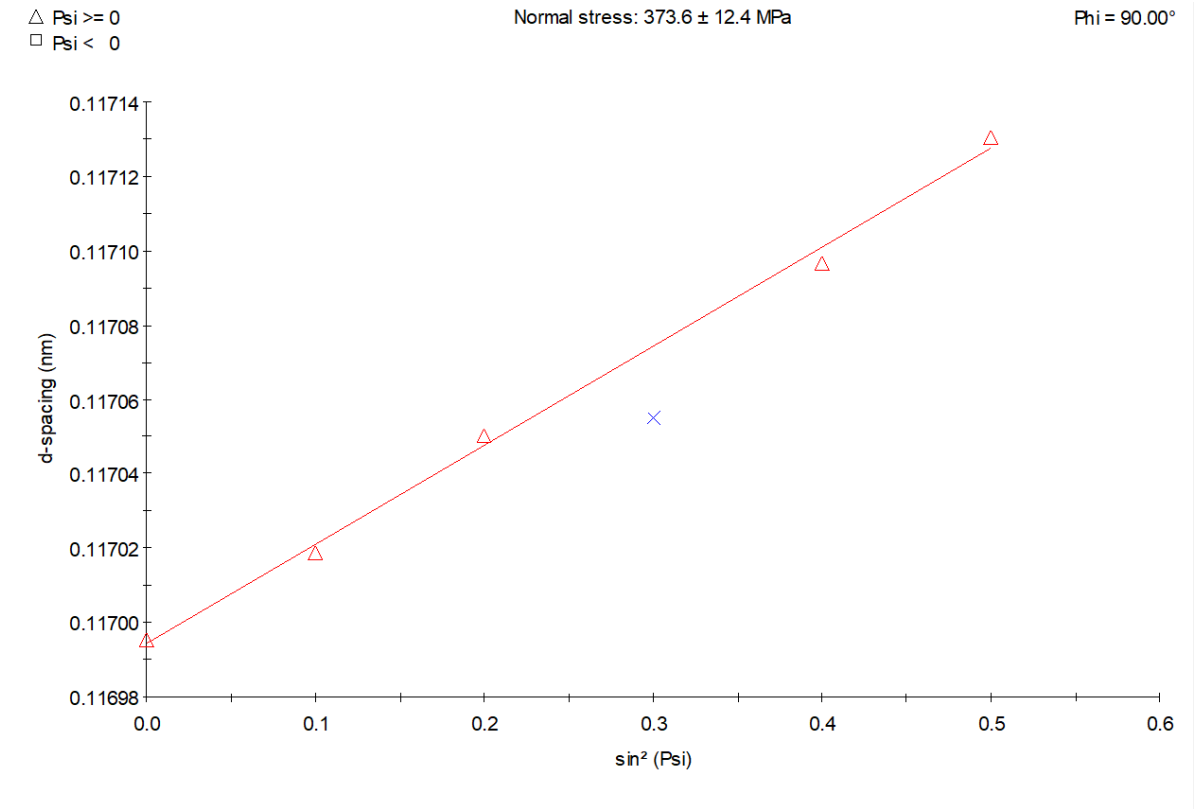

Figure B.10: Reference d vs $\sin^2\psi$ plot of the ferrite(211) reflection for $x \approx 0.45mm$

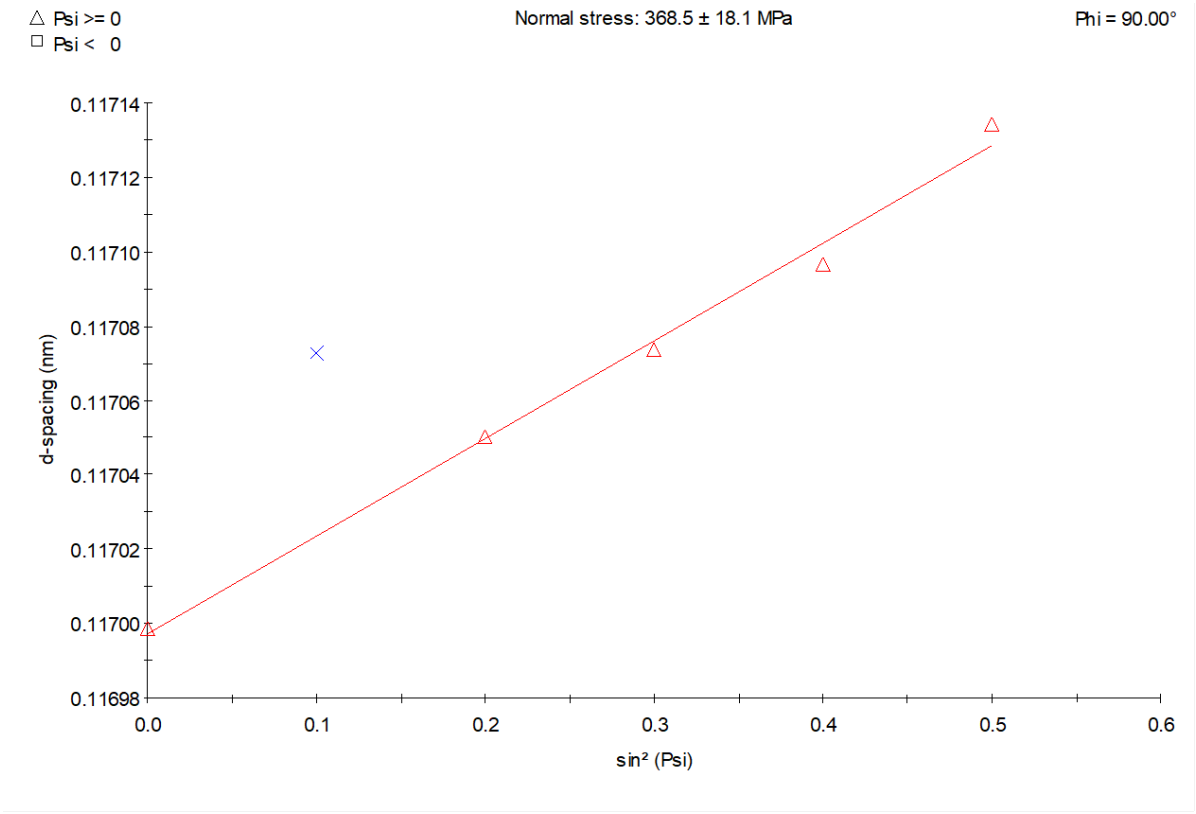

Figure B.11: Reference d vs $\sin^2\psi$ plot of the ferrite(211) reflection for $x \approx 0.50mm$

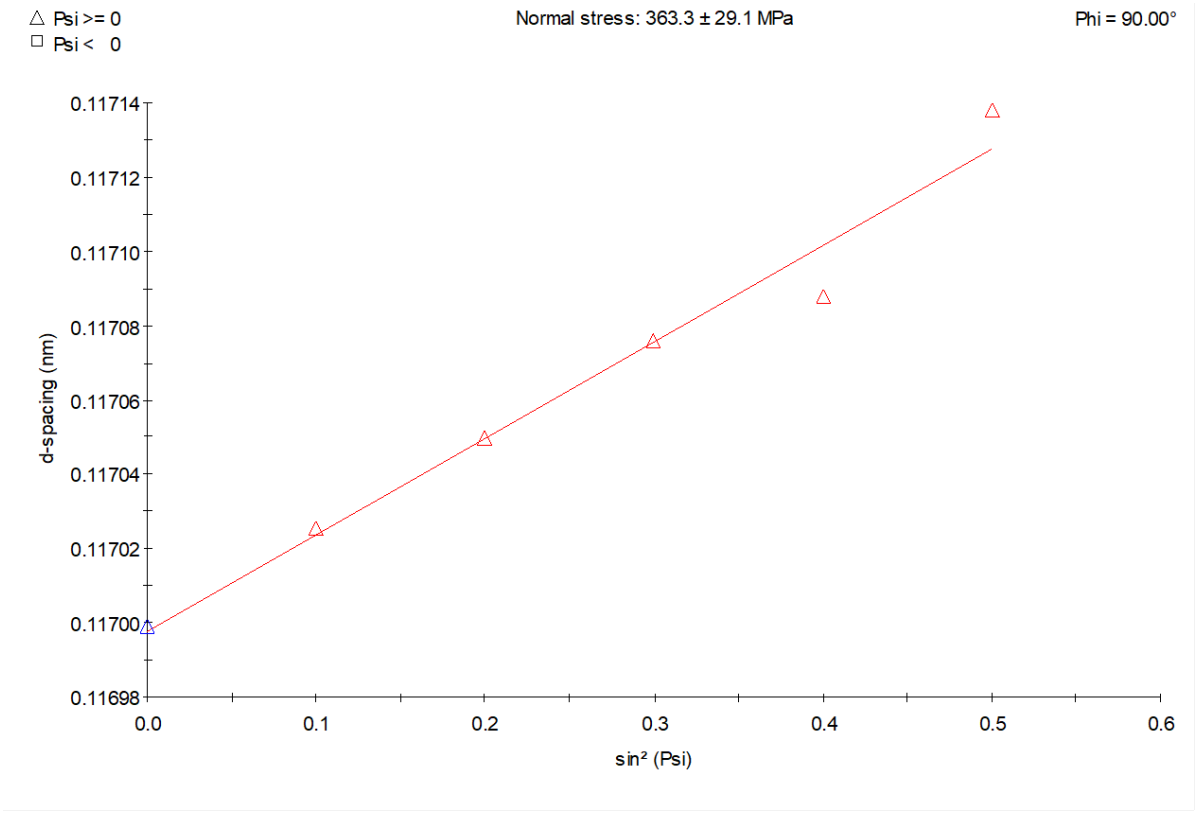

Figure B.12: Reference d vs $\sin^2\psi$ plot of the ferrite(211) reflection for $x \approx 0.55mm$

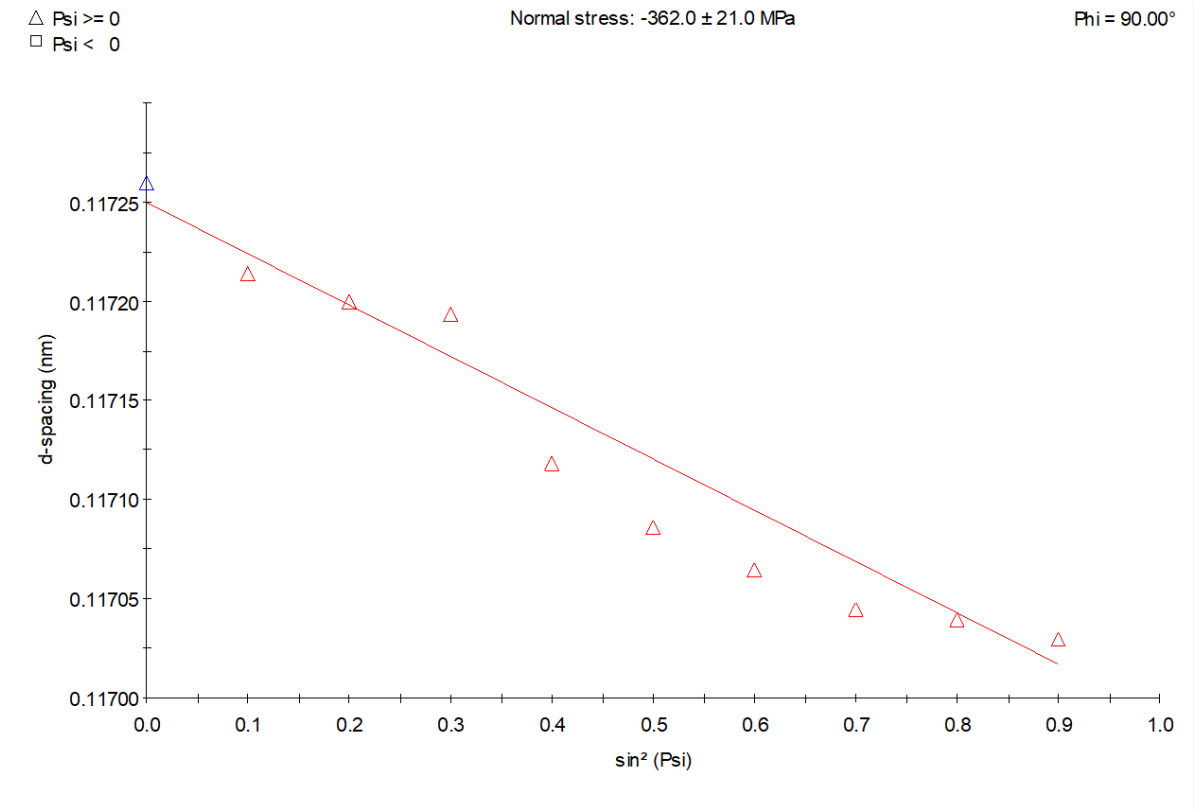

Figure B.13: Gasloos d vs $\sin^2\psi$ plot of the ferrite(211) reflection for $x = 0mm$

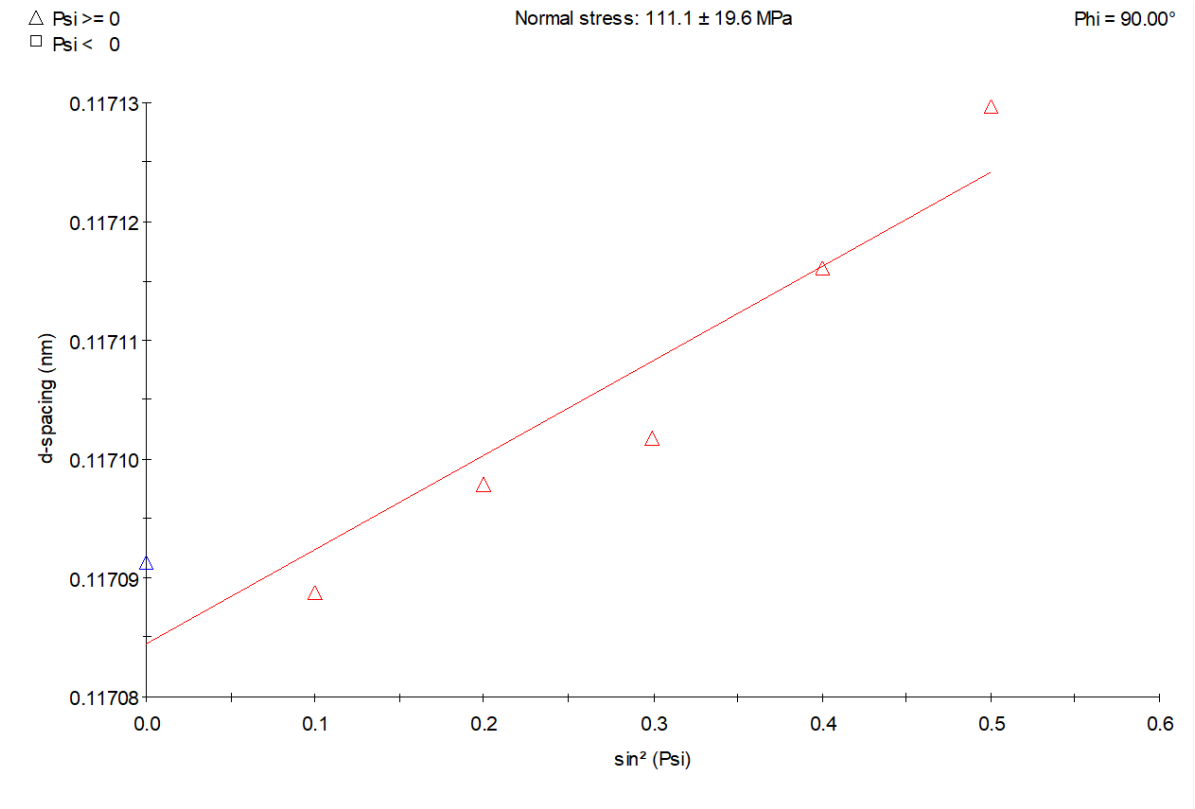

Figure B.14: Gasloos d vs $\sin^2\psi$ plot of the ferrite(211) reflection for $x \approx 0.05mm$

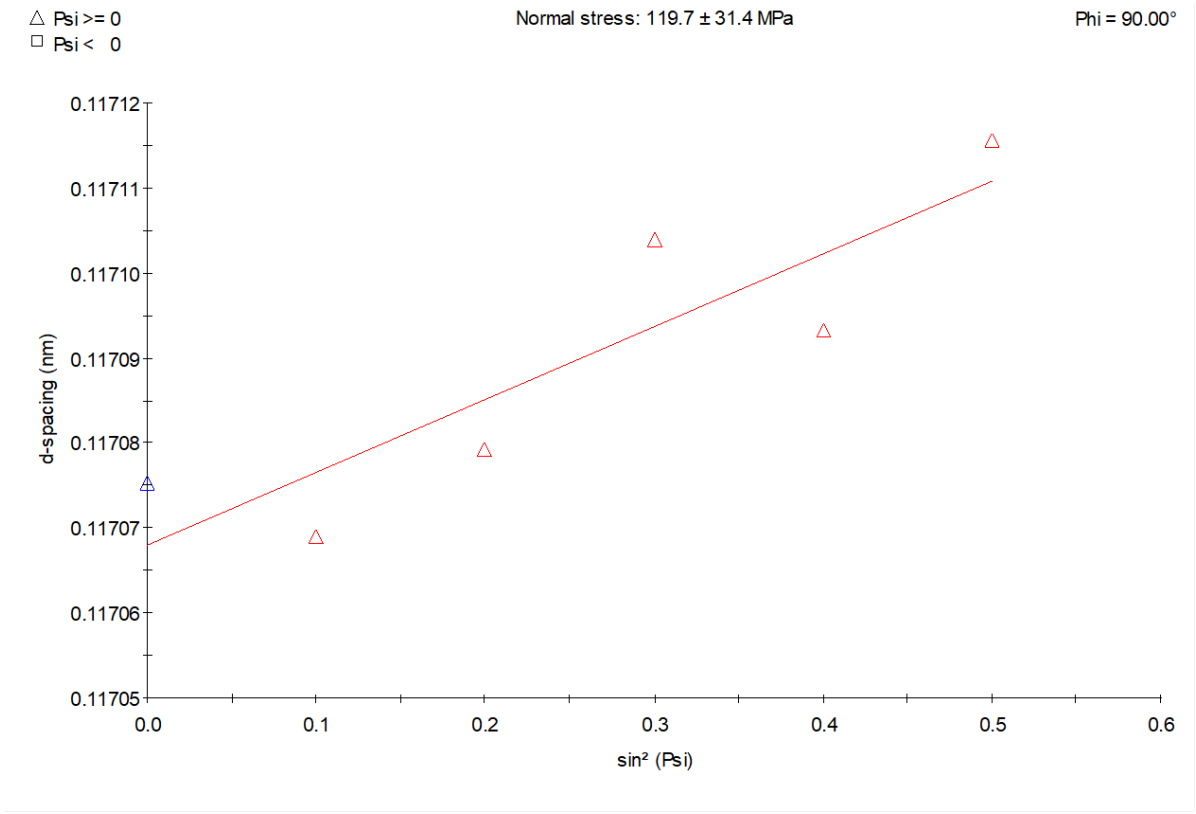

Figure B.15: Gasloos d vs $\sin^2\psi$ plot of the ferrite(211) reflection for $x \approx 0.10mm$

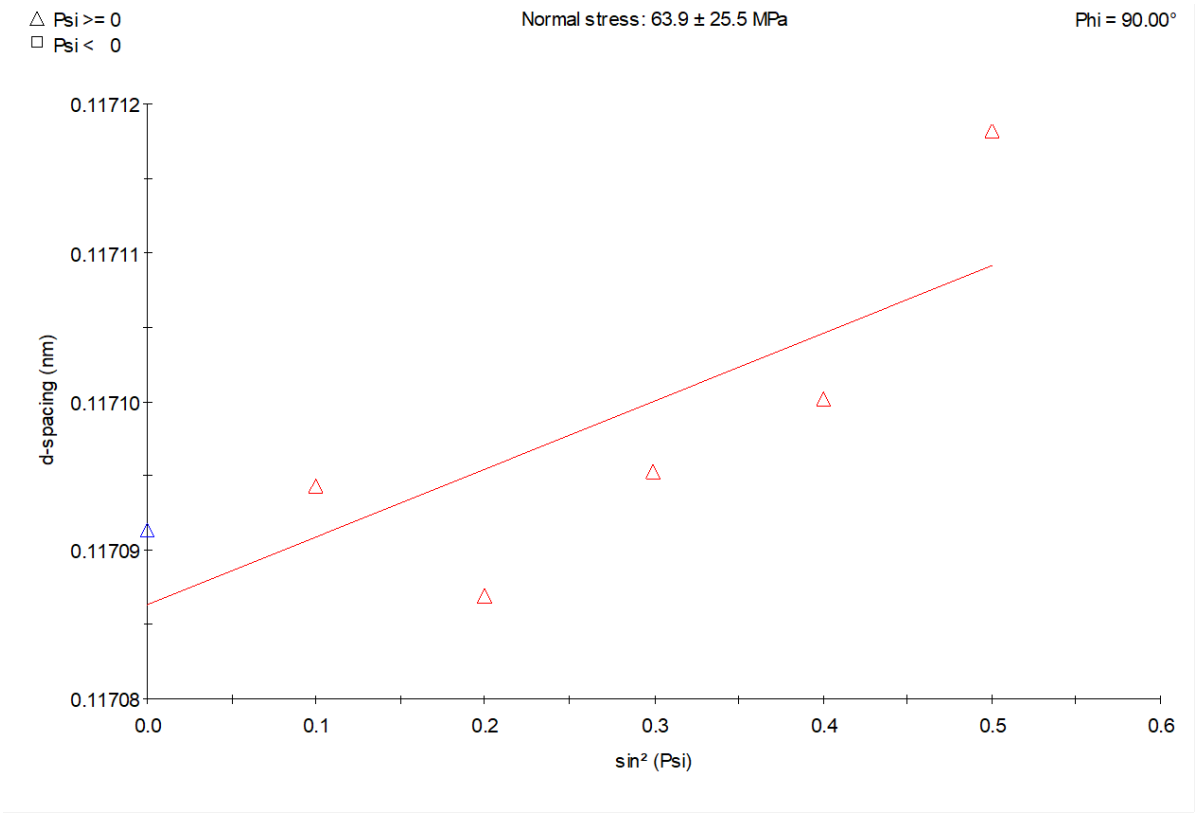

Figure B.16: Gasloos d vs $\sin^2\psi$ plot of the ferrite(211) reflection for $x \approx 0.15mm$

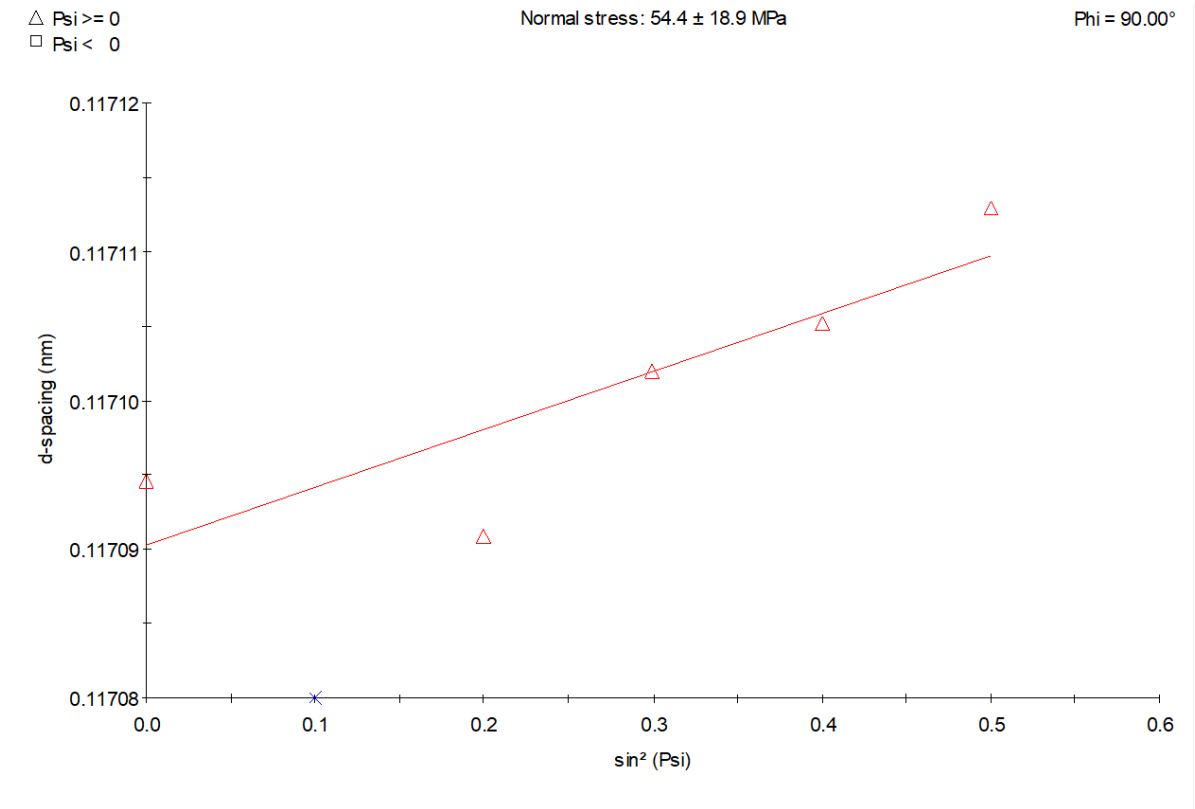

Figure B.17: Gasloos d vs $\sin^2\psi$ plot of the ferrite(211) reflection for $x \approx 0.20mm$

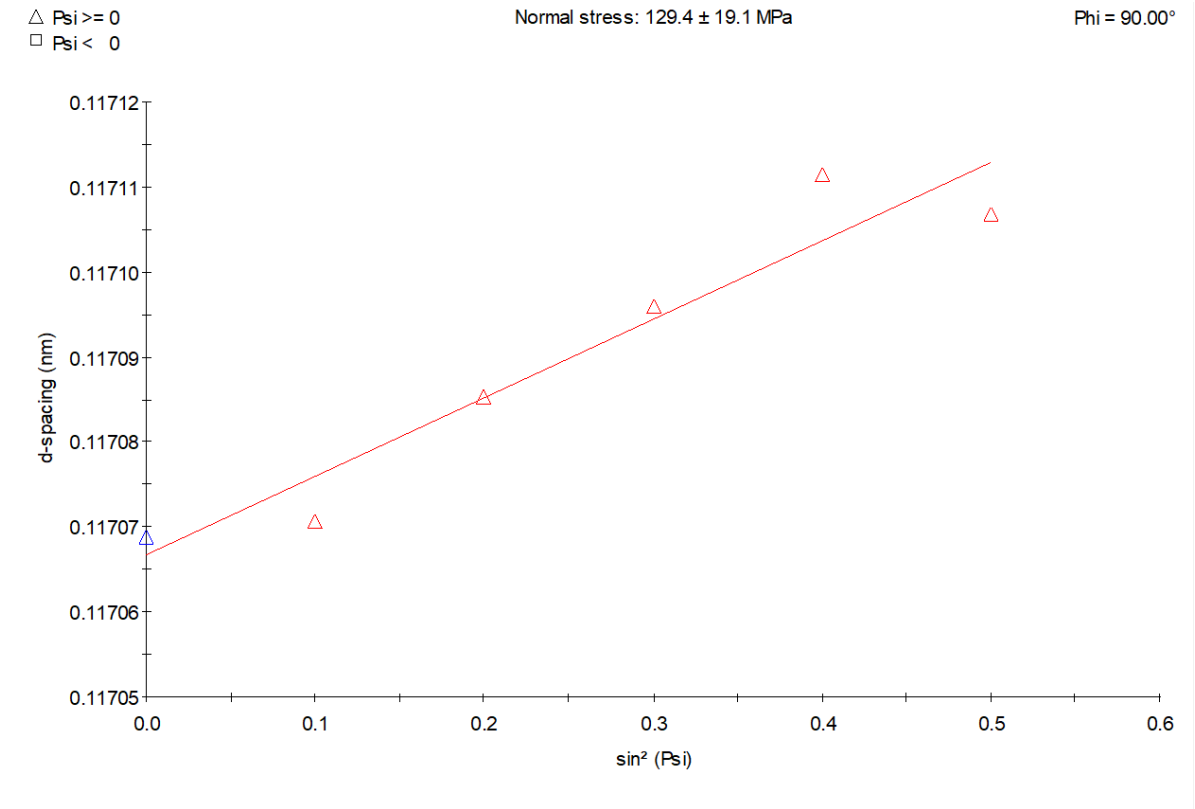

Figure B.18: Gasloos d vs $\sin^2\psi$ plot of the ferrite(211) reflection for $x \approx 0.25mm$

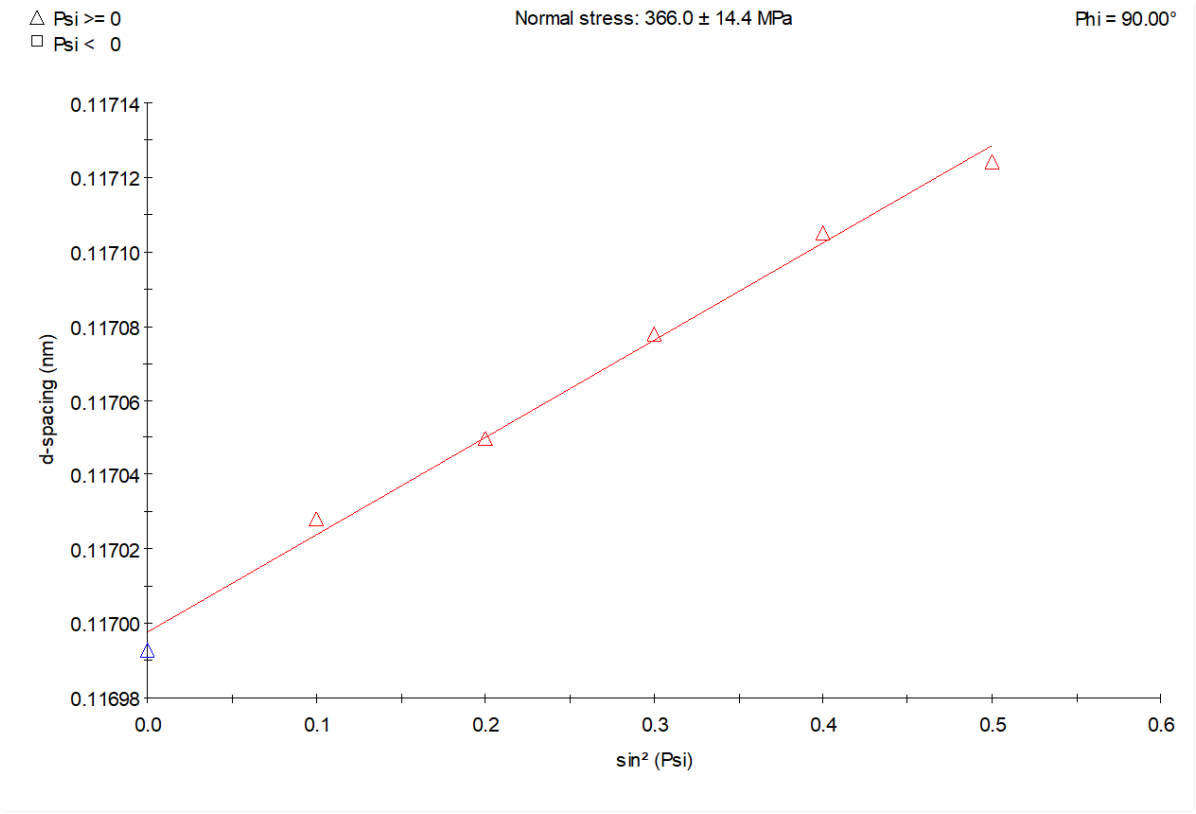

Figure B.19: Gasloos d vs $\sin^2\psi$ plot of the ferrite(211) reflection for $x \approx 0.30mm$

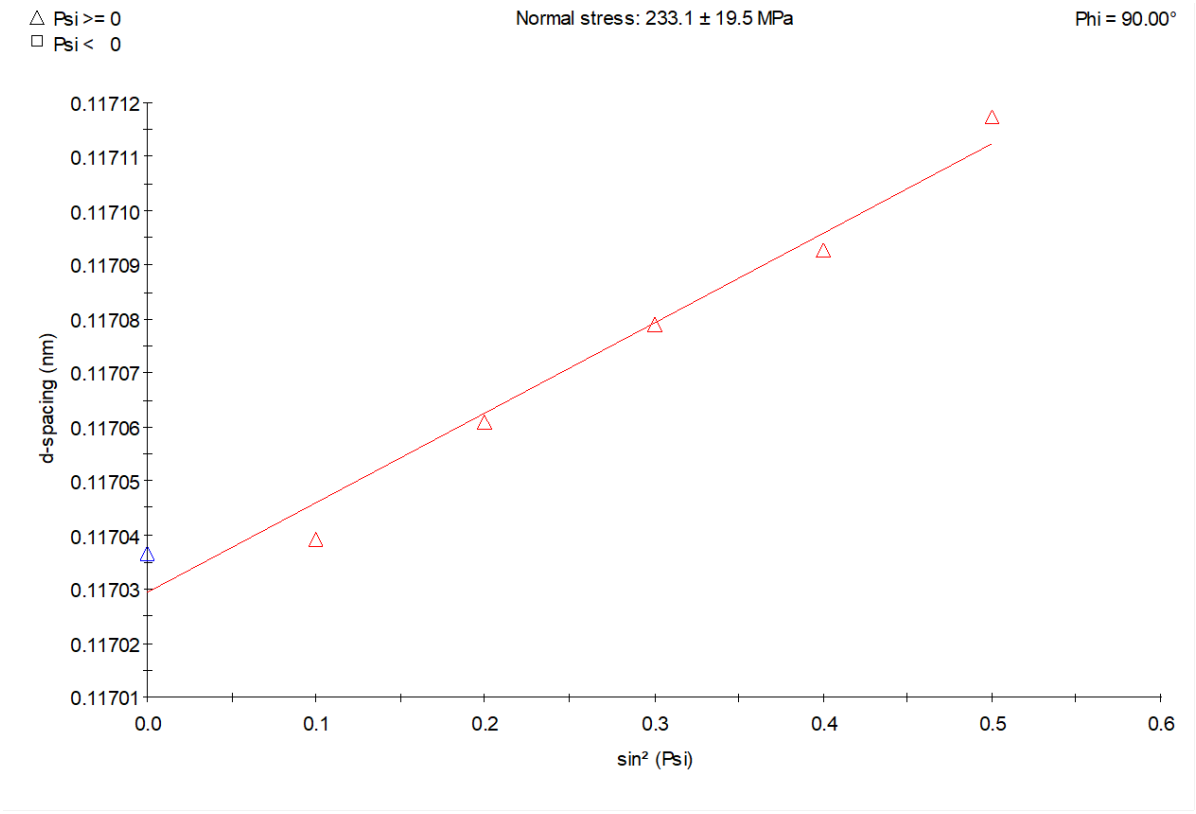

Figure B.20: Gasloos d vs $\sin^2\psi$ plot of the ferrite(211) reflection for $x \approx 0.35mm$

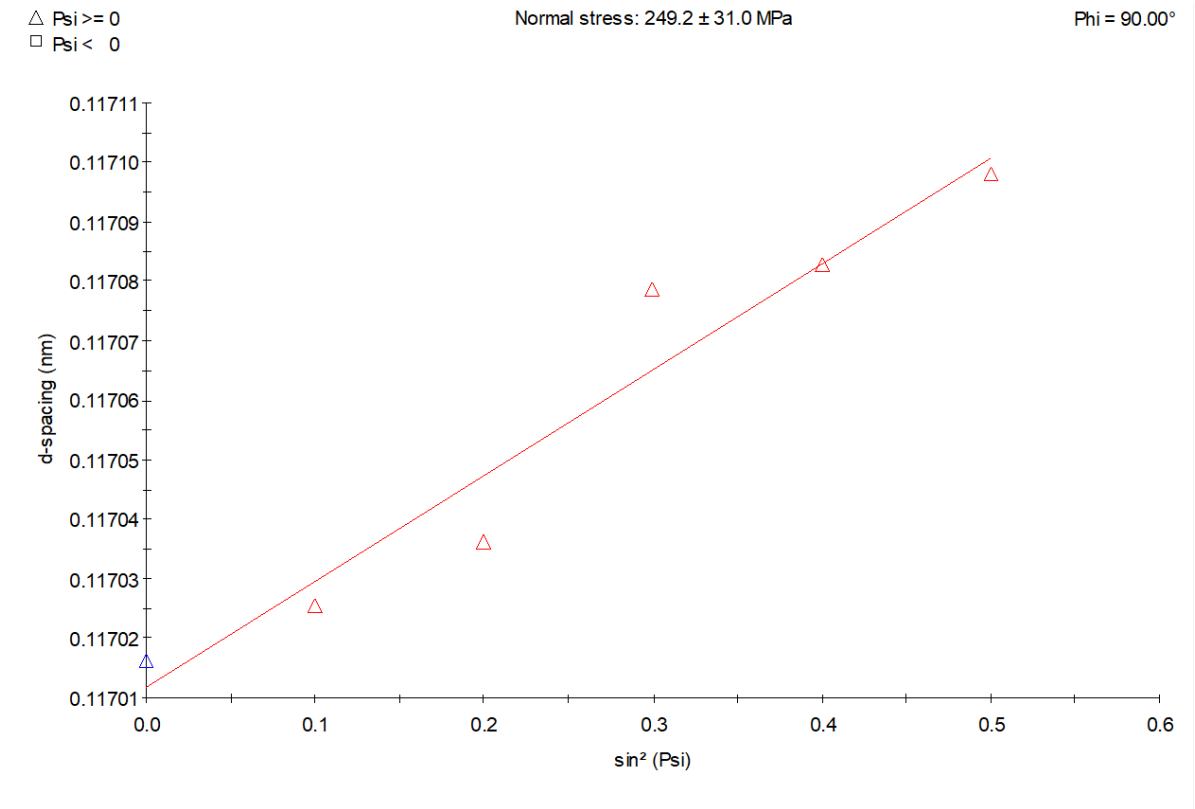

Figure B.21: Gasloos d vs $\sin^2\psi$ plot of the ferrite(211) reflection for $x \approx 0.40mm$

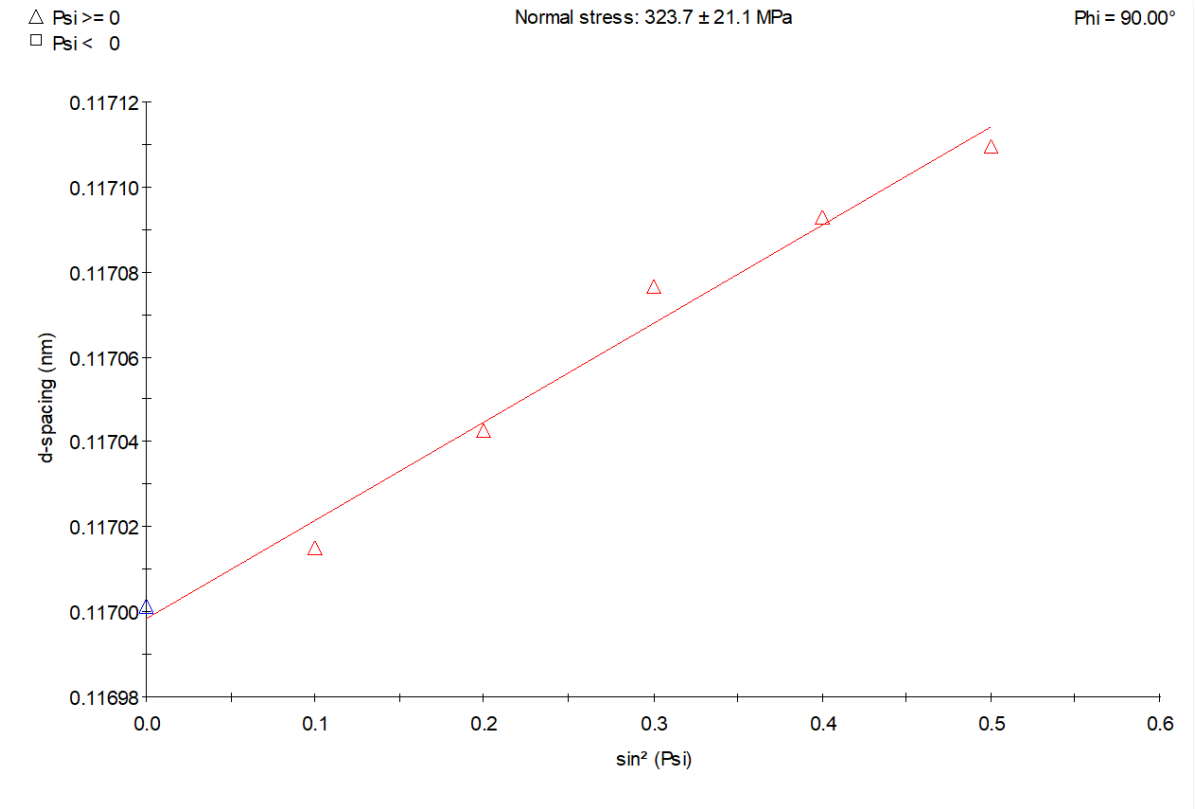

Figure B.22: Gasloos d vs $\sin^2\psi$ plot of the ferrite(211) reflection for $x \approx 0.45mm$

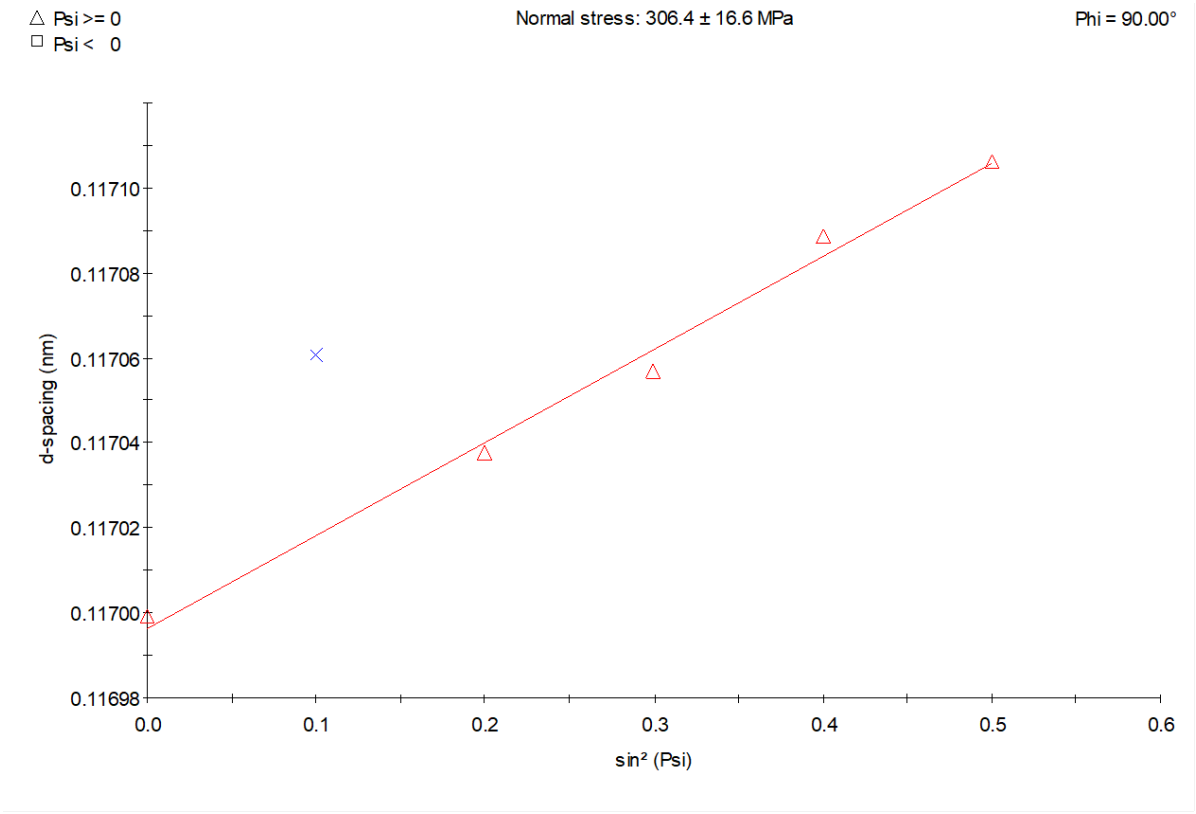

Figure B.23: Gasloos d vs $\sin^2\psi$ plot of the ferrite(211) reflection for $x \approx 0.50mm$

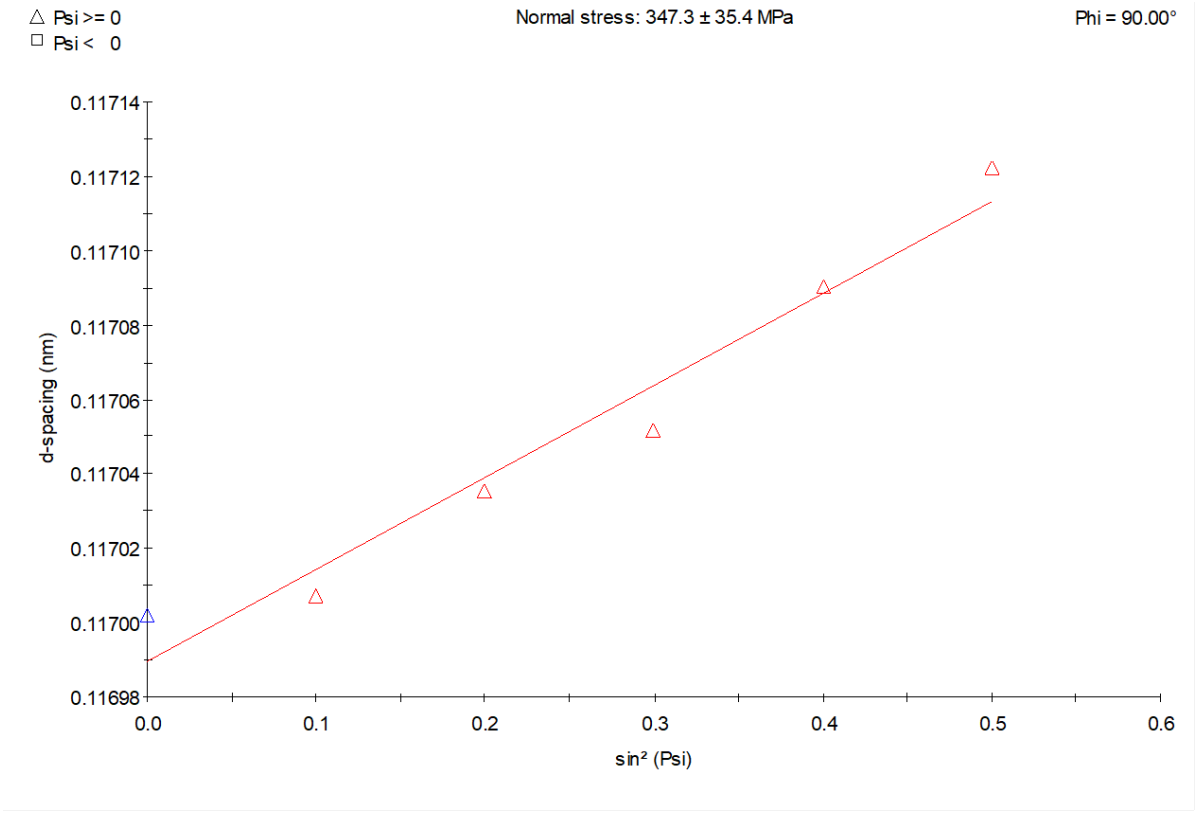

Figure B.24: Gasloos d vs $\sin^2\psi$ plot of the ferrite(211) reflection for $x \approx 0.55mm$